UC Davis
UC Davis Electronic Theses and Dissertations

Title

Atomistic Simulations of Hydrogen Embrittlement in Uranium

Permalink

https://escholarship.org/uc/item/3t16t1gd

Author

Soshnikov, Artem

Publication Date

2024

Peer reviewed|Thesis/dissertation

Atomistic Simulations of Hydrogen Embrittlement
in Uranium

By

ARTEM SOSHNIKOV
DISSERTATION

Submitted in partial satisfaction of the requirements for the degree of

DOCTOR OF PHILOSOPHY

in

Chemical Engineering

in the

OFFICE OF GRADUATE STUDIES

of the

UNIVERSITY OF CALIFORNIA

DAVIS

Approved:

_____
Nir Goldman, Chair

_____
Ambarish Kulkarni, Co-Chair

_____
Surl-Hee Ahn

Committee in Charge

2024

i

ABSTRACT

Uranium-based materials are an important research topic in material science due to numerous industrial and scientific applications. However, hydrogen embrittlement of uranium, which arises due to the formation of a structurally weak pyrophoric hydride, poses a major safety risk in material applications. Relatively little is known about the hydriding initiation mechanism in pure uranium, in part due to the material's highly reactive nature and toxicity. Future hydriding studies would thus greatly benefit from atomic-level simulations of the hydriding process, which can provide microscopic details about the hydrogen-uranium reaction and help guide future experimentation.

Kohn-Sham Density Functional Theory (DFT) is a well-established quantum mechanical technique that can be used to elucidate many aspects of the onset of hydride formation. DFT is used in chemistry, physics, and materials science for accurate prediction of physical and chemical properties, such as material equations of state, heats of formation, and the energetics of bond forming/breaking under reactive conditions. However, molecular dynamics (MD) simulations run with DFT are generally limited to time scales on the order of picoseconds and system sizes of a few hundred atoms. In contrast, many processes related to hydriding, such as initiation, nucleation, and growth, probe significantly longer time and length scales, and can require simulation cells of thousands of atoms run for nanosecond timescales or longer. In this regard, the Chebyshev Interaction Model for Efficient Simulation (ChIMES) approach is a method for rapid creation of reactive MD models. Briefly, ChIMES is optimized through determination of linear combinations many-body Chebyshev polynomials by fitting to DFT simulation data, such atomic forces, system energies, and stress tensor components. ChIMES has

been shown to yield similar accuracy to DFT while yielding linear scaling and orders of magnitude improvement in computational efficiency.

In this dissertation, we first present a systematic investigation of possible mechanisms for the formation of the metal hydride using DFT. Specifically, we address this problem by examining the individual steps of hydrogen embrittlement, including surface adsorption, subsurface absorption, and the interlayer diffusion of atomic hydrogen. Furthermore, by examining these processes across different facets, we highlight the importance of both (1) hydrogen monolayer coverage and (2) applied tensile strain on hydriding kinetics. Taken together, by studying these previously overlooked phenomena, our study provides foundational insights into the initial steps of this overall complex process.

Next, we use DFT generated data to develop a ChIMES U-H model that is fit to a training set containing energies and forces of U and UH_3 bulk structures with vacancies and hydrogen interstitials. We show that the bulk structural parameters, point-defect formation energies, and diffusion barriers predicted by the ChIMES potential are in strong agreement with the reference DFT data. We then use ChIMES to conduct MD simulations of the temperature-dependent diffusion of a hydrogen interstitial and determine the corresponding diffusion activation energy. Our work is likely to have impact in research areas where there traditionally is a strong need for computationally efficient methods to bridge length and time scales between experiments and quantum theories.

ACKNOWLEDGEMENTS

Table of Contents

LIST OF FIGURES

LIST OF TABLES

CHAPTER 1: INTRODUCTION

1.1 Hydrogen Embrittlement in Uranium

Uranium is a unique element that can be used in the energy industry as a nuclear fuel to generate electricity, and by the military to power submarines and for weaponry.[1] However, due to the high inherent reactivity of the metal, even trace amounts of hydrogen gas can readily induce corrosion. The pure metal occurs in three solid polymorphs: α (orthorhombic), β (tetragonal) and γ (body-centered cubic). The most prominent metal phase in nature is α-U, shown in Figure 1, which transforms to β-U at approximately 935 K and subsequently transforms to γ-U at approximately 1045 K.[2] However, uranium is also a highly reactive metal and under ambient conditions, it will react pyrophorically with hydrogen gas to form a brittle hydride (UH_3). This leads to operational hazards and makes surface hydrogenation experiments highly problematic.[3]

Uranium hydride can exist in two different phases: $α-UH_3$ and $β-UH_3$. Both phases possess a cubic lattice with each U atom is surrounded by 12 H atoms, as shown in Figure 1 (b and c). The $α-UH_3$ phase exhibits high symmetry and a face-centered cubic (fcc) structure, with four UH_3 formula units in the cubic unit cell. In contrast, the $β-UH_3$ phase exhibits lower symmetry with eight formula units per unit cell, though with cubic symmetry overall. The more compact α-phase completely converts to the β-phase at approximately 375 K,[4] generally below the operating conditions of many nuclear reactors.
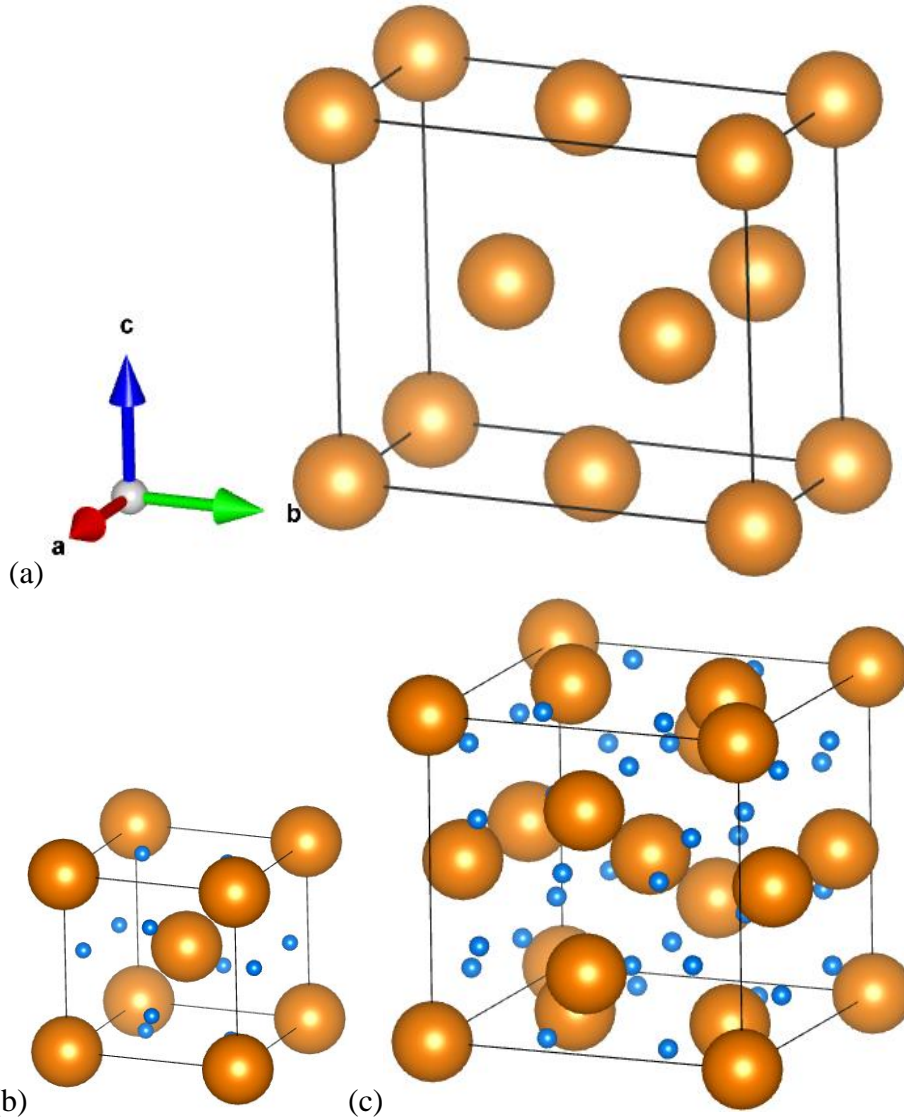
Figure 1. Crystal structure of (a) α-U (b) α-UH₃, and (c) β-UH₃ drown using Vesta (version 3.0) software.[5]

As uranium incorporates hydrogen, the uranium lattice expands by approximately 75% in volume, causing the formation of a black dispersive powder under ambient conditions with high surface area.[3] Uranium hydride is highly toxic and pyrophoric, releasing enormous amounts of heat upon exposure to air.[6] To date, there has been very limited understanding of how to control or mitigate the embrittlement process and relatively little is known about the hydriding initiation mechanism in pure uranium, in part due to the material's reactivity nature. Future hydriding

studies would thus greatly benefit from atomic-level simulations of the hydriding process, which can provide microscopic details about the hydrogen-uranium reaction and help guide future experimentation.

In the past few decades, many studies have investigated the thermochemistry, permeability, and diffusion of atmospheric gases within uranium. Experiments have shown that hydriding is characterized by the appearance of growing "spots," or surface monolayers.[7] These monolayer sites expand radially and eventually merge to form a continuous layer of hydride on the metal surface. Studies by Mallet and Trzeciak at 1 atm and 537 K showed the solubility of hydrogen in α-U to be 9.3×10^{-5} H atoms per unit cell U,[8] far below the U/H ratio of 1:3 in α/β-UH_3. In another study by Powell and Condon (reported by Condon and Larson), a diffusional barrier of 0.502 eV was estimated by tracking the preloaded hydrogen degassing rate from a uranium foils and determining an Arrhenius relationship for the diffusion constant.[9] These values would appear to indicate that hydriding initiation exhibits significant barriers under ambient conditions, in stark contrast to the observed formation process.

Previous experiments have largely investigated bulk properties[3] as well as hydrogen attacking regions beneath the hydride craters,[10] and did not directly probe surface effects. Such studies could overlook the potential importance of trap sites and the prevalence of hydriding at the surface and near the subsurface. In addition, hydriding experiments on pure uranium are difficult under ambient conditions. The uranium surface is typically covered with a protective oxide layer when exposed to air, which acts as a barrier to hydrogen reactivity, including diffusion and dissociation, and introduces a factor of unpredictability into the observed hydriding induction times. Future hydriding studies would thus greatly benefit from atomic-level

simulations of the hydriding process, which can provide microscopic details about the hydrogen-uranium reaction and help guide future experimentation.

1.2 Simulation approaches for hydriding.

In order to probe the formation of new material phases and the formation of covalent bonds, atomistic simulations frequently require use of Kohn-Sham Density Functional Theory (DFT), which has shown immense predictive capability for material phases over a wide range of thermodynamic conditions.[11–14] DFT is a well-established computational approach in material science, physics, and chemistry for the prediction of physical and chemical properties. A general overview of the method is described in the Appendix A section. DFT has been used to study numerous metal-hydrogen systems across the periodic table,[15–20] including palladium alloys,[21] titanium,[22] and many other systems. It has also been used to compute bulk absorption in plutonium[23] as well as hydrogen monolayer coverage on its low energy facets.[24] Several previous DFT studies have probed the initial interactions of α-U and hydrogen in the dilute limit (i.e., a single hydrogen atom per surface). For example, some results exist regarding surface energies, single atom/molecule geometries, point defect formation energies in the bulk, and adsorption energies on the (001) surface (generally considered to be the most stable).[14,25–29] While these studies provide useful information about the very first steps of the hydriding process (including H_2 dissociation), the effects of strain, concentration and partial pressure of hydrogen, and monolayer coverage remain entirely unknown.

DFT calculations, though, require immense computational resources per simulation step, and, therefore, are generally limited to time scales on the order of picoseconds and system sizes of few hundreds of atoms. Small-scale U+H calculations are consequently relatively tractable with DFT and can be used in dataset preparation and validation. However, DFT calculations are

4

generally too computationally intensive to model the polycrystalline regions, grain boundaries, and realistic defect concentrations that likely play a significant role in the hydriding process. In fact, for one of our studies, approximately 70,000 CPU hours was required to run a DFT-MD trajectory of a small α-UH_3 system (54U + 162H) for only 0.5 ps. In contrast, convergence of hydride initiation, nucleation, and growth studies could require simulation cells thousands of atoms run for nanosecond timescales or longer.[30] Therefore, uranium hydriding atomistic simulations require an alternative fast, accurate, and computationally-inexpensive approach that can calculate large-scale effects that are challenging to determine using DFT alone.

A practical solution to ameliorate these system size and time scale limitations is the development of computationally efficient MD force fields that can approximate the underlying potential energy surface with accuracy comparable to DFT. In this respect, classical force field approaches[31–33] have traditionally shown outstanding computational efficiency in modeling materials. These empirical approaches, though, generally do not allow for reactive conditions where bond breaking and forming occurs. Development of reactive force field methods, such as ReaxFF[34] and COMB,[35] incorporate both reactive and non-reactive terms with physically motivated bond-order forms, and allow for bond breaking and forming under realistic conditions. However, these methods frequently involve rigid functional forms that can require potentially challenging optimizations of non-linear parameters. More recently, machine learning (ML) approaches for MD simulations have been developed that utilize many-body kernels in more abstract, highly flexible functional forms. Examples include Gaussian Approximation Potential (GAP),[36] which leverages Gaussian Process Regression, and DeepMD,[37,38] which leverages deep neural networks. These ML approaches have shown high degree of accuracy and transferability for a number of systems.[39,40] ML approaches generally require large training and validation

datasets for training purposes as well significant training times due to their inherent non-linear optimization requirements. These issues can be of particular challenge for actinide containing systems, where existing DFT data can be limited, and training data can be challenging to generate due to the extreme computational effort associated with quantum calculations of high-Z materials.

Machine-learned methods that rely on linear parameterization, such as the Chebyshev Interaction Model for Efficient Simulation[41,42] (ChIMES), hold promise as an potentially easier to optimize model for accelerated MD simulations with a high degree of accuracy. ChIMES is a reactive force field for MD simulation based on linear combinations of many-body Chebyshev polynomials. The use of linear parameterization allows for optimal fitting coefficients to be solved for directly in most cases as well as powerful regularization approaches which are not necessarily available to non-linear optimization problems. ChIMES is based on an N-body expansion of DFT energies and forces and thus allows for a highly flexible functional form. In addition, use of Chebyshev polynomials imparts several advantages, including: (1) Chebyshev polynomials of the first kind are orthogonal and can be generated recursively, forming a complete basis set, (2) the derivatives of Chebyshev polynomials of the first kind are related to Chebyshev polynomials of the second kind, which are also orthogonal and generated recursively, (3) higher-order polynomials tend to have decreasing expansion coefficient values due to their monic form, and (4) Chebyshev polynomials of the first kind are nearly optimal, which means that the error due to interpolation closely resembles a minimax polynomial. ChIMES model optimization can be determined relatively quickly (e.g., within minutes for each optimization step of our study). In addition, ChIMES models have been shown in some cases to have significantly smaller data requirements and numbers of parameters than some neural network

approaches,[43] making them ideal for the application space to be studied here. Numerous ChIMES models have been designed for complex systems, such as molten liquid carbon,[41] water,[44,45] high-pressure C/O systems,[46,47] hydrazoic acid (NH3),[48] titanium hydride (TiH$_2$),[22] and silicon.[49]

1.3 Dissertation Scope and Structure

In this thesis, we greatly expand upon previously published results to further examine possible mechanisms for uranium hydriding, including bulk effects, the presence of multiple surfaces, and a wide range of hydrogen concentrations. In Chapter 2, we first perform a thorough analysis of DFT exchange-correlation functionals in order to determine an appropriate computational protocol that reproduces experimentally known bulk and surface properties. Hydrogen embrittlement and the phase transformation to α/β-UH$_3$ involve both changes in chemical composition and volumetric expansion of the lattice. Consequently, we investigate the process of uranium hydriding from two perspectives: (1) from formation of hydrogen monolayer coverage and (2) as a function of applied tensile load on the α-U lattice. We believe that both of these mechanisms could play significant roles in hydrogen embrittlement, and we quantify the relative importance of different surface adsorption sites and facets in the process.

In Chapter 3, we detail our efforts to create a ChIMES model for use in uranium hydriding studies. We start with a brief discussion of our DFT calculations as well as the ChIMES methodology. We then investigate different options for optimal values the ChIMES hyperparameters, including polynomials orders for different bodied interactions, the minimum and maximum interatomic distance cutoffs, and regularization parameters. We validate our model against previously determined computational and experimental results, including lattice constants and the bulk moduli of different U-H phases, as well as defect energies for single and multiple defects of uranium vacancies, hydrogen interstitials, and hydrogen vacancies in uranium

hydride. We then present results from simulations with our optimum model, including determination of kinetic properties for bulk hydrogen diffusion through bulk α-U, and molecular dynamics simulation of diffusion coefficients. In all cases, we find that our ChIMES model yields a high degree of accuracy relative to DFT calculations on smaller system sizes.

Finally, we complete this dissertation with some concluding thoughts (Chapter 4) and suggest some directions for further investigations (Chapter 5) in hydrogen-uranium chemistry that will allow us to make more direct contact with experiments. This includes discussions of opportunities for atomic-level simulations to make a more direct contact with experimental studies. Overall, this effort lays the groundwork for future atomistic modeling of actinide hydriding and provides a general model development framework for metal corrosion studies.

CHAPTER 2: QUATUM CALCULATIONS OF URANIUM-HYDROGEN INTERACTIONS

2.1 Introduction

Density Functional Theory (DFT) is a well-established computational approach that can provide valuable insights into physical and chemical properties of materials. In theory, DFT is exact for the ground-state energy and electron density; however, in reality the exchange-correlation energy has to be approximated using the appropriate exchange-correlation functional for a given system of study. In this chapter, we start with a detailed survey of DFT functionals related to our uranium-hydrogen study. We perform a down select of functional based on previously published experimentally known bulk and surface properties, such as lattice constants, surface energies, and atomic hydrogen adsorption energy. During hydrogen embrittlement, pure uranium undergoes a phase transformation that involves both changes in chemical composition and volumetric expansion of the lattice. Hence, we investigate the process of uranium hydriding from two perspectives: (1) from formation of hydrogen monolayer coverage and (2) as a function of applied tensile load on the α-U lattice.

2.2 Computational methodology

2.2.1 Calculation details

Density Functional Theory (DFT) calculations were performed using the Vienna ab initio simulation package code[50] (VASP). The projector augmented wave[51] (PAW) pseudopotentials for U provided in VASP include $6s^2 6p^6 5f^3 6d^1 7s^2$ as valence electrons. Fourth order Methfessel-Paxton smearing[52] was used with a value of 0.2 eV for all optimizations calculations in order to ensure energy convergence without dependence on the electronic smearing temperature. In our initial calculations, we examined the following exchange-correlation functionals: Perdew-Burke-

Ernzerhof (PBE), dispersion corrected PBE (PBE_D3BJ, RPBE_D3BJ), PBEsol, and SCAN, which were developed specifically for solids and solid surfaces. The energy cutoff for the planewave basis set for all our calculations was set to 500 eV based on convergence tests. Structural relaxations were performed until forces on each atom were less than 0.01 eV/Å. A k-point mesh of 14x7x8 generated by the MonkhorstPack[53] method for integration over the Brillouin zone was used for the primitive bulk unit cell optimization.

(a)   (b)   (c)
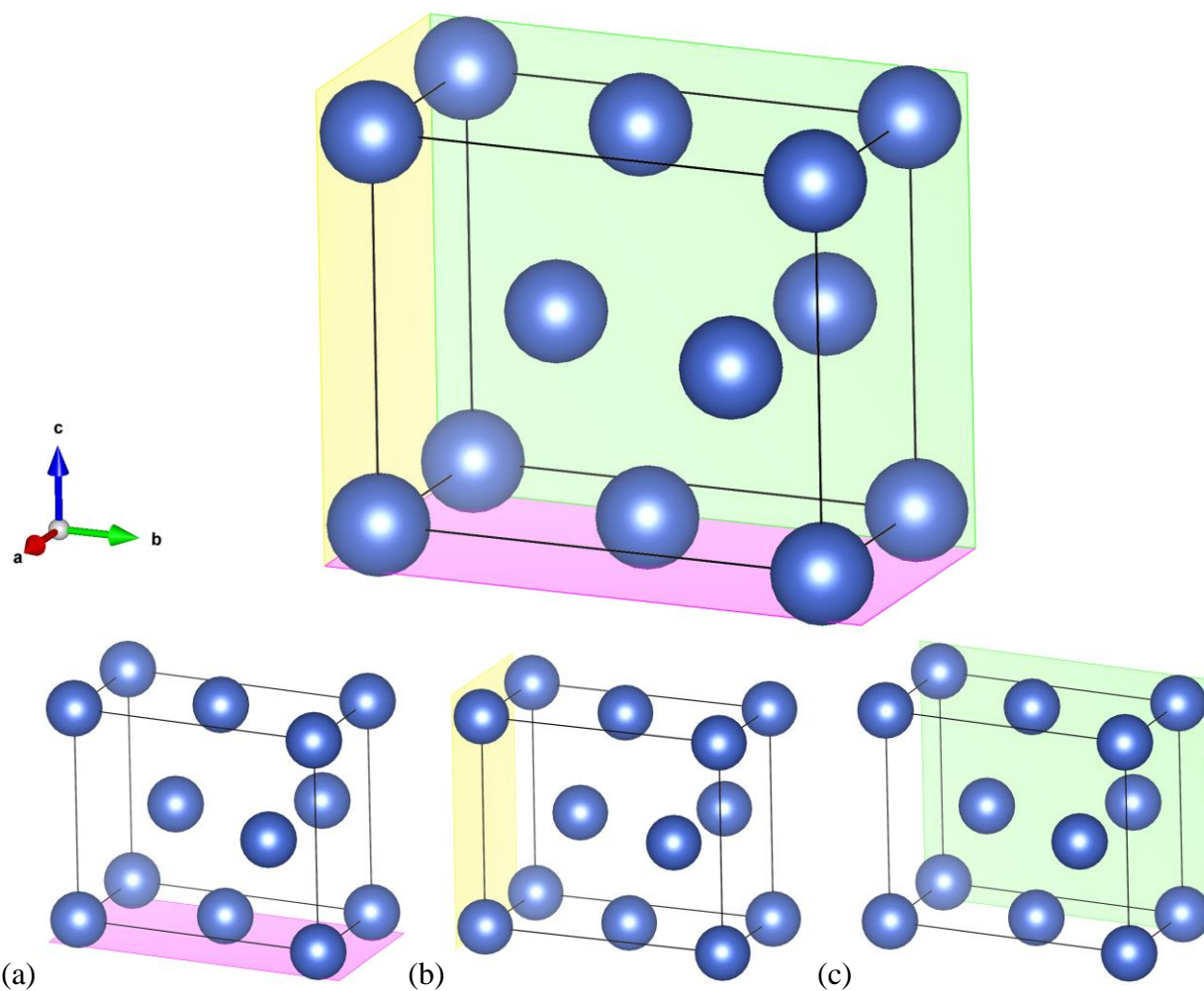
Figure 2: The α-U surface unit cell (a) (001) – magenta, (b) (010) – yellow, and (c) (100) – green.
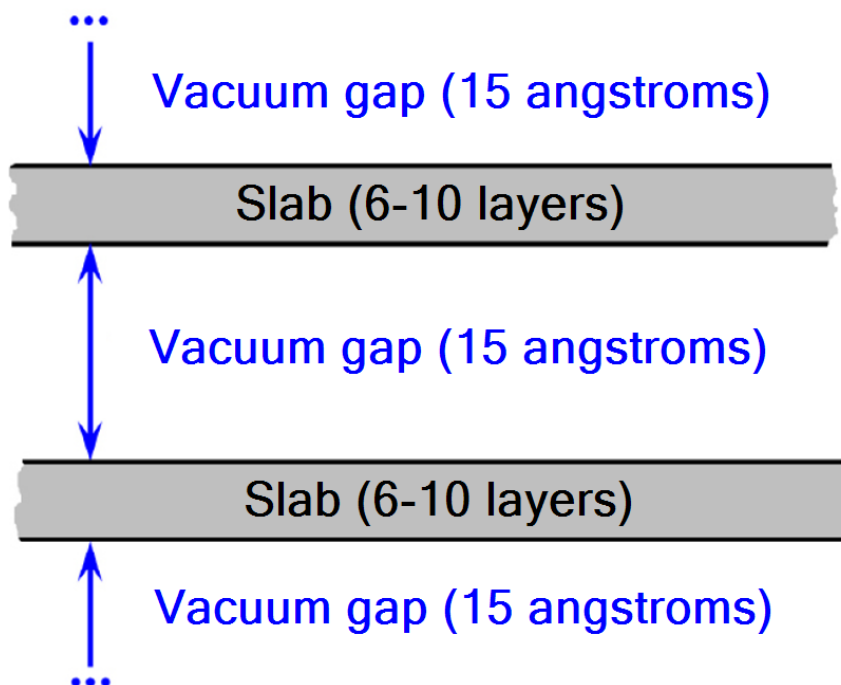
Figure 3: Cross-section of 3D model for α-U slab.

2.2.2   Surface and adsorption energies

Surfaces dominate features of the physical world, e.g., interfacial interactions govern fluid dynamics, heat and mass transfer, and chemical reactions. Therefore, understanding the chemistry at surfaces could potentially lead to understanding the hydrogen embrittlement process in uranium. The alpha phase of uranium has a face-centered orthorhombic structure with a CmCm space group[54] and the three stable low-index surfaces are well known (Figure 2).

In order to investigate how hydrogen reacts on α-U surface, surface properties of low index cleavage planes were examined using the surface slab model, which is a supercell representing an infinite two-dimensional thin film separated from periodic images by a large vacuum (Figure 3). In our study, slabs were generated from using Atomic Simulation Environment (ASE), as well as by hand for validation purposes. In order to make sure there are no interactions between adjacent slabs in the Z-orientation, a convergence study was performed

11

in a range from 2 to 20 angstroms of vacuum (Appendix B). We found that the vacuum thickness of 15 Å is adequate to meet the requirement. In addition, we concluded from multiple other convergence studies that at least a six-layer thickness is adequate for all relevant calculations.

Surface energy is defined as the required energy to cleave a surface of area A and is calculated using the following formula:

$$E_{surf} = \frac{E_{slab} - NE_{bulk}}{2A}, \qquad \text{Equation 1}$$

where E_{slab} is the total energy of the N-atom slab, E_{bulk} is the bulk energy per atom, A is the area of the surface. E_{bulk} is approximated using the Fiorentini and Methfessel[55] approach, from the slope of a linear fit of DFT energies from slabs of different thickness. This formulation assumes that both sides of the slab are identical, which is the case in this work.

The adsorption energy of one H atom on an α-U surface and the absorption energy into a subsurface site were determined using the following expression:

$$E_{ads/abs} = E_{(U/H)} - E_{(U)} - \frac{1}{2} E_{(H_2)}, \qquad \text{Equation 2}$$

where $E_{(U/H)}$ is the total energy of the optimized hydrogen+slab system, $E_{(U)}$ is the total energy of the clean slab, and $E_{(H_2)}$ is the total energy of the optimized isolated H_2 molecule. A negative adsorption energy corresponds to a stable adsorbate/surface system. The surface adsorption and subsurface absorption behavior of hydrogen was modeled using a (2x1) surface unit cell with 6-10 layers depending on the facet (between 24-40 U atoms), while the bulk absorption was modeled using a 4x2x2 supercell (64 U atoms). In contrast to the surface energy calculations, the bottom two layers were constrained to simulate the bulk environment while the rest were allowed to relax their equilibrium positions.

2.3 DFT functional comparison

2.3.1 Lattice parameters

Before we investigate uranium surface chemistry, we first perform a benchmark comparison study of the equilibrium lattice parameters with various exchange-correlation functionals with experimental values. As shown in

Table **1**, all exchange-correlation functionals used here underestimate the experimentally reported lattice constants. However, these deviations are relatively small (less than 3.97%). Even though PBEsol is designed to improve upon PBE for equilibrium properties of closely packed solids, it slightly underperforms its predecessor in terms of estimating lattice parameters. In addition, the long-range dispersion effects in PBE_D3BJ and RPBE_D3BJ also do not yield improved results, as these functionals display the worst calculated lattice constants. SCAN, which is a meta-GGA functional and thus includes the second derivative of the electron density, shows better results than all D3 functionals and PBEsol, but slightly worse than PBE. Overall, we observe that PBE and SCAN showed the lattice constants slightly closer to the experimental values, followed by PBEsol, PBE-D3BJ, and RPBE-D3BJ.

Table 1: Estimated equilibrium lattice parameters for α-U unit cell using PBE, PBEsol, PBE_D3BJ, RPBE_D3BJ, and SCAN functionals. Percent deviation from the published experimental result are indicated in parenthesis. GGA+U calculations used a value of $U_{eff} = U - J = 1.24$ eV.

method	a (Å)	b (Å)	c (Å)	volume (Å³)
PBE	2.811 (-1.16%)	5.857 (-0.20%)	4.901 (-0.63%)	80.690 (-1.98%)
PBEsol	2.745 (-3.48%)	5.753 (-1.98%)	4.839 (-1.89%)	76.417 (-7.17%)
PBE_D3BJ	2.752 (-3.23%)	5.729 (-2.39%)	4.853 (-1.60%)	76.513 (-7.06%)
RPBE-D3BJ	2.731 (-3.97%)	5.681 (-3.20%)	4.830 (-2.07%)	74.937 (-8.97%)
SCAN	2.803 (-1.44%)	5.854 (-0.26%)	4.898 (-0.69%)	80.370 (-2.37%)
PBE+U[56]	2.849 (+0.18%)	5.869 (+0.00%)	4.977 (+0.92%)	83.222 (+1.09%)
EXP[57]	2.844	5.869	4.932	82.322

We note that standard DFT functionals tend to underestimate electron correlations for 5f materials (e.g., U, Pu), which in turn can result in an underestimation of the atomic volume.[58] In general, this effect can be corrected through the inclusion of semi-empirical on-site Coulombic repulsions.[59] As shown in

Table **1**, the GGA+U approach somewhat improves α-U lattice parameter prediction, though its effects are relatively small.[60] Inclusion of the Hubbard U correction can drastically slow down surface convergence in actinides and have a minimal effect on surface adsorption energies.[61] In addition, PBE and PBE+U calculations have been shown to yield the same energetic ordering of surfaces for metallic solids.[62] Consequently, the accuracy of a subset of the functionals studied here are within reasonable accuracy without that correction.

2.3.2 Surface energies and atomic hydrogen adsorption on α-U (001) surface

After optimizing and comparing the lattice constants, we also performed an exchange-correlation functional comparison study by computing surface energies (

Table **2**). Here, we chose the (001) surface as this is the most stable α-U facet. The experimental surface energy of α-U is 1.828 J/m^2, however, this value corresponds to an isotropic crystalline structure of the metal or an average value of different surfaces.[26] Since the (001) facet has the lowest energy, it would be the most abundant surface in uranium crystalline material. As presented in

Table **2**, the descending order of the surface energy for various functionals is

RPBE_D3BJ > PBE_D3BJ > PBEsol > PBE > SCAN. The experimental surface energy is in

close proximity to the results determined from PBE and SCAN, while estimates by other

functionals are much higher.

Table 2: Energetic parameters and geometric features of H atoms on α-U (001) surface estimated using PBE, PBEsol, PBE_D3BJ, RPBE_D3BJ, and SCAN functionals. E_{ads} denotes the adsorption energy, d_{H-surf} represents the average binding height from H atom to the top layer of the slab, and SE denotes the surface energy for the pristine surface.

Approach	Ads Site	E_{ads} (eV)	E_{ads} (eV) w/zpe	d_{H-surf} (Å)	SE (J/m²)
PBE	hollow1	-0.51	-0.35	2.229	1.839
	hollow2	-0.57	-0.41	2.221	
PBEsol	hollow1	-0.59	-0.43	2.226	2.191
	hollow2	-0.65	-0.49	2.219	
PBE_D3BJ	hollow1	-0.58	-0.42	2.231	2.834
	hollow2	-0.64	-0.48	2.225	
RPBE_D3BJ	hollow1	-0.58	-0.42	2.223	3.482
	hollow2	-0.62	-0.46	2.215	
SCAN	hollow1	-0.51	-0.35	2.274	1.832
	hollow2	-0.57	-0.41	2.264	

Van der Waals (vdW) interactions are generally significant for surface properties and their inclusion in DFT models remains an area of active research.[63] PBE generally neglects most of the vdW interactions, while SCAN incorporates intermediate-range vdW, and D3 functionals include even long-range dispersion effects. Remarkably, these dispersion effects are of less importance in estimating bulk and surface properties in α-U. As mentioned, the closest agreement in estimating the surface energies was achieved by PBE and SCAN. SCAN is considered a more advanced functional due to inclusion of all 17 known exact constraints that a meta-GGA can satisfy. However, we only notice slight improvements in results calculated by SCAN over PBE.
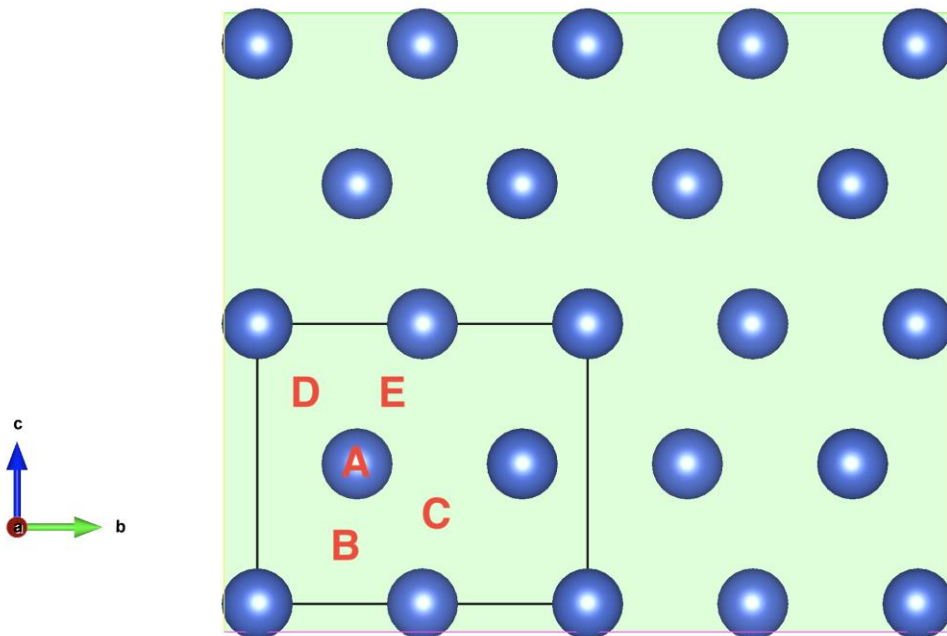
Figure 4: Schematic illustration of initial adsorption sites on (001) surface. A, B, C, D and E represent the initial sites of top, hollow1, hollow2, longbridge, and shortbridge, respectively.

In addition to surface energies, we performed a similar comparison study in estimating atomic hydrogen adsorption energies on the most stable (001) α-U surface (Figure 4). As shown, five possible unique adsorption sites (denoted as top, hollow1, hollow2, longbridge, or shortbridge) were considered. For all cases, the H atom is unable to remain stable at the top, long-bridge, or shortbridge sites, relocating to a more stable hollow site nearby. This indicates that there are only two preferred adsorption sites on the (001) surface for a single hydrogen adsorption: hollow1 and hollow2. Similar results are observed in nitrogen/uranium[56] and oxygen/uranium[64] systems. In addition, all functionals used here indicate that the hollow2 site is slightly more energetically favorable (~0.06 eV) compared to hollow1.

Table **2** also shows minimal differences between functionals, with a relatively small energetic spread of ~0.08 eV for all approaches, due in part to the various representations of vdW interactions. We note that quantum nuclear vibrational zero-point energies (ZPE) can be significant for low-Z elements such as hydrogen. As a result, we have computed the ZPE for hydrogen surface adsorption energies. We observe that the ZPE tends to occur as a systematic correction, depending on the type of functional, but the overall order of energetics of sites is preserved. Uranium phases are known to exhibit magnetic moments at their surface,[65,66] which can affect surface adsorption energies[67] and will be considered in future efforts.

Overall, we have computed the lattice constants, surface energies, and atomic hydrogen adsorption energies on the (001) facet. We have compared experimental determined results to those calculated by various exchange-correlation functional approaches. Given the correct ordering and reasonably small differences in adsorption energies, surface energies, and lattice constants results, PBE was our functional of choice for the rest of our studies.

2.4 Absorption into α-U (001) first subsurface layer

Upon molecular dissociation, atomic hydrogen will tend to bind in thermodynamically favored surface adsorption sites. This can be followed by diffusion of hydrogen from the surface to the subsurface, which could also play a substantial part in hydrogen embrittlement process. We now calculate the energetic parameters of hydrogen absorption into the first subsurface layer. In this section, we present results for the (001) facet, while results (for the most stable site) for all other surfaces of interest are presented in Table S2 (Supplementary Information).

Figure 5 shows the typical interstitial sites for the (001) surface: tetrahedral (Tet), square-pyramidal (Sqpy) and octahedral (Oct). Due to the low symmetry of the α-U surface, there are one Oct and two types of Tet and Sqpy sites between the top and the first subsurface layers. Tet1

19

has three surface and one subsurface uranium nearest neighbors, while Tet2 is surrounded by one

surface and three subsurface U atoms (Figure 5 a, b). Sqpy1 has three surface and two subsurface

U nearest neighbors, while Sqpy2 has two surface and three subsurface U atoms (Figure 5 c, d).

Oct has three surface and three subsurface U atom nearest neighbors (Figure 5 e).
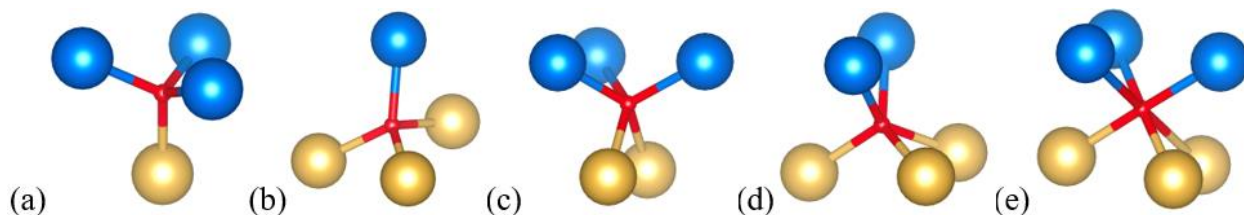
Figure 5: High symmetry interstitial sites of hydrogen atoms in the first subsurface layer of α-U (001) surface: (a) Tet1 (b) Tet2 (c) Sqpy1 (d) Sqpy2 (e) Oct. The top layer U atoms are labeled in blue, the second layer U atoms in yellow, and the hydrogen interstitial in red.

The subsurface interstitial/absorption energies for each unique site were calculated using

Eq. 2. The absorption energies, site type, the distances between absorbed hydrogen and top

surface layer are listed in

Table **3**. All of the subsurface absorptions in the first sublayer were found to be endothermic. The subsurface absorption at Tet1 site was found to be the most favorable (0.16 eV), followed by Sqpy1 (0.25 eV), Sqpy2 (0.32 eV), and Tet2 (0.49 eV). In fact, the Tet1 value is almost half of the absorption energy of 0.32 eV at tetrahedral interstitial site in bulk (as per our own calculations). First layer subsurface absorption at the Oct site was found to be unstable as hydrogen atom prefers to migrate to the more stable Sqpy1 site during geometry optimization. We notice a trend of sites closer to the surface having lower energetics, in correlation with lower d_{H-surf} values, shown in

Table **3**.

Table 3: The subsurface absorption energies and geometric parameters of hydrogen atoms under (2x1) α-U (001) surface. E_{abs} denotes the average absorption energy to insert H atom inside the first subsurface layer; d_{H-surf} represents the distance between H atom to the top surface layer.

Interstitial Type	E_{abs} (eV)	d_{H-surf} (Å)
Tet1	0.16	0.463
Tet2	0.49	1.884
Sqpy1	0.25	0.818
Sqpy2	0.32	1.379
Oct	----	----

We performed similar analysis of subsurface absorption on other low-index facets and the most favorable energetic sites are shown in Table S2 (Supplementary Information). In general, we found that these are either of Tet or Sqpy geometry and absorption energy increases as hydrogen penetrates deeper within the lattice. Regardless of the surface, single hydrogen absorption into a defect-free α-U surface is an endothermic process for all facets studied here.

2.5 Effect of tensile load on surface adsorption, subsurface absorption, and diffusion

Due to the substantial lattice expansion of α/β-UH₃ compared to α-U, there is likely a significant tensile strain of the α-U lattice as more hydrogen diffuses into bulk. In this section, we investigate the surface adsorption and subsurface absorption properties as a function of applied tensile load on an α-U surface supercell of 6-10 layer thickness (with the bottom 2 layers fixed). Convergence studies indicated that a six-layer slab with a vacuum layer of 15 Å between the two adjacent slab surfaces were found to be adequate for all relevant calculations. Tensile strain was applied to each facet by first applying an isotropic strain to the bulk followed by optimization of the ion positions. We then created a surface slab for each facet and optimized its geometry while constraining the bottom two atomic layers. Interplanar distances were then

computed by selecting a given surface atom and calculating the distance of the atom directly underneath.

In order to investigate thermal activation of these dilated geometries, we have computed the pressure-volume work required to create tensile loads in the bulk by fitting volumetric strain data to the Birch-Murnaghan isothermal equation of state and computing the pressure-volume work. Our results indicate that ~0.04 eV is required for the lattice to expand up to 4%, which is likely thermally accessible under ambient conditions, and we use this value as an upper bound for our study here.

Figure 6a shows the surface energies for three standard terrace surface, (001), (010), and (100), as well as those for two kinked facets, (012), and (102), all as a function of applied tensile strain. In addition to common low-index terrace surfaces, we have analyzed a few stepped facets (Figure 7). In realistic systems, surfaces are non-ideal, defect-rich, and contain imperfections, such as kinks, steps, or defect sites. In fact, stepped facets play a significant role in the palladium hydriding process[68], implying their potential significance in this work as well. When no strain is applied, (001) is the most stable facet relative to other surfaces. In contrast, the α-U (012) kinked facet has the highest energy and, thus, the most unstable. When symmetric tensile strain is applied, the surface energy decreases for all facets. In fact, the volumetric expansion of the lattice causes densification along the surface normal as the interlayer distance decreases with applied load, which is compensated for with increased U-U bond distances within the same layer (Table S1 in SI). The effective coordination number can serve as an additional descriptor for predicting surface chemistry and activation energies[69,70] and could be included in subsequent work.
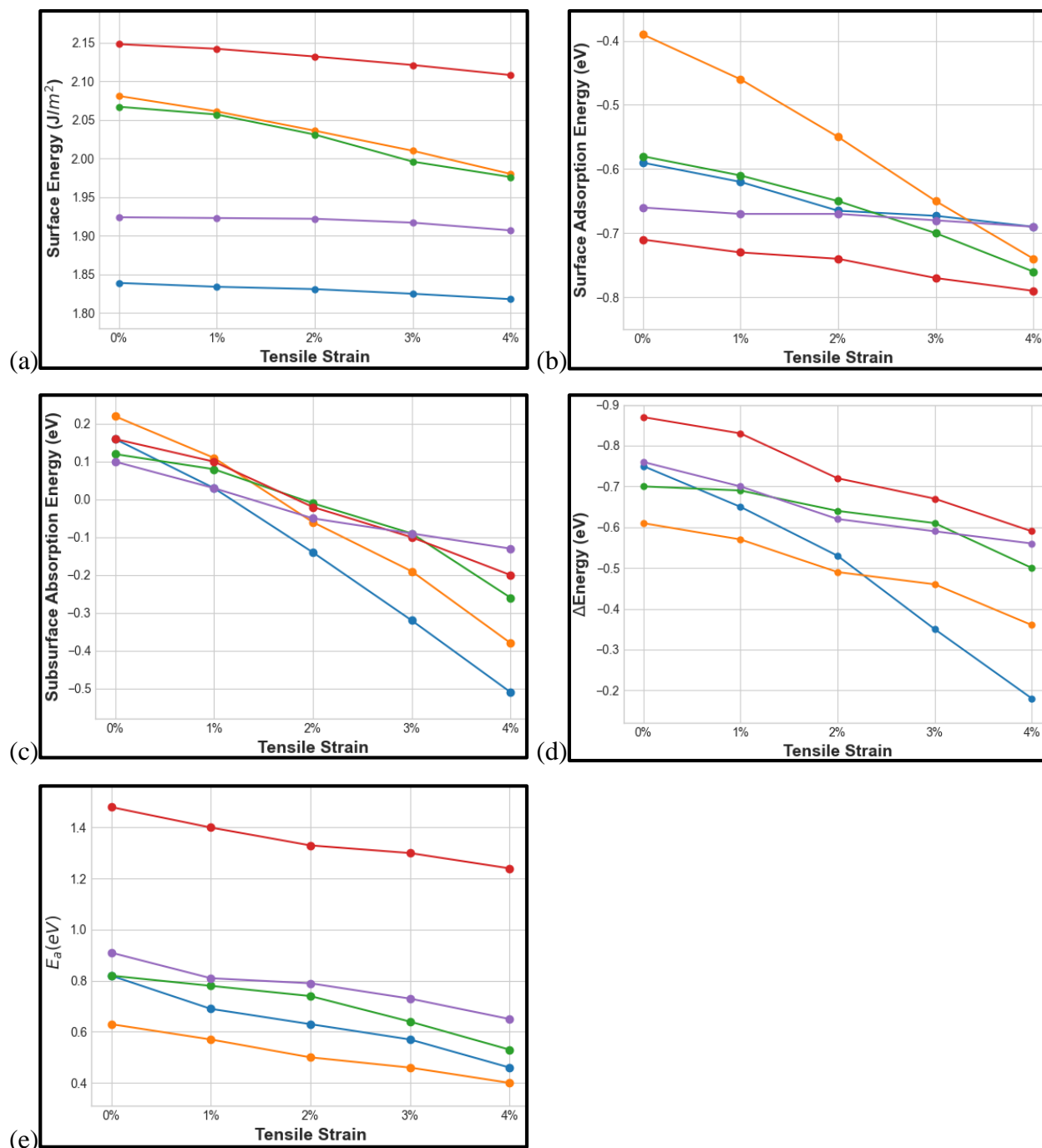
Figure 6: Applied tensile strain study for (001)-blue, (010)-orange, (100)-green, (012)-red, and (102)-purple α-U facets. For a given surface and applied load: (a) the surface energy (b) the lowest adsorption energy, (c) the lowest subsurface absorption energy, (d) the energy difference (ΔE) between the surface adsorption and the subsurface absorption, and (e) the activation energy (E$_a$) for atomic hydrogen diffusion between the lowest adsorption and subsurface absorption sites for a given surface. Note: refer to Supplementary Info for a more detailed information.
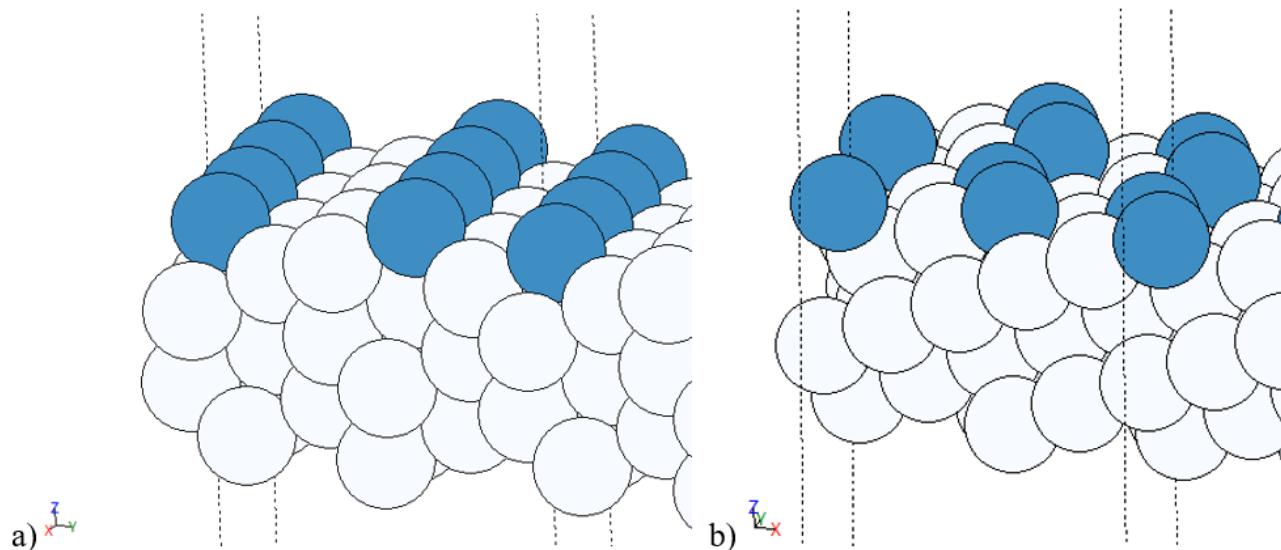
Figure 7: α-U kinked surfaces. Kinked U atoms are highlighted in blue. a) (012), b) (102).

The effect of tensile strain on H atom surface adsorption and subsurface absorption are illustrated in Figure 6 (b-d) (also Table S2 in Supplemental Information). Here, we compare the lowest surface adsorption to the lowest subsurface absorption site, as well as assess the trends for hydrogen diffusion from the most stable surface site to nearby subsurface site. For all facets and tensile loads, hydrogen surface adsorption prefers to bind at the hollow 3-fold sites, excluding the (010) surface where the 4-fold adsorption sites are uniformly favored. On the other hand, the tetrahedral subsurface site is preferred for the (001), (012), and (102) surfaces, while the square-pyramidal is favored in (010) and (100) slabs. Adsorption on the stepped facets is more energetically favorable than on terrace surfaces (Figure 6a). For example, under 0% strain, the adsorption energies for (012) and (102) are -0.71 and -0.66 eV, while the energies for (001), (010), and (100) facets are -0.57, -0.39, and -0.58 eV, respectively. Compared to the terrace surfaces studied here, the stepped regions yield some distortion of distances and angles between surface atoms (see Figure S2 for details) that may result in higher reactivity towards hydrogen.

In addition, we observe that tensile strain uniformly results in lower hydrogen surface adsorption energy (Figure 6a). Similar trends are observed in H/Pt(111) and H/Rh(111) systems, and have been confirmed in phenomenological thermodynamic studies,[71] where a tensile load leads to stronger hydrogen bonding to the surface of interest.[72] When elastic strain is applied, two effects promote bonding between hydrogen and nearby uranium atoms. With increased tensile strain, the distances between all atoms within a surface layer also increase, which leads to a decreased bond strength. However, counteracting this effect is the simultaneous reduction of the distance between the hydrogen adsorbate and the subsurface U atoms, which then stabilizes adsorbate/surface interactions. In addition to the adsorption energy, we also notice tensile strain has a significant effect on the subsurface absorption energy (Figure 6b). In fact, only 2% tensile strain is required for subsurface absorption to become an exothermic process.

As shown in Figure 6c, the energy difference (ΔE) between surface adsorption and subsurface absorption energy decreases as tensile strain increases, which means that lattice expansion can facilitate the formation of the hydride. This effect is enhanced in terrace surfaces, e.g., (001), (010), (100), compared to the stepped surfaces, (012) and (102). Since this surface penetration reaction energy decreases the most for most stable (001) facet, this surface/subsurface transition could be more sensitive to tensile load of those studied here. Overall, we observe that atomic hydrogen prefers to bind at the stepped sites, but surface to subsurface diffusion could be more likely to occur from the (001) facet.

In addition to the thermodynamic properties, we have also computed activation barriers of hydrogen diffusion from the surface to first subsurface via NEB (Figure 6e). Here, the Climbing Image Nudged Elastic Band (CI-NEB) method was employed to find the transition state and the minimum energy path (MEP) for each surface of interest. In this approach, a chain

27

of 6-8 linear interpolation images along an initial pathway between a given initial and final states

of a reaction is relaxed to determine the MEP and its corresponding saddle point. The images are

relaxed along the energy pathway until the maximum residual forces on each atom are less than

0.01 eV/Å. The transition state was confirmed by presence of one imaginary vibrational

frequency.
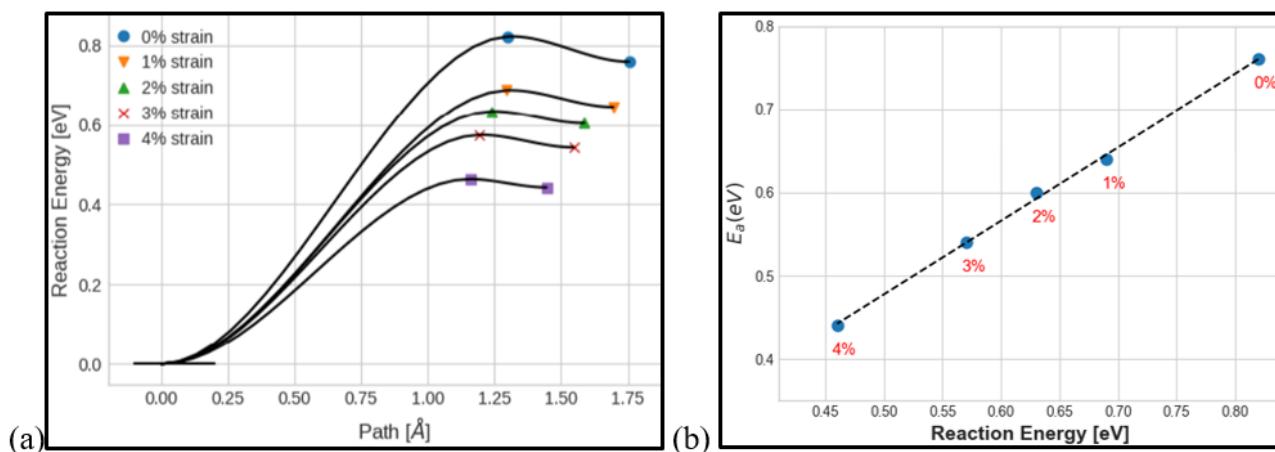
Figure 8: (a) Schematic illustration of the reaction barrier for H penetration on a α U (001) surface under tensile strain and (b) the activation energy vs reaction energy plot as a function of tensile strain.

The surface to subsurface MEPs and activation energies were calculated with hydrostatic

elastic tensile strain of up to 4%. Results are shown in Figure 8a for the α-U (001) surface (see

Table S2 in the SI for results for other facets). As hydrogen penetrates the (001) surface cell, it

has to overcome an activation energy barrier of 0.82 eV on the surface with no strain, 0.69 eV

with 1%, 0.63 eV with 2%, 0.57 eV with 3%, and 0.46 eV with 4% tensile load. These values are

in close proximity with the experimental result of 0.502 eV for activation barrier.[9] This trend is

similar to our results for the adsorption and absorption energies, as well as previous calculations

of hydrogen diffusion in expanded bulk palladium supercells[73]. In this case, stronger hydrogen

bonding in the strained system likely also stabilizes the transition state, leading to lower

activation energies overall. We also notice that the relative path from the adsorption site to the final subsurface absorption site gets shorter with tensile strain. This could be attributed to the reduction of the distance between the hydrogen adsorbate and the subsurface U atoms due to the decrease of interlayer spacing described in the above section. In addition, the plot of the activation barrier as a function of reaction energy (Figure 8b) shows a linear dependence, while simultaneously showing an inverse relationship to the applied tensile load. Thus, this relationship can potentially be exploited as a predictive tool to estimate diffusional barriers for similar loads. As shown in Table S2, results for other surfaces follow a similar trend, with facets exhibiting lower adsorption energies (e.g., kinked vs. terrace surfaces) showing higher activation diffusion barriers overall.

We note that quantum nuclear vibrational zero-point energies (ZPE) can be significant for low-Z elements such as hydrogen. As a result, we have computed the ZPE for hydrogen surface adsorption and subsurface absorption, as well as those effects on reaction energies and transition states (see Table S1 in the SI for detailed results). We observe that the ZPE tends to occur as a systematic correction, depending on the atomic environment of the hydrogen atom. For example, surface adsorption results in a ZPE correction of 0.15 ± 0.02 eV whereas as subsurface absorption results in a correction of 0.22 ± 0.02 eV. However, in general the ZPE effect is canceled for the reaction and transition state energies, which are very similar to their non-corrected counterparts. We also observe that for some facets, the ZPE correction results in a slight increase of the tensile load requirement for exothermic surface diffusion. However, vibrational frequencies from DFT are known to exhibit functional dependence, and choice of a different functional could affect these results[74]. A systematic study of ZPE effects in uranium containing systems can be explored in future work.

2.6 Coverage dependence on atomic hydrogen surface adsorption and subsurface absorption

2.6.1 Monolayer coverage dependence

Adsorption on metal surfaces is governed by both the adsorbate/surface interactions and the adsorbate/adsorbate interactions that could be attractive or repulsive. Such interactions can significantly impact the kinetics and thermodynamics of processes on surfaces, such as monolayer formation, desorption, diffusion, phase transitions, and chemical reactions.[75,76] In the previous section, all of the adsorption calculations were performed on lower surface coverage, isolated systems (e.g., in the dilute limit). However, this dilute limit does not always correspond to experimental conditions, where a range of monolayer coverages can be explored. Here, we compute properties over a range of monolayer coverages, helping to bridge the gap between DFT and experiments.

In order to understand the effects of multiple hydrogen atoms, we assess the effect of increasing hydrogen coverage on adsorption unstrained surfaces. In this case, we calculate the energetic trend for an increasing monolayer coverage by computing the adsorption energy per H atom using the following formula:

$$E_{ads} = \frac{E_{(U/H)} - E_{(U)} - 1/2 N_H * E_{H_2}}{N_H} \qquad \text{Equation 3}$$

where $E_{(U/H)}$ is the total energy of the system with adsorbates present, $E_{(U)}$ is the total energy of the clean surface, E_{H_2} is the energy of gas phase hydrogen molecule, and N_H is the number of adsorbed hydrogen atoms. In our study, the full monolayer (ML) coverage corresponds only to exothermic adsorption of hydrogen. For example, the (001) facet contains 20 possible adsorption sites (top, hollow, and bridge). However, only the first 8 adsorbed hydrogens in hollow sites

yielded exothermic adsorption. Therefore, for (001) surface we elaborated the adsorption

behavior at coverages ranging from 1/8 ML to 1 ML.

In order to overcome the combinatorial issue associated with an exhaustive search for

adsorbate-surface structures, we employed a greedy forward-stepwise sampling method.[77] This

approach allows for finding an adsorbate/surface configuration with a reasonably low energy

using a minimal amount of computational resources. First, we determine the most favorable

configuration for a single hydrogen atom on a given facet. Then, we take that configuration and

add another hydrogen atom to different sites until we determine the lowest energy configuration

for that particular coverage. The process is repeated step-wise until the full monolayer coverage

is achieved.
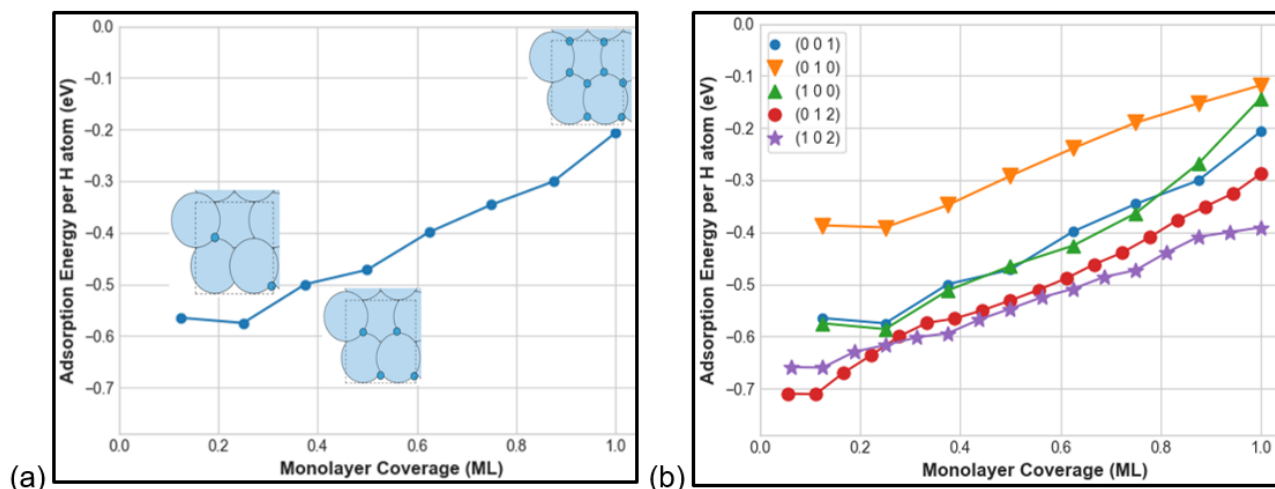
Figure 9: Adsorption energy per H atom on α-U surface at different coverage: (a) (001) facet,
(b) a cross-facet comparison including the (001)-blue, (010)-orange, (100)-green, (012)-red, and
(102)-purple α-U surfaces.

As shown in Figure 9, different structural combinations at each specific monolayer

coverage produce a dissimilar average adsorption energy. In addition, the average adsorption

energy becomes more positive as more hydrogen adsorbs on any given surface. For the (001)

surface (Figure 9a), the first H adatom prefers to bind to the hollow2 site, as previously

described. At 0.25 ML coverage, the second hydrogen atom prefers to bind nearest hollow2 site. At this point, we observe some electrostatic screening from uranium atoms (flat line) as there are little to no interactions between two adsorbed hydrogen atoms that are spatially close to each other. In fact, the same preference occurs up until all hollow2 sites are occupied. At 0.5 ML coverage, the four hydrogen adatoms form a period zigzag structure on the α-U (001) surface. Newly added H atoms adsorb to nearby available hollow1 sites until all hollow sites are occupied at 1 ML coverage.

We observe similar trends on other terrace and stepped facets studied here (Figure 9b). At low coverage, we observe likely screening effects (flat line) in all surfaces, similar to the (001) case. In addition, the adsorption energy per hydrogen atom becomes more positive (repulsive) with increasing monolayer coverage. In terms of the energy scale, the kinked facets (012) and (102) start at lower energies (-0.71 eV/H and -0.66 eV/H, respectively) compared to terrace surfaces, as they possess the most reactive stepped sites. As coverage increases, the stepped sites on (012) and (102) fill up first, followed by adsorption at hollow sites in relatively (unkinked) flat regions of the surface. In contrast, in (010) and (100), we observe initial adsorption at hollow sites followed by adsorption into bridge sites. For all surfaces, no exothermic adsorption occurs on top sites directly above U surface atoms.

2.6.2   Surface H/U phase diagram

All of our previous calculations were based on zero-temperature and zero-pressure optimizations. In order to connect our DFT calculations to actual thermodynamic measurements, we use the Python multiscale thermochemistry toolbox[78] (pMuTT) to generate the surface phase diagram for equilibrium hydrogen adsorption. pMuTT is a Python library designed to estimate various thermochemical and kinetic properties from ab-initio data for heterogeneous catalysis.

Here, the 2D phase diagram is computed by finding the U/H surface configuration from our set of calculations that exhibits the lowest Gibbs free energy at a specific temperature and pressure. The Gibbs free energy for each adsorbate-solid structure is estimated in the harmonic limit, where each adsorbed hydrogen is treated as an independent quantum-harmonic oscillator and its vibrational frequencies are computed via finite difference.

In Figure 10, each computed phase diagram depicts the monolayer coverage as a function of pressure and temperature. Configurations with high monolayer coverage are more favored at high pressure and low temperature, whereas the clean α-U surface is more prominent at low pressure and high temperature. As temperature increases, the entropy of the gas phase drives the desorption of hydrogen. Since hydrogen adsorption on an α-U surface is an exothermic reaction, the adsorption capacity increases with the decreasing temperature. We also notice that only the (102) facet shows a complete monolayer coverage at low temperatures (~150 K) and high pressure (>1 bar) over the range of conditions studied here. On the other hand, facets behave differently at various non-extreme cases. If we look at ambient conditions of 300 K and a realistic partial pressure of hydrogen gas in air (~10^{-4} bar), these stepped surfaces have higher monolayer coverages than the terrace facets. Specifically, the (012) and (102) facets have 0.56 ML coverage at these conditions, while (001), (100), and (010) have smaller monolayer coverages of 0.38 ML, 0.5 ML, and 0.25 ML, respectively. At 600 K, which is the operating temperature some nuclear reactors, and at ~10^{-4} bar hydrogen partial pressure, we notice a similar trend. We note that this temperature is above the transition point for α to β-UH_3 under atmospheric pressure. The stepped facets have a monolayer coverage of 0.17 ML, while the terrace surfaces have 0 ML coverage. Overall, we observe that monolayer coverage is generally more significant for stepped surfaces over all conditions studied here, consistent with the

conventional notion that these surfaces are likely much more reactive than their terrace

counterparts.
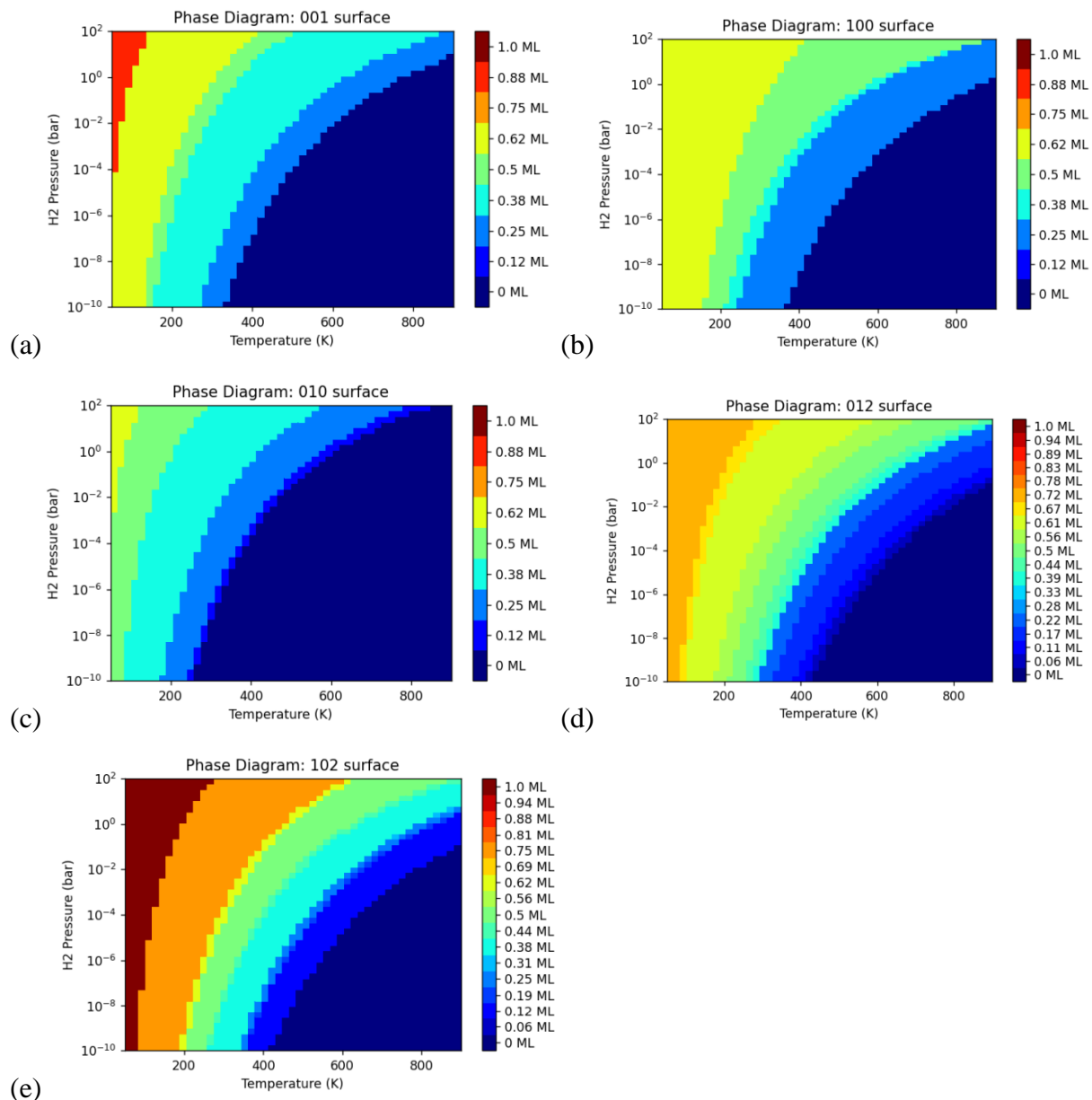
Figure 10: Ab-initio phase diagram of the H/α-U system generated by pMuTT, where the color represents the most stable configuration at a given temperature and pressure (a) (001), (b) (010), (c) (100), (d) (012), and (e) (102).

2.6.3 Subsurface adsorption as a function of surface coverage

We now investigate the possibility of surface adsorption either mitigating or enhancing subsurface absorption for a non-tensile loaded system. Our goals are to potentially find a cross-over point where hydrogen subsurface absorption becomes more favorable compared to surface adsorption for various facets of interest. We compute the energy to add hydrogen into either the first subsurface layer or on the surface itself for each ML coverage using the following equation:

$$E_{add\_surf/add\_subsurf} = E_{(U/NH+1)} - E_{(U/NH)} - \frac{1}{2} * E_{H_2} \qquad \text{Equation 4}$$

Here, $E_{(U/NH+1)}$ is the energy of the system with N+1 surface adsorbates (for $E_{add\ surf}$) or the energy of the system with N surface adsorbates and one subsurface hydrogen (for $E_{add\ subsurf}$), $E_{(U/NH)}$ is the total energy of the system with N surface adsorbates, and N is the number of adsorbed hydrogen atoms.

Table 4 shows the results for surface coverage of the (001) facet. At zero ML, adding an H atom to the surface is favored over the subsurface; in fact, subsurface adsorption is endothermic (+0.16 eV), while surface binding is exothermic (-0.57 eV). The most stable subsurface site at this point is used in subsequent calculations at higher coverages. Subsurface adsorption becomes exothermic at 1/8 ML coverage, though adding hydrogen to the surface is still more favored. This trend continues until 3/8 ML coverage, where the subsurface absorption (-0.36 eV) becomes preferred over surface absorption (-0.26 eV). Further details on the other low index terrace and kinked surfaces and the results are presented in the Supplemental Materials in Table S3. For all other facets studied here, subsurface absorption was either endothermic or still less favorable compared to the surface adsorption. As a result, (001) is the most likely candidate from our specific set that appears able to initiate subsurface hydriding at higher ML coverage.

Table 4: The adsorption energy to add a hydrogen atom on (2x1) α-U (001) surface or in the first subsurface layer as a function of coverage. $E_{add\_subsurf}$ denotes the energy required to add a hydrogen atom to the subsurface layer. E_{add_surf}(eV) represents the energy required to add a hydrogen on the top of the surface.

Surface Coverage	$E_{add\_subsurf}$ (eV)	E_{add_surf} (eV)
0	0.16	-0.57
1/8 (ML)	-0.02	-0.44
1/4 (ML)	-0.11	-0.43
3/8 (ML)	-0.36	-0.26
1/2 (ML)	-0.44	-0.21

2.7 Conclusion

In this work, we have investigated uranium hydriding from two perspectives: as a function of (1) applied tensile load on a α-U lattice and (2) formation of hydrogen monolayer coverage. First, we have analyzed the adsorption, absorption, and diffusion of hydrogen from surface to the first subsurface layer under applied symmetric tensile strain of up to 4%. Absorption sites closest to the surface were found to be the most favorable and exhibited either tetrahedral or square-pyramidal geometries. Both surface and subsurface binding energies were found to be sensitive to the hydrostatic elastic tensile strain, leading to lower values overall. In fact, a tensile strain of only 2% is required for subsurface absorption to become an exothermic process, though this value could shift somewhat depending on the choice of DFT functional and inclusion zero-point energy effects. In addition, the energy difference between surface adsorption and first layer subsurface absorption becomes less positive with increasing tensile strain. These tensile strain states are likely thermally accessible at ambient conditions. Similar to the binding energies, the diffusion barriers were found to be responsive to strain and exhibited an inverse linear relationship as a function of reaction energy, yielding a new predictive capability for this process.

We also explore the hydriding process from the perspective of formation of a hydrogen monolayer on the uranium surface. Coverage studies for all facets showed that the adsorption energy becomes more positive as more atoms hydrogen adsorb on the surface. We also observe that the kinked (012) and (102) facets initially exhibit more exothermic adsorption energies compared to the terrace surfaces. As depicted in our phase diagrams, they also show larger monolayer coverages with increasing pressure and temperature. Also, calculation of the energetic cost of inserting additional hydrogen inside the first subsurface layer of the (001) facet showed: (1) at 1/8 ML, subsurface absorption becomes exothermic, and (2) at 3/8 ML, this absorption is energetically favored over surface adsorption. This trend was only observed for the (001) facet in our study. Hence, we have found that high monolayer coverage is more likely on the (102) surface, with 56% coverage possible at ambient conditions. In contrast, (001) ML formation is more likely to enhance subsurface penetration.

CHAPTER 3: A REACTIVE MOLECULAR DYNAMICS MODEL FOR URANIUM/HYDROGEN CONTAINING SYSTEMS.

3.1 Introduction

Quantum based methods require immense computational resources per simulation step and, therefore, are generally limited to time scales on the order of picoseconds and system sizes of few hundreds of atoms. In order to study convergence of hydride initiation, nucleation, and growth, simulation cells of tens of thousands of atoms or greater run for nanosecond timescales or longer are typically required. A practical solution to ameliorate the system size and time scale limitations of quantum based methods is the development of computationally efficient molecular dynamics (MD) force fields that can approximate the underlying potential energy surface with accuracy comparable to DFT.

In this work, we detail our efforts to create a Chebyshev Interaction Model for Efficient Simulation (ChIMES) model for use in uranium hydriding studies. We start with a brief discussion of our DFT calculations as well as the ChIMES methodology. We then investigate different options for optimal values the ChIMES hyperparameters, including polynomials orders for different bodied interactions, the minimum and maximum interatomic distance cutoffs, and regularization parameters. We validate our model against previously determined computationally and experimental results, including lattice constants and the bulk moduli of different U-H phases, as well as defect energies for single and multiple defects of uranium vacancies, hydrogen interstitials, and hydrogen vacancies in uranium hydride. Finally, we present results from simulations with our optimum model, including determination of kinetic properties for bulk hydrogen diffusion through bulk α-U, and molecular dynamics simulation of diffusion

coefficients as a function of temperature. In all cases, we find that ChIMES yields a high degree of accuracy relative to DFT calculations on smaller system sizes.

3.2   Computational methods

3.2.1   Density Functional Theory (DFT)

All of our DFT calculations were performed using the Vienna ab initio simulation package code (VASP)[79–81] with the projector augmented wave (PAW) pseudopotentials[51,82] for U and H with the Perdew–Burke–Ernzerhof generalized gradient approximation (GGA-PBE) exchange-correlation functional.[83] In our work, we choose to focus on the high symmetry α-UH$_3$ phase, and leave results from α-UH$_3$ for validation. The energy cutoff for the planewave basis set was set to 500 eV based on convergence tests. Structural relaxations were performed until forces on all atoms were less than 0.01 eV/Å. A k-point mesh of 4x4x4 generated by the Monkhorst-Pack[52] method for integration over the Brillouin zone was used to generate the training set for both α-U and α-UH$_3$, discussed below.

Our full set of reference data contains 792 snapshots from the following DFT calculations: (1) short (0.5-1 ps) molecular dynamics simulations of α-U and α-UH$_3$ metallic systems at temperatures of 400 K and 1000 K and various hydrogen concentrations, (2) single-point calculations of isotropically distorted α-U and α-UH$_3$ lattices, and (3) supercell structures with uranium vacancies and images from optimized minimum energy path calculations of hydrogen diffusion in α-U. Pure uranium optimization calculations (atomic coordinates and lattice parameters) and DFT-MD simulations of interstitial-containing systems were performed on 4x2x3 supercell with initial lengths 11.209 x 11.687 x 14.711 Å. The interstitial simulations contained 94-96 uranium atoms and various hydrogen concentrations of hydrogen atoms (1-10 H atoms). We used a cubic supercell for defect-free α-UH$_3$ that a cubic supercell vector length of

12.363 Å and contained 54 U and 162 H atoms. All DFT-MD simulations were performed in the canonical ensemble (NVT) with timestep of 4.0 fs for pure systems of uranium and 0.20 fs for systems containing H, using Nose-Hoover thermostat chains[84–86] and periodic boundary conditions. For our training, uniformly spaced frames from the MD calculations were extracted every 150-200 fs in order to ensure that configurations were as statistically uncorrelated as possible.

3.2.2   Chebyshev Interaction Model for Efficient Simulation (ChIMES)

A detailed explanation of the ChIMES interaction model has been discussed elsewhere[22,87] and is summarized here, briefly. The design philosophy behind ChIMES comprises of mapping the DFT total energy onto linear combinations of many-body Chebyshev polynomials of the first kind. The ChIMES total energy is expressed as follows:

$$E_{\text{ChIMES}} = \sum_{i_1}^{n_a} {}^1E_{i_1} + \sum_{i_1>i_2}^{n_a} {}^2E_{i_1 i_2} + \sum_{i_1>i_2>i_3}^{n_a} {}^3E_{i_1 i_2 i_3} + \sum_{i_1>i_2>i_3>i_4}^{n_a} {}^4E_{i_1 i_2 i_3 i_4} + \text{higher bodied terms}$$

Here, ${}^1E_{i_1}$ corresponds to the one-body energies or atomic energy constants, ${}^2E_{i_1 i_2}$ to the two-body energies or pair-wise interactions, ${}^3E_{i_1 i_2 i_3}$ to the three-body energies or triplet interactions, and ${}^4E_{i_1 i_2 i_3 i_4}$ to the four-body energies or quadruplet interactions. The index n_a corresponds to the number of atoms in the system. In ChIMES, each of the greater than one-body terms is expressed as a polynomial sum. For example, the two-body term ${}^2E_{i_1 i_2}$ is expressed as:

$$^2E_{i_1 i_2} = f_{\text{p}}(r_{i_1 i_2}) + f_{\text{c}}^{e_{i_1} e_{i_2}}(r_{i_1 i_2}) \sum_{m=1}^{O_2} C_m^{e_{i_1} e_{i_2}} T_m\left(s_{i_1 i_2}^{e_{i_1} e_{i_2}}\right)$$

Here, the indices $\{e_{i_1}, e_{i_2}\}$ correspond to the element types of atoms i_1 and i_2 respectively. In this case, all pairwise distances $r_{i_1 i_2}$ are transformed over $\left[r_{min}^{e_{i_1} e_{i_2}}, r_{max}^{e_{i_1} e_{i_2}}\right]$ (e.g., the range of minimum and maximum values) to the scaled coordinate $s_{i_1 i_2}^{e_{i_1} e_{i_2}}$, which is restricted to the Chebyshev polynomial input variable range of [-1,1]. The function $f_c^{e_{i_1} e_{i_2}}(r_{i_1 i_2})$ assures smooth variation of the energy function at the boundary with a predefined maximum. The function $f_p(r_{i_1 i_2})$ is a penalty function that adds extra repulsion for situations where $r_{i_1 i_2} < r_{min}^{e_{i_1} e_{i_2}}$, (i.e., when the pairwise distance falls below the range of allowable inputs for the Chebyshev polynomials). The two-body sum is performed over all m dimers that exist within the $r_{max}^{e_{i_1} e_{i_2}}$ cutoff, and $\{C_m^{e_{i_1} e_{i_2}}\}$ are the set of optimized fitting coefficients that are permutationally invariant for each pair of atom types.

Higher bodied orthogonal polynomials for clusters greater than a dimer can be constructed by taking the tensorial product of the sum of the constituent $\binom{n}{2}$ unique pairwise polynomials of a that cluster. For example, a triplet or three-body cluster with the set of indices of $\{i_1, i_2, i_3\}$ contains $\binom{3}{2} = 3$ unique distances, namely $r_{i_1 i_2}, r_{i_1 i_3}, r_{i_2 i_3}$. Thus, a three-body polynomial of order m, n, o is constructed by first applying the transforms $r_{i_1 i_2} \longrightarrow s_{i_1 i_2}^{e_{i_1} e_{i_2}}$, $r_{i_1 i_3} \longrightarrow s_{i_1 i_3}^{e_{i_1} e_{i_3}}$, $r_{i_2 i_3} \longrightarrow s_{i_2 i_3}^{e_{i_2} e_{i_3}}$ and then taking the product $T_m\left(s_{i_1 i_2}^{e_{i_1} e_{i_2}}\right) T_p\left(s_{i_1 i_3}^{e_{i_1} e_{i_3}}\right) T_q\left(s_{i_2 i_3}^{e_{i_2} e_{i_3}}\right)$.

The three-body energy E_{ijk} can then be computed as the following linear combination:

$$^3E_{i_1 i_2 i_3} = f_c^{e_{i_1} e_{i_2}}(r_{i_1 i_2}) f_c^{e_{i_1} e_{i_3}}(r_{i_1 i_3}) f_c^{e_{i_2} e_{i_3}}(r_{i_2 i_3}) \sum_{m=0}^{O_3} \sum_{p=0}^{O_3} \sum_{q=0}^{O_{3*}} C_{mpq}^{e_{i_1} e_{i_2} e_{i_3}} T_m\left(s_{i_1 i_2}^{e_{i_1} e_{i_2}}\right) T_p\left(s_{i_1 i_3}^{e_{i_1} e_{i_3}}\right) T_q\left(s_{i_2 i_3}^{e_{i_2} e_{i_3}}\right).'$$

In this case, the set of $\{C_{mpq}^{e_{i_1} e_{i_2} e_{i_3}}\}$ correspond to the three-body fitting coefficients that are permutationally invariant to atom types as well as polynomial order. We also apply smoothly

varying cutoff functions to the three-body interactions, though penalty functions are omitted in this case and only included in the two-body energies. Finally, the '*' in the sum in equation above corresponds to the fact that we only include distinct triplets in the sum where $r_{i_1 i_2}$, $r_{i_1 i_3}$, and $r_{i_2 i_3}$ are all less than $r_{max}^{e_{i_1} e_{i_2}}$.

Greater than three-body terms in the ChIMES energy expression can be included in an equivalent manner. In practice a maximum of four-body terms are used due to prevent creating a combinatorically large polynomial space and potential parameter explosion.[22,43] In addition, ChIMES bears some resemblance to other polynomial expansion methods such as the Atomic Cluster Expansion[88,89] (ACE) and spectral neighbor analysis potential[90] (SNAP) methods. We note that the polynomial basis sets in these methods are atom-centered and are functionally different than the cluster-centered Chebyshev approach we employ here.

Similar to other atomic interaction potentials,[37,91–93] ChIMES models are trained through matching forces, energies, and stress tensor components. In general, training and validation data are generated through DFT optimized structures and MD simulations, though the possibility exists to include data form higher levels of theory. In addition, use of weights is frequently required due to the differing physical units of the forces, stresses, and energies and the number of data points per configuration. We can thus define an objective function for our optimization as follows:

$$F_{obj} \; = \; \frac{1}{N_d} \sum_{\tau=1}^{M} \left(\sum_{i=1}^{N_\tau} \sum_{\alpha=1}^{3} \left(w_F \Delta F_{\tau_{\alpha_i}} \right)^2 + \sum_{\alpha=1}^{3} \sum_{\beta \leq \alpha} \left(w_\sigma \Delta \sigma_{\tau_{\alpha\beta}} \right)^2 + (w_E \Delta E_\tau)^2 \right)$$

Here, the index τ corresponds to a specific training set configuration from the total set of N_τ configurations, i is the atomic index, and α and β are the cartesian directions. We use the index M to denote the total number of configurations in the training set, with N_d corresponding to the

total number of data points (e.g., forces, stress tensor components, and energies). In addition,

$\Delta F_{\tau_{\alpha_i}} = F_{\tau_{\alpha_i}}^{ChIMES} - F_{\tau_{\alpha_i}}^{DFT}$, $\Delta \sigma_{\tau_{\alpha\beta}} = \sigma_{\tau_{\alpha\beta}}^{ChIMES} - \sigma_{\tau_{\alpha\beta}}^{DFT}$, $\Delta E_{\tau} = E_{\tau}^{ChIMES} - E_{\tau}^{DFT}$. The value w_F is the

weight for forces, w_σ for the stress tensor components, and w_E for the energies.

3.2.3 Optimization and regularization

Regularization is an important concept that is utilized in order to avoid overfitting of the

trained data, and we refer to previous publications for further details.[49] In this work, we use the

Least Absolute Shrinkage and Selection Operator method (LASSO), a regularization technique

which adds a penalty equal to the absolute value of the magnitude of the fitting coefficients. In

turn, some coefficients can become zero and eliminated from the model. In this case, the

objective function F_{obj} is minimized with the following additional penalty on the sum of the

absolute values of the fitting coefficients C_i:

$$F_{obj} = N_d F_{obj} + 2\alpha' \sum_{i=1}^{N_p} |C_i|$$

where α' is the parameter that regularizes the magnitude of the fitting coefficients C_i, and N_p is

the total number of unique fitting parameters. In our work, we use LASSO as implemented

within the Least-Angle Regression (LARS) optimization method,[94] which is discussed in more

detail in Refs.[22,49]

3.3 Finding optimal parameters

ChIMES model development requires the definition of a number of *hyperparameters*,

i.e., user-chosen model parameters. These include the two, three, and four-body polynomial

orders, minimum and maximum atomic interaction distance cutoffs (r_{min} and r_{max}), and the

regularization method and degree of regularization. Figure 11 shows a workflow diagram for determination of optimal ChIMES model, which comprises exploring different combinations of the fitting parameters. Validation was determined through calculation of the root-mean-square (RMS) error of different physical properties that were not included in our fits, such as the bulk lattice constants, ground-state volumes for α-U and α-UH$_3$ systems, single uranium vacancy formation energy in pure U, and single hydrogen absorption interstitials in an α-U supercell.
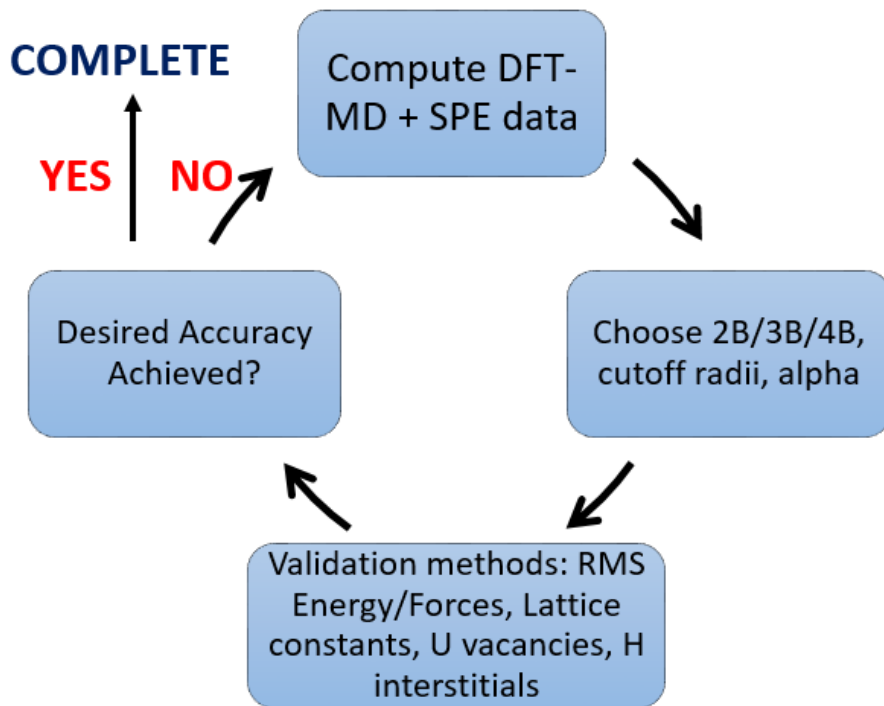
Figure 11: Flowchart for creation of ChIMES model.

3.3.1 Optimal interatomic interaction distances

The r_{min} value for each atomic pair (H-H, U-H, and U-U) was determined by scanning the data and finding the minimum interatomic interaction distances in our dataset (0.50 Å for H-H, 0.68 Å for U-H, and 1.07 Å for U-U pairs). Previous studies have shown that long-distance interactions play significant role in the energetics of the system. Therefore, the r_{max} atomic pair

values were uniformly set to the maximum allowed distance sampled in our training set (5.5 Å)
in order to satisfy the minimum image convention (i.e., one half of the shortest box length).

3.3.2   Sweep of polynomial order.

Given our choice of r_{min} and r_{max}, we have created multiple models with our training set
by sampling a range of polynomial orders for the two-body (2B), three-body (3B), and four-body
(4B) interactions. Here, we have looped over our workflow by sampling the 2B order a range of
$2 \leq O_{2B} \leq 18$, the 3B order over a range of $2 \leq O_{3B} \leq 14$, each with a step size of two. We have
also created a subset of potentials with the 4B order varied over range of $1 \leq O_{4B} \leq 4$, in steps of
one. Our preliminary studies showed that models with 2B only interactions produced
substantially diminished results for all validation tests, therefore, we decided sample models with
combinations of non-zero 2B/3B order values. The optimizations were performed with the
LASSO regularization of $\alpha = 10^{-3}$, similar to previous work.[22,49] In doing so, we are able to
validate a large number of independent models and eventually down select to our optimal choice.
In this section, we will first present results for models with 2B/3B polynomial models, followed
by studies with incorporation of the 4B terms.

a)

(b)
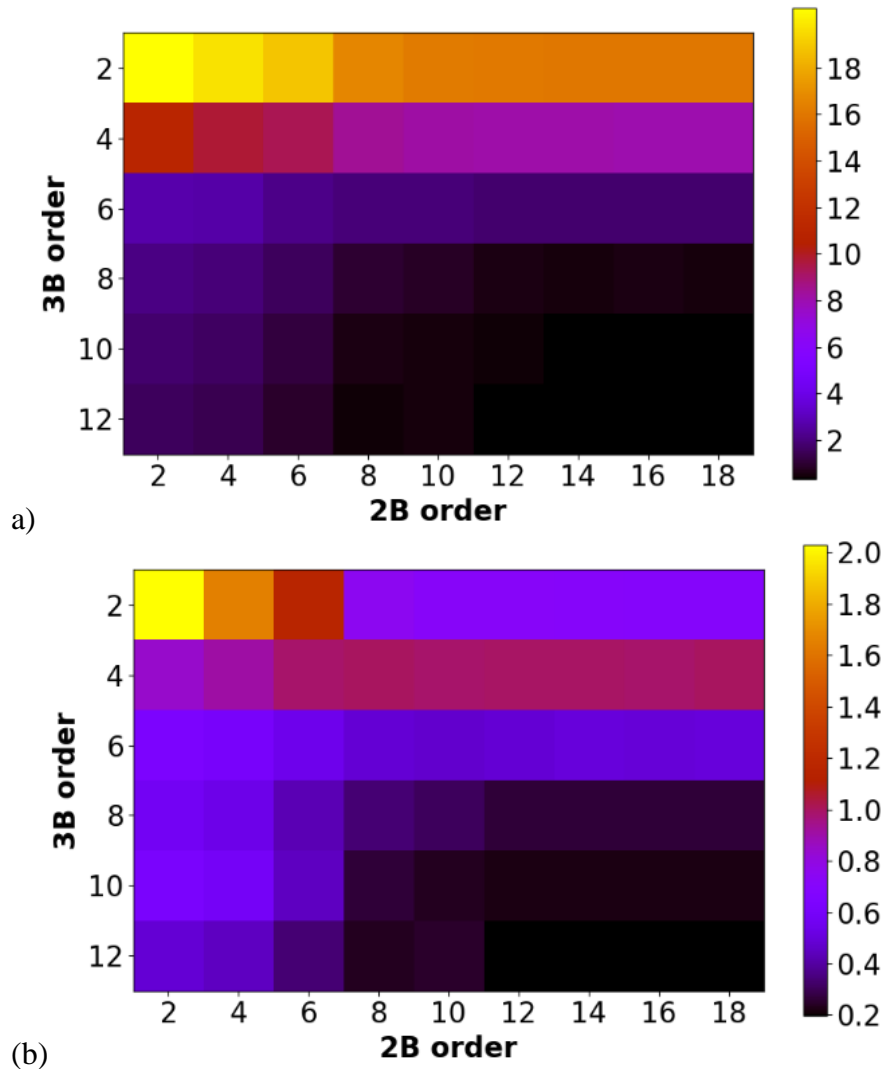
Figure 12: Results for training RMS errors using O_{2B} and O_{3B} Chebyshev polynomials. RMS error in the forces in units of eV/Å for (a) on U atoms and (b) on H atoms.

The results for the computed the root-mean-square (RMS) error in our training set for the atomic forces on hydrogen and uranium ions are shown in Figure 12. A more detailed RMS error results summary, which includes diagonal of the steps tensor and energies, are shown in the Supplementary Materials section. Unsurprisingly, the RMS error for forces of each fit decreases systematically with higher polynomial orders and higher bodied models. For example, a model with a set of $\{O_{2B}=8, O_{3B}=6\}$ yields fitting errors of 0.489 and 1.971 eV/Å for the forces acting

on H and U, respectively. On the other hand, a model with a set of $\{O_{2B}=18, O_{3B}=12\}$ produces substantially lower fitting errors of 0.197 and 0.342 eV/Å.

We notice similar trends for RMS errors of the diagonal of the stress tensor (e.g. 1.962 GPa for $\{O_{2B}=8, O_{3B}=6\}$ compared to 0.696 GPa for $\{O_{2B}=18, O_{3B}=12\}$ model). On the other hand, the opposite trends are observed for the total energy as increasing polynomial order yields to larger RMS values (e.g. 0.283 eV/U atom for $\{O_{2B}=8, O_{3B}=6\}$ and 0.421 eV/U atom for $\{O_{2B}=18, O_{3B}=12\}$ sets). We also note that models with higher orders of polynomials require more computational resources for the optimization process (e.g., about ten times the computational effort for the $\{O_{2B}=18, O_{3B}=12\}$ model discussed here), though the optimization remains relatively rapid (approximately 45 minutes on a single Intel Xeon E5-2695 processor for the above example).
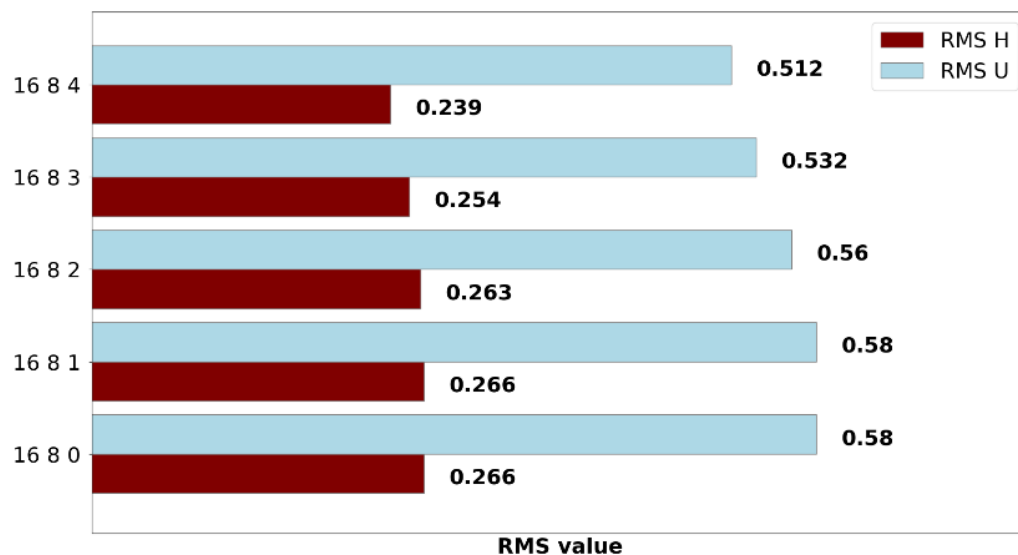
Figure 13. Results for training RMS error test with the inclusion of O_{4B} Chebyshev polynomials.

Incorporation of 4B interactions yields further training accuracy, where we have included terms up to $O_{4B}=4$, similar to previous work.[22,43] As shown in Figure 13 and Table S5 (Supplemental Information), we observe a monotonic decrease in RMS training error with

inclusion of higher four-body order in our model. We see RMS force errors of 0.580 eV/Å in U and 0.266 eV/Å in H for $\{O_{2B}=16, O_{3B}=8, O_{4B}=0\}$, 0.580 eV/Å and 0.266 eV/Å for $\{O_{2B}=16, O_{3B}=8, O_{4B}=1\}$, and 0.560 eV/Å and 0.263 eV/Å for $\{O_{2B}=16, O_{3B}=8, O_{4B}=2\}$. In this case, the RMS errors for the total energy diminish with increasing 4B polynomial order (e.g. 0.243 eV/U atom for $O_{4B}=0$, and 0.238 eV/U atom for $O_{4B}=3$ models), though these improvements are small. We notice that ChIMES model with $O_{4B}=0$ yields virtually identical results to those from $O_{4B}=1$, which occurs due to LASSO regularization setting these four-body parameters to zero. We observe some measurable reduction in the RMS errors for models with $O_{4B}=3$ or higher. We calculate the RMS force errors of 0.532 eV/Å in U and 0.254 eV/Å in H and the total energy error of 0.216 eV/atom for $\{O_{2B}=16, O_{3B}=8, O_{4B}=3\}$ and 0.512 eV/Å, 0.239 eV/Å, and 0.191 eV/U atom for $\{O_{2B}=16, O_{3B}=8, O_{4B}=4\}$. The opposite trends are observed in RMS errors of the diagonal of the stress tensor with increasing four-body order (e.g. 0.771, 0.771, 0.778, 0.789, 0.877 GPa).

Next, we perform a model down select through validation against a series of DFT-computed physical properties. These include the lattice constants, volume of the optimized unit cell of α-U and α-UH₃, vacancy formation energy in α-U, and hydrogen interstitial energy formation in α-U. We note that β-UH₃ was not part of this initial validation test because our training set only contained α-UH₃ data. As shown in **Error! Reference source not found.** (Supplemental Information), the complexity of the model in general reduces the absolute errors relative to DFT reference values. However, some validation tests are more sensitive than others. The lattice constants and equilibrium volume tests converge to sufficient accuracy without utilizing the four-body interactions. For example, a model with a set of $\{O_{2B}=6, O_{3B}=6\}$ yields absolute errors for lattice constants for α-U and α-UH₃ below 5.0%. Increasing the polynomial

order above these values leads to the reduction of relative errors in lattice, e.g., a model set of

{O_{2B}=18, O_{3B}=8} produces errors of 1.4% and 4.15% for α-U and 1.83% and 5.4% for α-UH$_3$

lattice and volume parameters.

A similar trend to a certain extent is observed for the formation energy of the uranium

vacancy in 4x2x3 α-U supercell. Here, we define the uranium vacancy formation energy is

defined as

$$E_v = E_{(n-1)U} - \left[\frac{n-1}{n}\right]E_{nU} \qquad \text{Equation 5}$$

where $E_{(n-1)U}$, E_{nU}, and n are the supercell energies for the defective and perfect systems, and n

is the number of uranium atoms, respectively. Models with polynomials orders above 10 for 2B

and 8 for the 3B interactions estimate vacancy energy with relative error of ±0.4 eV (or 25%

errors) or smaller, relative to the DFT computed value of 1.78 eV, with the best model {O_{2B}=12,

O_{3B}=8} of 1.80 eV with relative error of 0.9% .

While models with only two-body and three-body polynomial orders thus far appear to

provide sufficient complexity, we find that accurate prediction for the hydrogen interstitial in

α-U to be one of the most challenging properties in our initial validation set. The interstitial

formation energy is defined as

$$E_f = E_{U+nH} - E_U - 1/2\, nE_{H_2} \qquad \text{Equation 6}$$

where E_{U+nH}, E_U, and n are the supercell energies for the defective and perfect systems, and n is

the number of hydrogen atoms in the defective supercell, respectively. Here, we calculated the

hydrogen interstitial energy for the most stable site (square-pyramidal). Similar to other

validation tests, increasing the polynomial order of 2B and 3B interactions improve the results.

For example, a model with a set of {O_{2B}=6, O_{3B}=6} yields absolute errors of over 600%, while a

model $\{O_{2B}=12, O_{3B}=8\}$ estimates the interstitial energy of 0.22 eV (17% relative error). fairly

large polynomial orders (above 12 for 2B and 8 for 3B) are required to achieve relative errors

below 10% relative to the DFT computed value of 0.27 eV, with the best model $\{O_{2B}=18,$

$O_{3B}=8\}$ of 0.26 eV with relative error of 1.5% .

Lastly, we looked at the effect of including higher-body interactions on the validation

test. As shown in Table S5 (Supplemental Information), incorporation of the four-body

polynomial to the model set significantly improves the lattice constants for both of α-U and

α-UH₃. For example, adding the 4B terms to the model with a set of $\{O_{2B}=16, O_{3B}=8\}$ somewhat

improves relative errors 2.32% (α-U) and 2.13% (α-UH₃) for $\{O_{4B}=0\}$ and $\{O_{4B}=1\}$, 2.29%

(α-U) and 1.49% (α-UH₃) for $\{O_{4B}=2\}$, 2.23% (α-U) and 1.15% (α-UH₃) for $\{O_{4B}=3\}$, and 1.8%

(α-U) and 1.43% (α-UH₃) for $\{O_{4B}=4\}$. However, additional complexity to the model set

increases for other validation test. Errors in uranium vacancy formation energies systematically

increase from ~0.2 eV (0.9%) to ~0.4 eV (20.8%). Similar trends are observed in calculation of

the hydrogen interstitial with ~0.05 eV (16.8%) for $\{O_{4B}=0\}$ and $\{O_{4B}=1\}$, ~0.07 eV (24.3%) for

$\{O_{4B}=2\}$, ~0.18 eV (67.2%) for $\{O_{4B}=3\}$, and ~5.7 eV (>2000%) for $\{O_{4B}=4\}$. Overall, we find

comparable accuracy between the $\{O_{2B}=16, O_{3B}=8, O_{4B}=0\}$ model those with $\{O_{2B}=16, O_{3B}=8,$

$O_{4B} \leq 2\}$ for the solid phase lattice constants and point defect energies in this validation suite.

We compute some loss of accuracy for ChIMES models with values of $O_{4B} = 3$ or 4 for defect

formation energies. As a result, we choose to proceed with ChIMES models with 2B and 3B

interactions only, though the inclusion of non-zero 4B interactions has proven essential for

simulations of reactive materials over a broad range of thermodynamic conditions [REF-Pham,

JCP, 2020, HN3].[48]

As a result, at this stage we down select to a ChIMES model $\{O_{2B} = 16, O_{3B} = 8, O_{4B} = 2\}$. We find that this model achieves the correct balance of minimizing the RMS errors our training set while yielding accurate bulk parameters for α-U and α-UH$_3$. In particular, we find that this model is able to achieve accurate results for point defect properties, including hydrogen interstitial and uranium vacancy formation. Hence, we choose to proceed with this model for the remainder of our study.
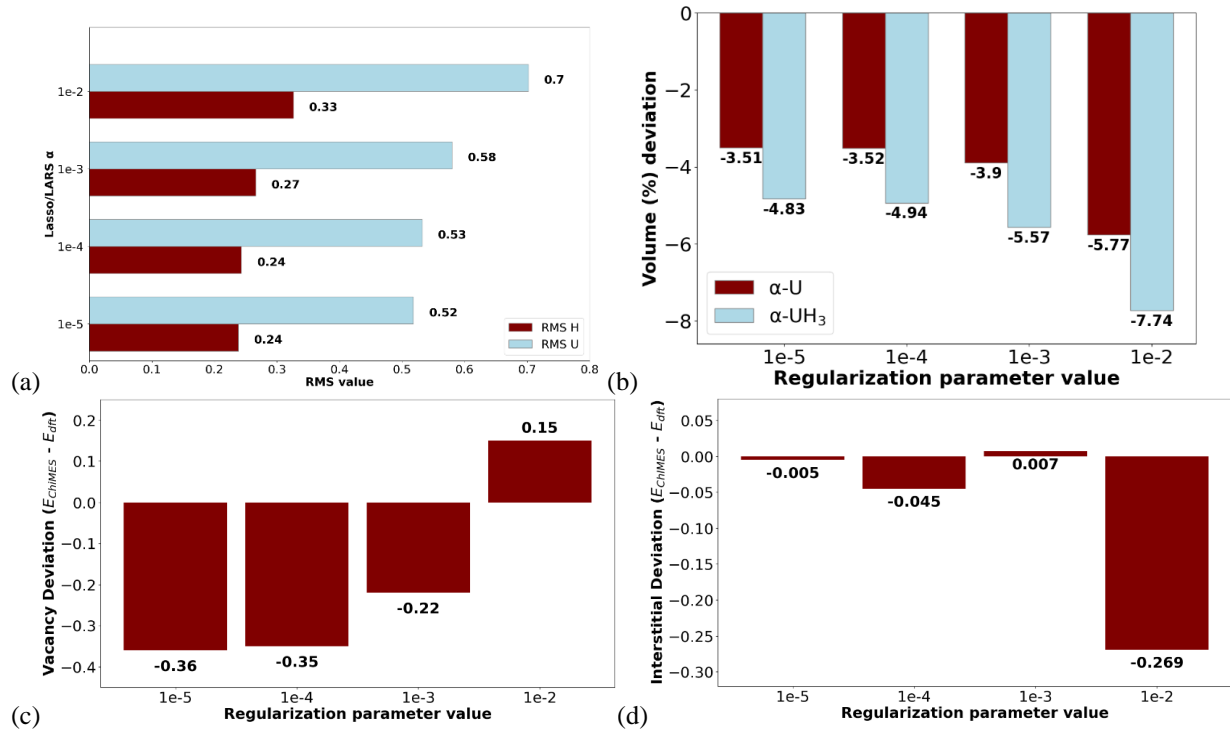
Figure 14. Results of validation tests using different values of LASSO/LARS parameter α. (a) Root mean square force errors (in eV/Å) on U and H atoms, (b) Percent deviation in volume of ChIMES estimated optimized unit cell from the PBE-DFT value in α-U and α-UH$_3$, (c) Defect energy formation deviation (in eV) of U vacancy in α-U 4x2x3 supercell, and (d) Defect energy formation deviation (in eV) of 1 H interstitial (square-pyramidal) in α-U 4x2x3 supercell.

3.3.3 Test of Regularization methods

Given our choice of the $r_{min}^{H-H} = 0.50$, $r_{min}^{U-H} = 0.68$, $r_{min}^{U-U} = 1.07$ and $r_{max}^{H-H} = 5.5$, $r_{max}^{U-H} = 5.5$, and $r_{max}^{U-U} = 5.5$ atomic interaction distance cutoffs and the ChIMES polynomial order $\{O_{2B}=16, O_{3B}=8, O_{4B}=0\}$, we also explored different options for determining the optimal

LASSO α parameter based on the validation errors (Figure 14). In this study, we varied α over the range of $10^{-5} \leq \alpha \leq 10^{-2}$. A more detailed summary of the results is shown in Table S6 in the Supplemental Materials section. In short, values of $\alpha = 10^{-2}$ and higher yields relatively high RMS errors in all of our validation tests, with RMS force errors (0.70 eV/Å in U and 0.33 eV/Å in H), lattice constants (-1.97% for α-U and -2.65% for α-UH₃), volume (-5.77% for α-U and -7.74% for α-UH₃), single uranium vacancy (-8.43%), single hydrogen interstitial (-100.37%). In contrast, the under-regularized value of $\alpha = 10^{-5}$ show considerable improvement with RMS force errors (0.52 eV/Å in U and 0.24 eV/Å in H), estimation of lattice parameters (-1.19% for α-U and -1.63% for α-UH₃), volume (-3.51% for α-U and -4.83% for α-UH₃), single uranium vacancy (20.17%), and single hydrogen interstitial (1.87%). However, as shown in Figure 14, the optimal balance of regularization and minimized training and validation occurs with $\alpha = 10^{-3}$. Here, compared to $\alpha = 10^{-5}$ model, we see slightly higher RMS force errors (0.52 vs 0.58 eV/Å in U and 0.24 vs 0.27 eV/Å in H), lattice (-1.19% vs -1.32% for α-U and -1.63% vs -1.9% for α-UH₃) and volume (-3.51% vs -3.90% for α-U and -4.83% vs -5.57% for α-UH₃) but significantly lower uranium vacancy formation energy errors (20.17% vs 12.53%) and similar hydrogen interstitial energy errors (1.87% vs 2.61%). Therefore, we chose to proceed with LASSO/LARS optimization with $\alpha = 10^{-3}$ as the best for our U-H model.

3.3.1 Final hyperparameters.

Our final set of hyperparameters values includes $\{r_{min}^{H-H} = 0.50, r_{min}^{H-U} = 0.68, r_{min}^{U-U} = 1.07, r_{max}^{H-H} = 5.5, r_{max}^{H-U} = 5.5, r_{max}^{U-U} = 5.5\}$ and $\{O_{2B} = 16, O_{3B} = 8, O_{4B} = 0\}$, optimized with LASSO/LARS with a regularization of $\alpha = 10^{-3}$. This model yields the RMS force errors of 0.27 eV/Å in hydrogen and 0.58 eV/Å in uranium, the total energy of 0.24 eV/U atom, and the

diagonal of the stress tensor of 0.77 GPa. For the remainder of our discussion, we will present results using this ChIMES model.

3.4 Bulk structural properties

Using optimal parameters, we performed analysis of the pure α-U and α-UH$_3$, and β-UH$_3$. The ChIMES potential predicted lattice parameters of these reference structures, listed in the Table 5, agree quite well with DFT results[95] and experimental data[96,97]. The results for the α-U and α-UH$_3$ bulk properties indicate that the ChIMES yields lattice constants with errors of only ~1.19% and ~1.7% from the DFT and the experimentally determined values, respectively. Volumetric (per unit U atom) of the optimized unit cell and the bulk modulus parameters are slightly lower than PBE-determined results, with errors of 3.9% and 12.8% for α-U and 5.57 % and 21.4% for α-UH$_3$. In each case, the bulk modulus was estimated from energy vs. volume curve computed over a range of -13 to 24 GPa, followed by regression to a Birch-Murnaghan[98] model. We note that β-UH$_3$ data was not included in the training set in order to benchmark the transferability of the ChIMES potential. Our ChIMES potential is in excellent agreement with DFT-calculated and experimental values for β-UH$_3$, with relative errors of 2.1% and 3.0% for the lattice constant, and 6.1% and 8.7% for the unit cell volume, respectively. We compute an error of 0.9% for the bulk modulus relative to DFT. In addition, ChIMES yields the correct energetic ordering of the uranium hydride phases, with β-UH$_3$ predicted to be 0.03 eV/U atom lower in energy than α-UH$_3$, compared to the DFT computed result of 0.02 eV/U atom.

Table 5: Lattice parameters, unit cell volumes (V) per U atom, and bulk moduli (B) for α-U, α-UH₃, and β-UH₃ predicted by the ChIMES potential. Present results are compared with experimental and computational calculations.

Structure	Method	a (Å)	b (Å)	c (Å)	V (Å³)	B (GPa)
α-U (ortho)	PBE	2.81	5.87	4.92	20.29	148
	ChIMES	2.78	5.79	4.86	19.53	156
	Exp	2.84	5.87	4.94	20.59	125
α-UH₃ (cubic)	PBE	4.12	4.12	4.12	34.97	106
	ChIMES	4.05	4.05	4.05	33.22	135
	Exp	4.16	4.16	4.16	36	---
β-UH₃ (cubic)	PBE	6.59	6.59	6.59	35.77	106
	ChIMES	6.45	6.45	6.45	33.54	115
	Exp	6.65	6.65	6.65	36.76	---

3.5 Additional point defect formation energies in α-U.

3.5.1 Uranium vacancy energies as a function of system size.

In order to further validate our optimal ChIMES parameterization, we choose to compute the formation energies of vacancies in α-U as a function of supercell size, thus estimating the effect of uranium vacancy concentration. As shown in Figure 15, the vacancy formation energy shows some dependence on the uranium vacancy concentration in the bulk structure. The DFT estimated vacancy values were found to be 2.03 eV for (2x1x1), 1.93 eV for (2x2x1), 1.92 eV for (2x2x2), 1.90 eV for (3x2x2), 1.81 eV for (4x2x2), and 1.78 eV for (4x2x3) supercells. The 0.25 eV decrease in the vacancy formation energy with the increase of the system size from (2x1x1) to (4x2x3) indicates that there are strain-induced interactions around the defect at higher concentrations.
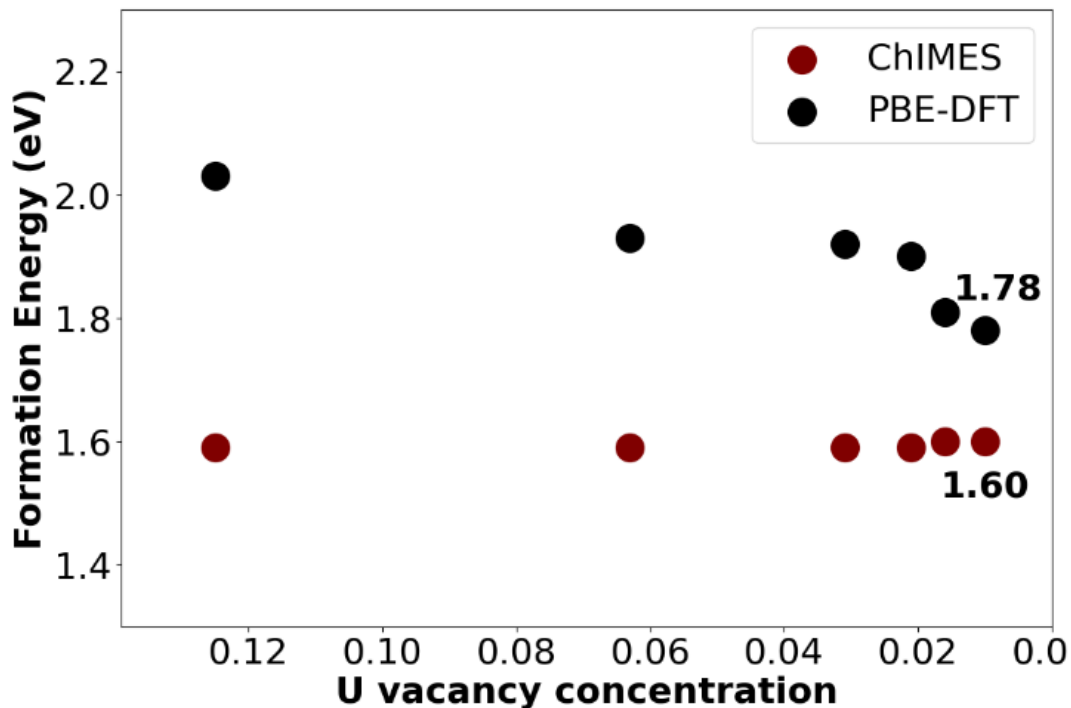
Figure 15: Uranium vacancy formation energy for α-U at various concentrations using ChIMES potential.

Our ChIMES calculated value in the dilute limit of 1.56 eV is 0.22 eV lower (~12% error) than our computed DFT value and about ~0.13-0.39 eV lower than other published DFT results of 1.95 eV (Taylor[28]), 1.69 eV (Wirth[99]), and 1.86 eV (Beeler[100]). We found that underestimation of the U vacancy energy was typical for all ChIMES models created in our study. We also observe a weaker dependence on vacancy formation energy as a function of defect concentration, where the curve from ChIMES is relatively flat compared to DFT. This yields somewhat larger error between the DFT and those predicted by ChIMES potentials at higher vacancy concentrations. This could be attributed to the lack of training data in our ChIMES model for multiple vacancies. We note that by positron annihilation experimentally determined vacancy formation energy[101] of 1.20±0.25 eV is relatively lower than DFT or ChIMES. In addition, DFT calculations could vary depending on choice of functional and dispersion interaction model.

3.5.2 Multiple hydrogen interstitial formation energies in α-U.

In this study, as shown in Figure 16, we have calculated the interstitial energies for (a) a low-energy interstitial hydrogen at the square-pyramidal (sq) position, a pair of hydrogen atoms at nearby sq sites in 2 different directions (b and c), and a hydrogen pair located ~5 Å apart (d). The square-pyramidal interstitial site occurs where the H atom is coordinated by five U atoms from the lattice (Figure 16a and Table 6). ChIMES predicts a formation energy for this site of 0.28 eV, which agrees within 0.01 of our result from DFT and is also in a good agreement with previously published results of 0.319 eV using 4x2x2 supercell (64 U atoms).[102] In addition, our ChIMES model predicts hydrogen interstitial formation energies that compare well to DFT for higher energy sites (not shown here), including the tetrahedral site with a value of 0.32 eV (~0.02 eV or 9.6% error) and the octahedral site with a value of 0.50 eV (~0.05 eV or 10.2% error). The tetrahedral and octahedral sites are relatively low energy and are likely thermally accessible under ambient conditions.

Table 6. Hydrogen interstitial formation energies (in eV) in α-U (4x2x3) supercell. The labeled systems are pictorially shown in Figure 16. Percent deviation compared to the DFT-PBE estimated value is shown in parenthesis.

System	DFT-PBE (eV)	ChIMES (eV)
sq (Figure 16a)	0.27	0.28 (3.7%)
sq_sq_1 (Figure 16b)	0.64	0.50 (-21.8%)
sq_sq_2 (Figure 16c)	0.51	0.58 (13.7%)
sq_sq_3 (Figure 16d)	0.52	0.65 (25.0%)
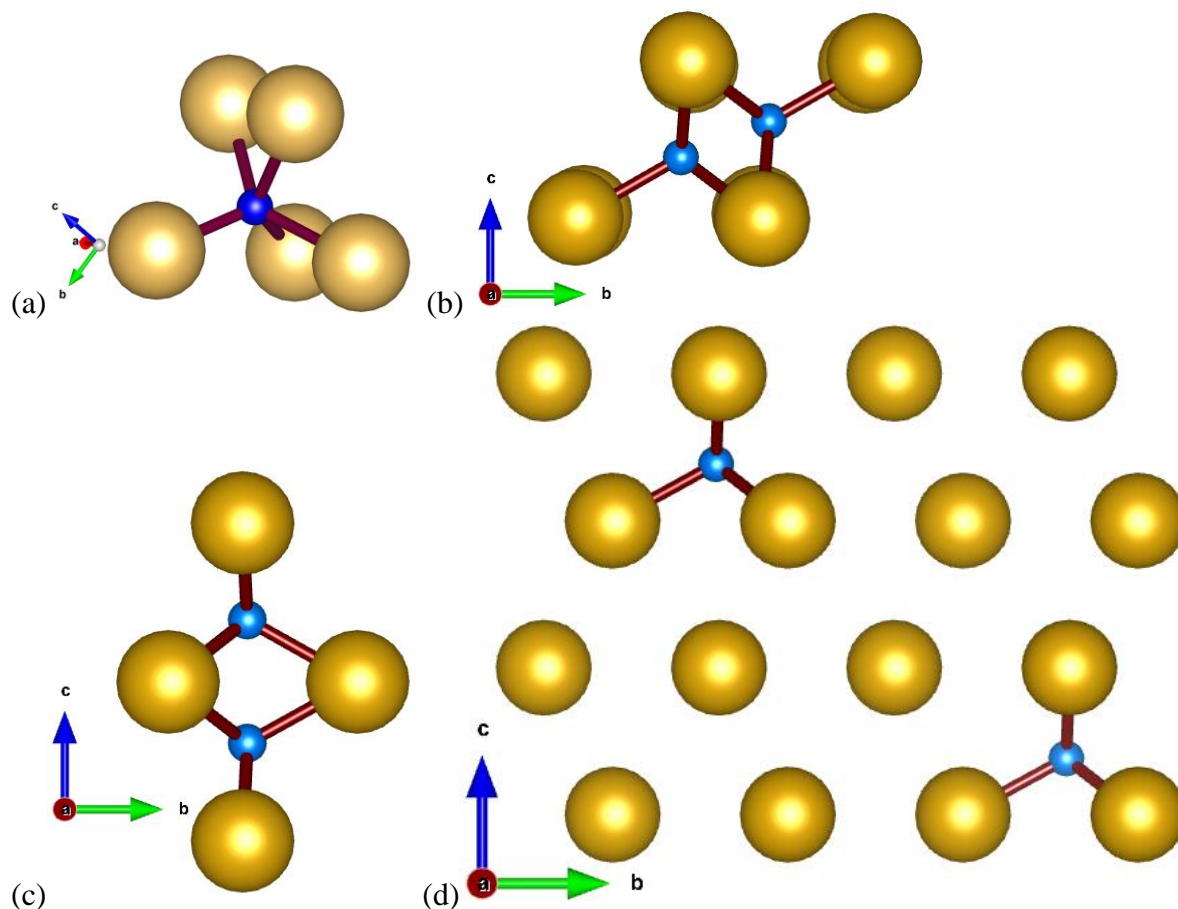
Figure 16. Hydrogen interstitial systems (a) square pyramidal site, (b) sq_sq_1, (c) sq_sq_2, and (d) sq_sq_3 systems.

We now examine our ChIMES model in terms of different double hydrogen interstitials in α-U with a 4x2x3 supercell (Table 6 and Figure 16). For the short-range double interstitial system (two H interstitials in nearest-neighbor sites, labeled sq_sq_1) contains hydrogen atoms about 1.5 Å apart from each other. The ChIMES formation energy of 0.50 eV has an error of 0.14 eV, relative to DFT. On the other hand, the medium-range double interstitial system (H interstitials in next-nearest neighbor sites, labeled sq_sq_2) has an inter-hydrogen separation of 2.1 Å. Here, ChIMES yields a formation energy of 0.58 eV, with an error of 0.07 relative to DFT. Finally, the formation energy for the longer-range system (H interstitials several lattice spacings apart, labeled sq_sq_3) is also in relative agreement with the DFT value of 0.65 eV (a

relative error of 0.17 eV). Overall, these results indicate that ChIMES can yield accurate physical quantities related to bulk hydrogen absorption within α-U lattices.

3.5.3 Hydrogen vacancy in α-UH₃ as a function of concentration.

In addition to the uranium vacancy and hydrogen interstitials in α-U, we have also computed the hydrogen vacancy formation energy E_{vac} in α-UH₃, defined as

$$E_{vac} = E_{def} + 1/2\, E_{H_2} - E_{perf} \qquad \text{Equation 7}$$

where E_{def} and E_{perf} are the supercell energies for the defective and perfect systems, respectively, and E_{H_2} is the energy of the isolated hydrogen molecule. The hydrogen vacancy formation energies were not part of our validation test and have been evaluated at various concentrations. Here, we begin with α-UH₃ supercell size of 3x3x3 (54U + 162H atoms), sequentially remove random hydrogen(s), and optimize the atomic positions. As shown in Figure 17, the defect formation energy is relatively constant over the concentration range probed in our analysis. The calculated DFT E_{vac} value for bulk α-UH₃ phase is 0.90 eV. The ChIMES predicted hydrogen vacancy energy (0.85 eV) slightly underpredicts this value with a relative error of 0.05 eV. However, we observe that both ChIMES and DFT results are relatively flat as a function of hydrogen vacancy concentration. Hence, it is likely that the errors in our ChIMES here are systematic.

All of the results presented in this subsection indicate that ChIMES exhibits a high degree of accuracy for different bulk uranium and UH₃ properties. In particular, our model yields accurate results for a number of validation that were not included in our training set. This includes the relative energetic ordering of the two UH₃ phases, uranium vacancy and hydrogen interstitial formation energies in α-U as under varying system sizes and concentrations, and

hydrogen vacancy formation over a range of concentrations in α-UH$_3$. These all indicate that ChIMES can yield close to DFT accuracy for the energetics of U/H-containing systems under a variety of conditions, allowing us to use our model for kinetic and molecular dynamics calculations relevant to the hydriding process.
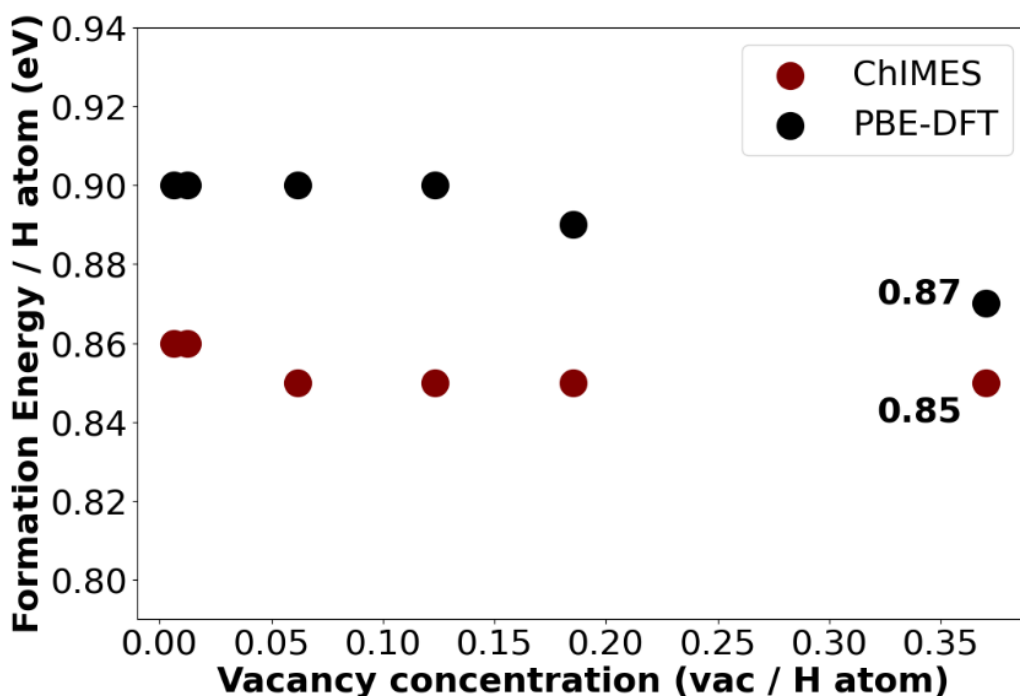
Figure 17. Hydrogen vacancy formation energy for α-UH$_3$ at various concentrations.

3.6 Hydrogen hopping barrier in α-U bulk.

We now compute kinetic parameters for hydrogen diffusion between square pyramidal sites within bulk α-U. The atomic hydrogen diffusion minimum energy pathways (MEP) were calculated via the climbing image nudged elastic band (NEB) method.[103] Here, a chain of 3-5 linearly interpolated images along an initial pathway between given initial and final absorption sites was relaxed to determine the MEP and its corresponding saddle point. The images were relaxed along the energy pathway until the maximum residual forces on each atom was less than

0.01 eV/Å. The transition state was confirmed by presence of one imaginary vibrational frequency.

We have studied bulk diffusion between neighboring low-energy square-pyramidal sites within the α-U lattice. Two main pathways were identified: (1) along the <011> lattice direction, and (2) along the <001> direction, as illustrated in Figure 18. Results of this study (Figure 19) show that diffusion barrier and the jump distance depend on the pathway direction. For pathway 1, the hopping distance between sites for hydrogen migration is 1.5 Å and the DFT barrier height is 0.14 eV. For pathway 2, the hopping distance is 2.1 Å and the DFT estimated barrier is 0.38 eV. For comparison, ChIMES yields a calculated barrier is 0.09 eV (0.05 eV relative error) for pathway 1 and 0.39 eV (0.01 eV residual error) for pathway 2, indicative of a high degree of accuracy. These barrier values are in close proximity with the experimental result of 0.280 eV,[8] which likely represents an average quantity for an imperfect crystalline system.
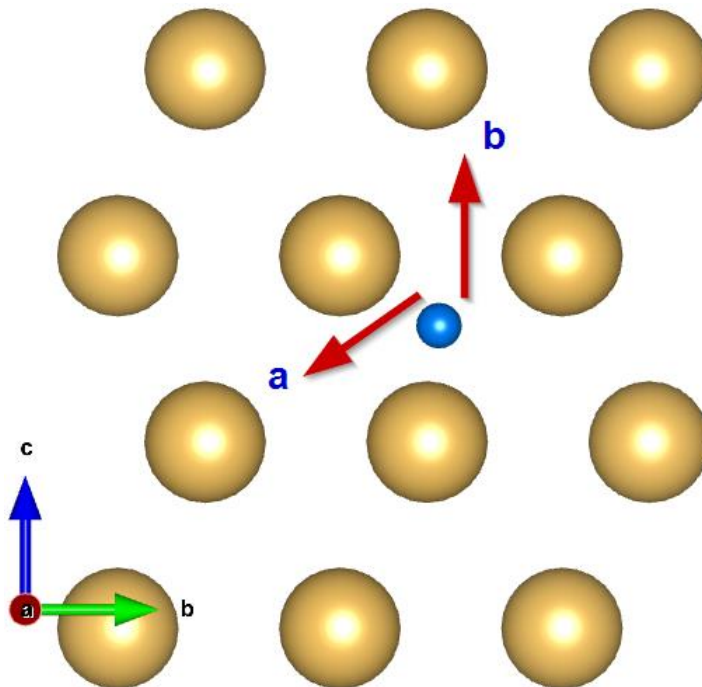
Figure 18: Pictorial representation of two potential pathways: (a) pathway along <011> direction, (b) pathway along <001>.

(a)

(b)
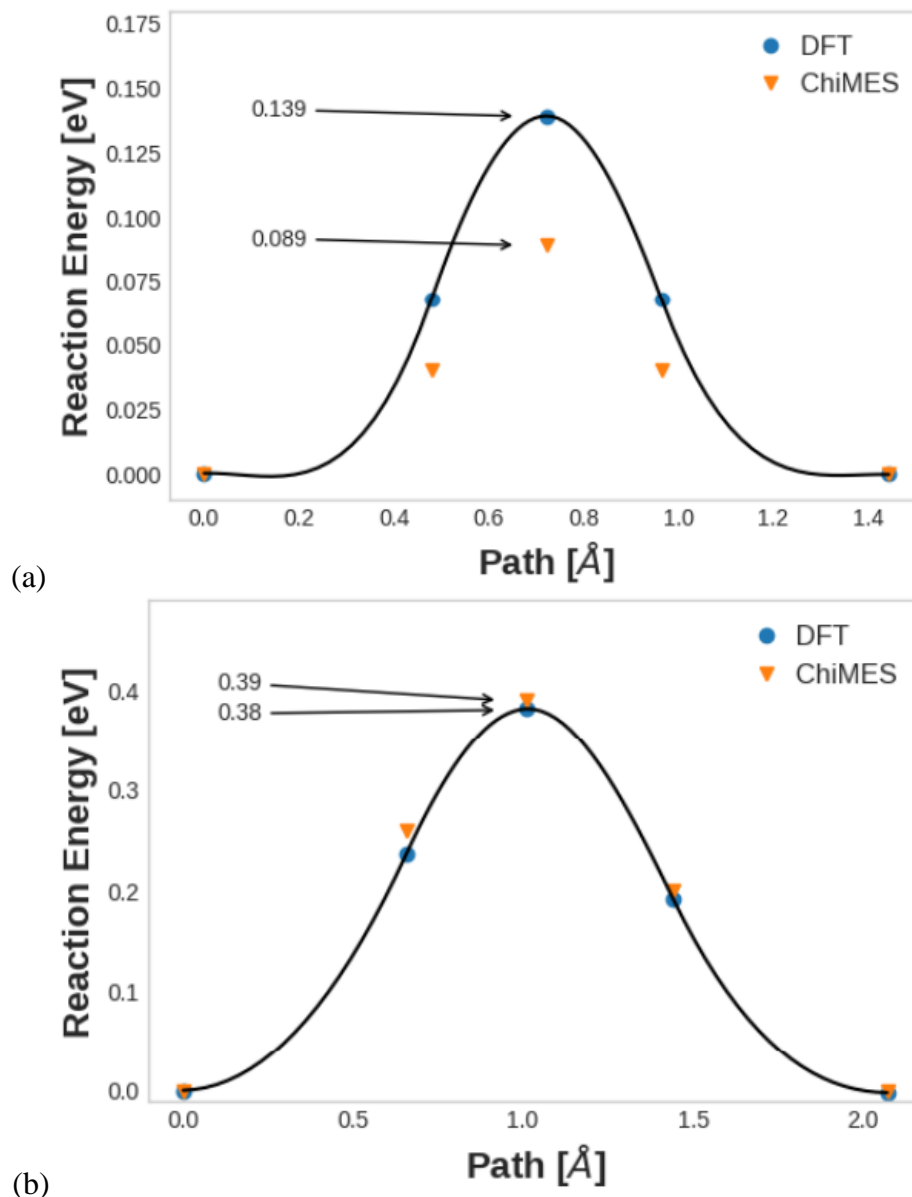
Figure 19: NEB predicted barrier for hydrogen diffusion from sqpy to another nearby sqpy interstitial site along (a) <011> direction and (b) <001>.

3.7 Molecular dynamics

We now evaluate the reliability of our ChIMES model for molecular dynamic (MD) simulations by comparing energies with DFT along a computed trajectory. This was performed by first computing a short NVT MD simulation with ChIMES of 5x2x3 α-U supercell (120 U atoms) at 400 K. The trajectory was computed for ~20 picosecond with a time step of 4.0

femtoseconds. We then extracted images after every 100th MD step and calculated single point

energies using DFT in order to determine errors in the resulting energies. Figure 20 shows the

ChIMES predicted energies of these structures along the MD trajectory in comparison to their

DFT reference. We observe accurate system energies from ChIMES, with slight overestimations

of the DFT values with relative errors up to 0.05 eV/atom. Similar MD studies were performed

for α-UH_3 (54U + 162H) and β-UH_3 (64U + 192H) systems, shown in Figure 21. In each of these

systems, we computed trajectories for ~5 ps with a time step of 0.2 fs and collecting images

every 1000 steps. For both of these systems, we observe errors in the system energies 0.10 eV/U

atom in α-UH_3 and below 0.15 eV/U atom in β-UH_3.
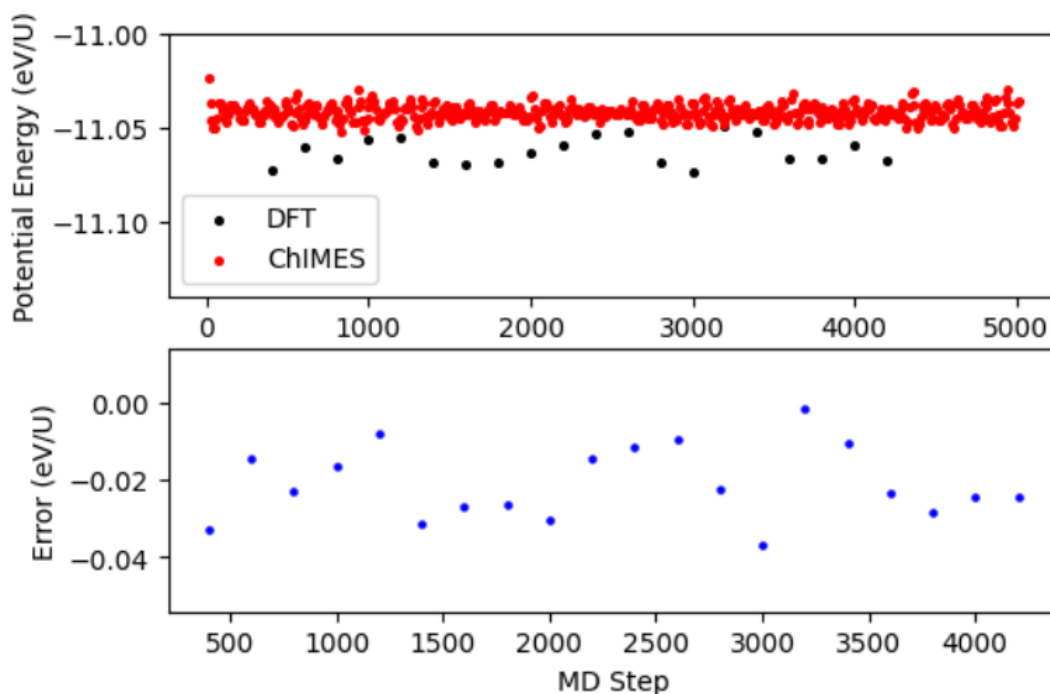
Figure 20: Comparison of energy predicted by the ChIMES and DFT along the same MD trajectory in α-U.
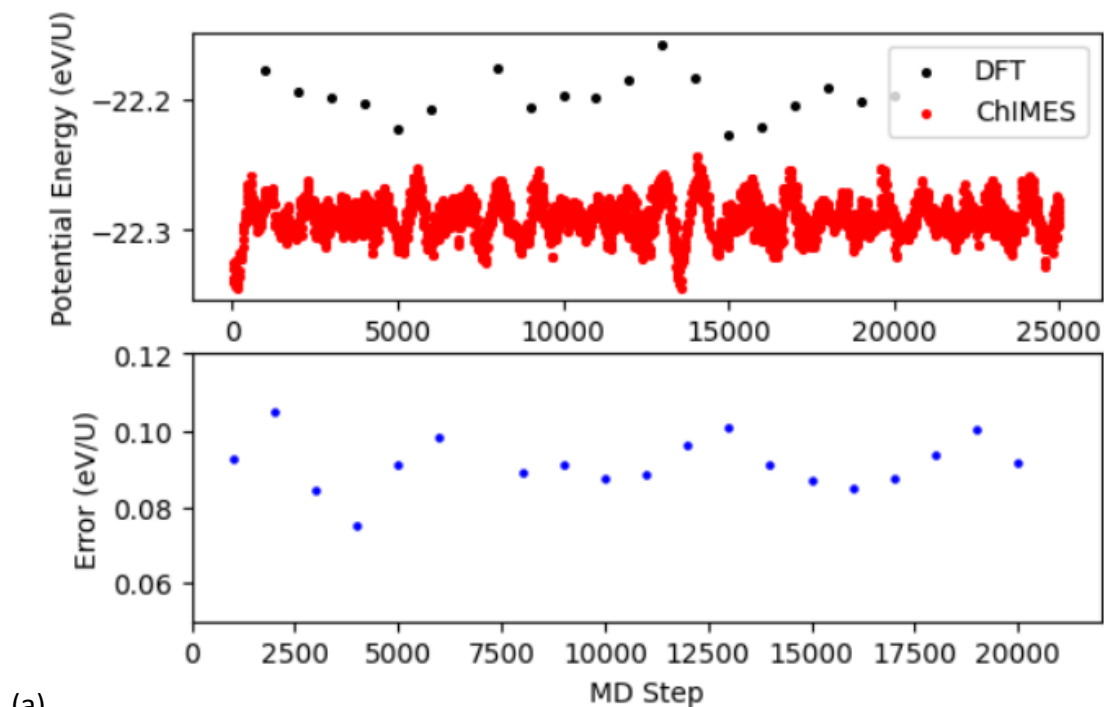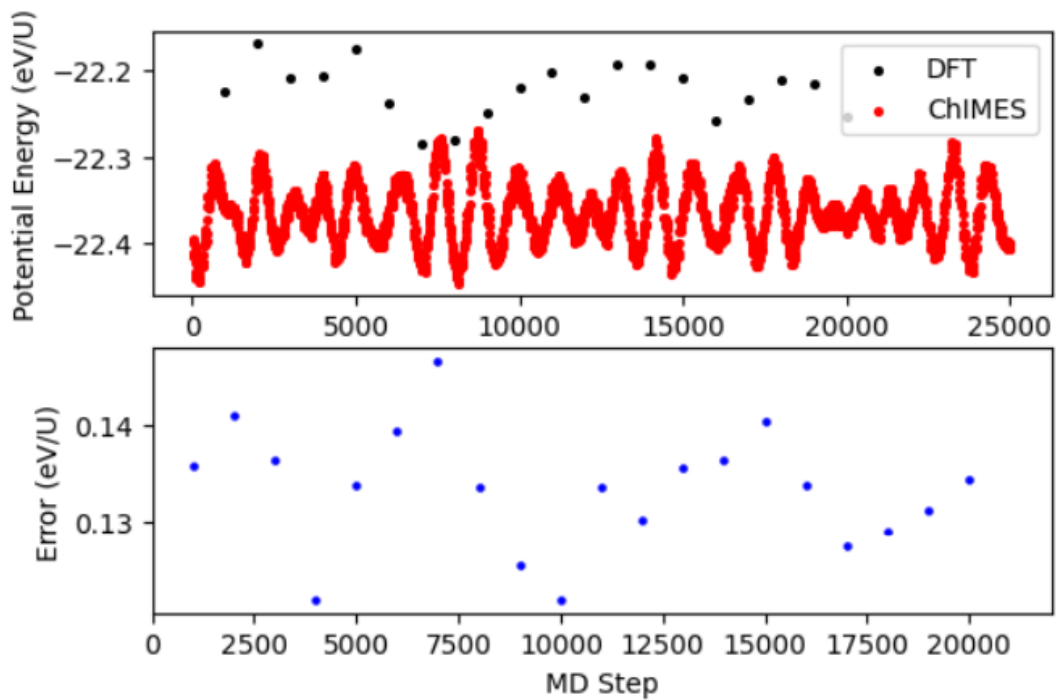
Figure 21. Comparison of energy predicted by the ChIMES and DFT along the same MD trajectory in (a) α-UH₃ and (b) β-UH₃.

We also have used MD simulations with our ChIMES potential to investigate the frequency of sites the hydrogen interstitial hopping in bulk α-U. For this study, we have

performed ten 10 ps NVT MD simulations over a range of temperatures (100-1000K) of one

atomic hydrogen atom in a large α-U supercell (840U + 1H atoms) with a time step of 0.2 fs.

Hydrogen location was monitored based on the number of U atoms surrounding interstitial H

atom a given radius. In this case, a value of 2.85 Å centered at each site was chosen based on the

largest possible U-H distance, which is the out of plane distance along the stretched axis in the

octahedral site (~2.65 A˚). An additional 0.2 Å was added in order to compensate for thermal

fluctuations of lattice sites during the MD simulation. Hydrogen locations were determined at

each step and residency time was monitored during the molecular dynamics simulation.
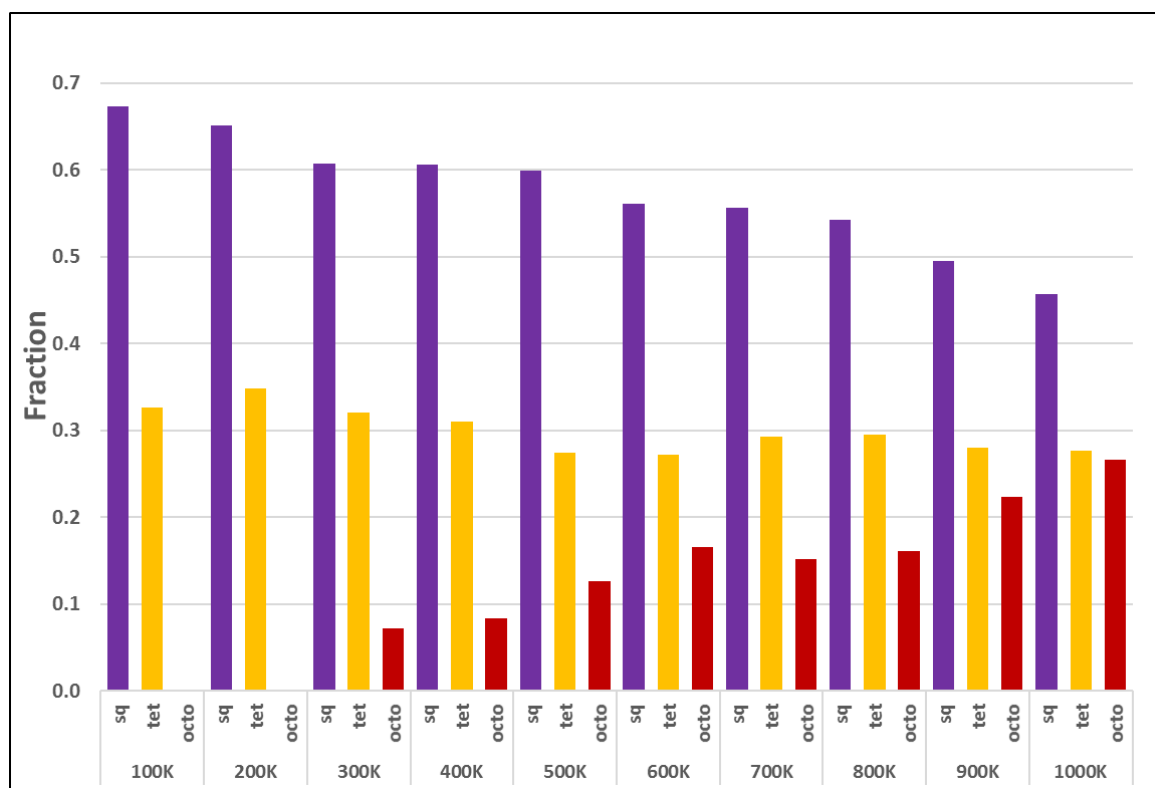
Figure 22. Interstitial site type analysis.

As shown in Figure 22, hydrogen predominantly occupies the square-pyramidal

interstitial site for all temperatures of our study with residence of over 50%. The square-

pyramidal is the most stable interstitial site in pure uranium bulk, which is confirmed by our

ChIMES potential and DFT studies and has the shortest average residency time of 1.7 fs. This short residency time is commensurate with the relatively low hopping barriers computed for both <011> and <001> diffusion pathways. As temperature increases, the fraction of the square-pyramidal site decreases from 0.67 (100 K) to 0.46 (1000 K), as the other sites – tetrahedral (+0.05 eV) and octahedral (+0.22 eV than square-pyramidal) – become more energetically accessible. The second most stable interstitial tetrahedral site shows occupancy fraction of ~0.25, which remains constant for all range of temperatures, and the average residency time of 4.44 fs. On the other hand, we observe the first occurrence of the octahedral site at a temperature of 300 K. As the system temperature increases, the frequency of the octahedral site also increases, most likely at the expense of the square-pyramidal site. The octahedral was found to have the longest residency time of 8.39 fs. Overall, all residency times computed here are exceedingly short at ambient conditions. This indicates that hydrogen are highly mobile in the pure metal lattice, which likely has ramifications for hydriding initiation.

3.8 Hydrogen diffusivity

Finally, we have computed hydrogen diffusion coefficients in pristine α-U as a function of temperature from MD simulations. During the constant temperature MD simulation, the mean square displacement (MSD) of hydrogen atoms was calculated and the diffusion coefficient was determined from the standard Einstein-Smoluchowski relation. Each MD simulation (840 U + 20 H atoms with supercell dimensions of 19.19 x 29.23 x 29.24, similar to α-U at ambient density) was run for 10 ps with time step of 0.2 fs. The MSD was averaged over a time interval of at least 5ps for each calculation. In addition, the diffusivities were then estimated by linear regression of the MSDs over a temperature range of 300 K to 1000 K and then fit to the Arrhenius equation:

$$D(T) = D_0 \, exp\left(-\frac{E_a}{k_B T}\right) \hspace{2cm} \text{Equation 8}$$

Here, D_0 is a prefactor, k_B is the Boltzmann constant and E_a is a total hydrogen diffusion

activation energy. The Arrhenius plot of hydrogen diffusivity as a function of temperature is

shown in Figure 23. Our regression analysis yields a value of D_0 of 2.73×10^{-3} cm^2/s, which is

in very good agreement with the experimentally determined result of 1.43×10^{-3} cm^2/s.[8]

However, ChIMES yields an overall diffusion barrier of 0.13 eV, which a bit lower than

experimental value of 0.28 eV (Mallett[8]). This could be attributed to the environmental

conditions surrounding the metal during experimentation, such as presence of the surface cracks,

grain-boundaries, and the passive layer of oxides, oxycarbides, and water, while our

computational simulation currently probes a defect-free crystal.
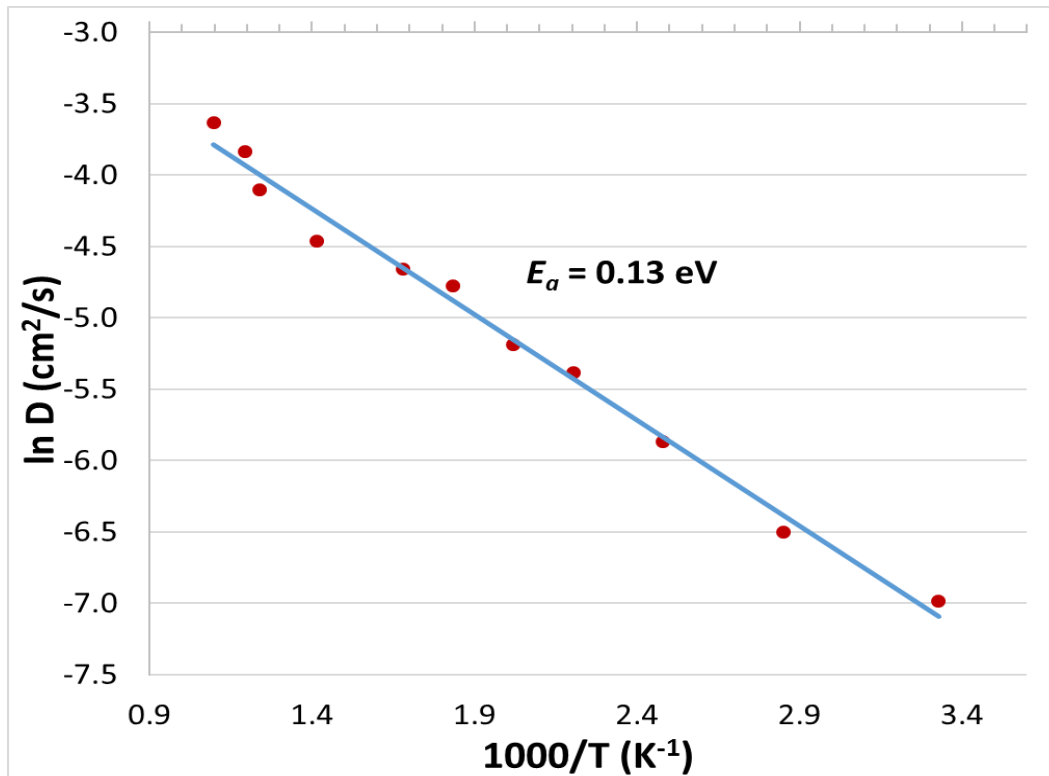
Figure 23: Arrhenius plot of hydrogen diffusivity at temperatures ranging from 300 to 1000 K.

3.9 Conclusion

In this work, we have created a workflow for the ChIMES reactive force field model based on linear combinations of Chebyshev polynomials. Optimal ChIMES parameters can be determined extremely rapidly in a semi-automated approach by varying the minimum and maximum pairwise interaction radius, the polynomial order, and the type of the regularization. We observe that ChIMES yields accuracy that is comparable to DFT calculations in predicting Overall we find that our ChIMES model yields comparable accuracy to DFT for the U-H containing systems studied here. This includes thermodynamic data, such as the bulk structural parameters of α-U, α-UH$_3$, and β-UH$_3$, the relative energetic ordering of UH$_3$ phases, and the bulk moduli of these three phases. Our model also yields accurate defect formation energies in both α-U and α-UH$_3$ over a range of defect concentrations. Finally, ChIMES yields accurate kinetic data for hydrogen interstitial hops in an a-U lattice as well as bulk diffusivity over a broad temperature range.

CHAPTER 4: CONCLUSIONS

In this thesis, we have first presented a systematic study of possible mechanisms for formation of the hydride using quantum simulations via Kohn-Sham Density Functional Theory (DFT). Specifically, we have started with calculations of the surface adsorption, subsurface absorption, and the inter-layer diffusion of atomic hydrogen as a function of applied tensile strain and monolayer coverage. We find that hydrogen subsurface absorption becomes favorable (exothermic) with a tensile strain of only 2%, and these tensile strains of that magnitude are likely thermally accessible at ambient conditions. Similarly, surface to subsurface diffusion barriers were found to be responsive to tensile strain, exhibiting an inverse linear relationship between the two and thus yielding a new predictive capability for this process. On the other hand, monolayer coverage studies for all surfaces examined in this work demonstrate that the adsorption energy becomes more positive as more atoms hydrogen adsorb on the surface. Also, we find that kinked (012) and (102) facets initially exhibit a larger degree of exothermic adsorption compared to the terrace surfaces. Monolayer coverage on the most stable (001) surface can enhance subsurface absorption as well.

In order to run dynamics on significantly larger systems (e.g., thousands of atoms and nanosecond timescales or longer), we have developed a reactive force field through the Chebyshev Interaction Model for Efficient Simulation (ChIMES). Our ChIMES model yields accuracy that is comparable to DFT for numerous of physical parameters, including lattice constants of α-U, α-UH$_3$, and β-UH$_3$, the relative energetic ordering of the hydride phases, and the bulk moduli of these three phases. We also show that our ChIMES model produces accurate uranium vacancies in α-U and hydrogen vacancies in α-UH$_3$ over a range of defect concentrations. Finally, we have demonstrated that ChIMES model yields accurate kinetic data

for hydrogen interstitial hops in an a-U lattice as well as bulk diffusivity over a broad

temperature range. Therefore, our ChIMES interatomic potential can be used reliably in future

exploration of the U-H system and our effort lays the groundwork for future atomistic modeling

of actinide hydriding.

CHAPTER 5: FUTURE DIRECTIONS

Atomistic simulations and multiscale modeling will continue to be important for understanding hydrogen embrittlement phenomena in uranium and actinides. In this section, I will discuss several scientific directions that could be carried out in this research area.

First, we can extend our DFT study to look at permeation (e.g., the product of solubility and diffusion) of hydrogen within the uranium lattice. This could involve the exploration of hydrogen concentration gradients, where we could examine hydrogen diffusion kinetics from a pure metallic surface to its subsurface as a function of monolayer coverage. Numerous permeation studies of hydrogen have been done in palladium, titanium, and uranium alloys.[30,104–106] We could also utilize microkinetic modeling to investigate whether the penetration of hydrogen within the lattice is limited by diffusion of H atoms from surface to subsurface or whether it is limited by competing reactions, such as the reassociation of atomic hydrogen to form molecular hydrogen or the formation of water. Additional effects of temperature and hydrogen partial pressure could also be explored and verified by experimentally determined results.

Second, under atmospheric conditions, the surface of pure uranium is covered an assortment of oxides, hydroxides, oxycarbides, and water.[107] The strong affinity of oxygen to the metal is widely established and the oxide phases of uranium have been studied in detail.[108–110] However, this surface passive layer (SPL) acts as barrier to hydrogen diffusion, decelerating further corrosion. Hence, we could incorporate UO_2 and U_3O_8 surfaces and interactions with hydrogen data into our ChIMES model in order to explore hydrogen embrittlement under more realistic conditions. We could then calculate the timescale for which hydrogen penetrates the

SPL as well as the hydrogen diffusion coefficient. This could include additional material variability, such as the oxide layer thickness, presence of impurities, and oxide heterogeneity.

Third, grain boundaries (GB) are well-known to be preferential sites for hydrogen nucleation in metals. Hence, our future efforts could also involve simulation of hydriding initiation in the GBs and the formation of the hydride metal within the bulk and surfaces. A comparative study of hydrogen diffusion within the grain boundary and pure bulk are likely important factors in creating a fundamental understanding of this process. We could also look at the effect of the GB angle of incidence and its effect on the hydrogen diffusion coefficient.

All of these ideas could be combined in a single, more complex molecular dynamics simulation, which would include layers of pure uranium with grain boundary structures, partial oxide (U_3O_8) on top, followed by a stoichiometric oxide (UO_2) surface in a hydrogen-containing atmosphere. We could run these molecular dynamics simulations and catalog potential reactions, which would be important inputs for larger scale models, such as kinetic Monte Carlo, to estimate induction times, H_2 permeation, nucleation and growth rates, and potential surface nucleation sites in grain boundaries. We could also verify our calculations of H solubility, diffusion, and permeability with experimental measurements.

APPENDIX A: DENSITY FUNCTIONAL THEORY

Density functional theory (DFT) is a well-established computational technique in most branches of chemistry and materials science for the prediction of physical and chemical properties. DFT has provided an increasingly accurate and predictive methodology in material design, drug discovery, solar cells development, etc. The foundation of DFT is based on two theorems: (i) the external potential $V(\vec{r})$, felt by the electrons is a unique functional of the electron density $n(\vec{r})$ and (ii) the ground state $E(n)$ is minimal for the exact density. Essentially, if we know the electron density, we can obtain the precise energy of the ground state. The total Kohn-Sham energy of system can be written as

$$E_{KS} = T_s[n] + E_H[n] + \int V(\vec{r})\, n(\vec{r}) d\vec{r} + E_{NN} + E_{xc}[n] \qquad \text{Equation 9}$$

where $n(\vec{r}) = \sum_\sigma \sum_{i=1}^{N^\sigma} |\psi_i^\sigma(\vec{r})|^2$ term corresponds to the density of the fictitious system;

$T_s[n] = -\frac{1}{2}\sum_\sigma \sum_{i=1}^{N^\sigma} \langle \psi_i^\sigma | \nabla^2 | \psi_i^\sigma \rangle$ describes the kinetic energy of non-interacting electrons;

$E_H[n] = \frac{1}{2}\int \frac{n(\vec{r}\prime)n(\vec{r})}{|\vec{r}-\vec{r}\prime|} d\vec{r}\prime d\vec{r}$ represents the Coulomb self-interaction energy; E_{NN} is the Coulomb nucleus–nucleus interaction energy; and $E_{xc}[n]$ is called the exchange-correlation energy, which includes all complicated many-body exchange and correlation effects. In theory, DFT is exact for the ground-state energy and electron density, however, in practice the exchange-correlation energy has to be approximated. The physically-motivated definition of the exchange-correlation energy is

$$E_{xc} = \int d\vec{r}\, n(\vec{r})\epsilon_{xc}(n,\vec{r}) \qquad \text{Equation 10}$$

where $\epsilon_{xc}(n,\vec{r})$ is the energy per electron at point $\vec{r}$. Numerous different approaches to DFT calculations have been developed that describe the form and treatment of ϵ_{xc}, such as the local

density approximations (LDA), the generalized-gradient approximations, hybrid functionals, and

other more complex methods.

APPENDIX B: SURFACE SIMULATIONS

The standard procedure used to estimate surface properties from the first-principles electronic structure is the surface slab model — a supercell representing an infinite two-dimensional thin metal film with a facet of interest oriented in Z-direction. Each slab is separated from its neighbors by a certain layer of vacuum thick enough so there is no interaction between adjacent slabs. The width of a slab and the vacuum layer can affect the surface energy and adsorption energy calculations. Therefore, we first investigate the effects of these variables in order to determine the optimal model parameters. Numerous calculations have been performed for vacuum width of 2-20 Å and thicknesses of 4–8 layers for (001) facet, as shown in **Figure A1**. The surface energy for a system comprising N layers and a vacuum width of L are defined by **Equation 1** and convergence is achieved with vacuum width of 20 angstroms and 6-layer thickness. Additional studies for other surfaces are shown in the Supplemental Information section.

(a)
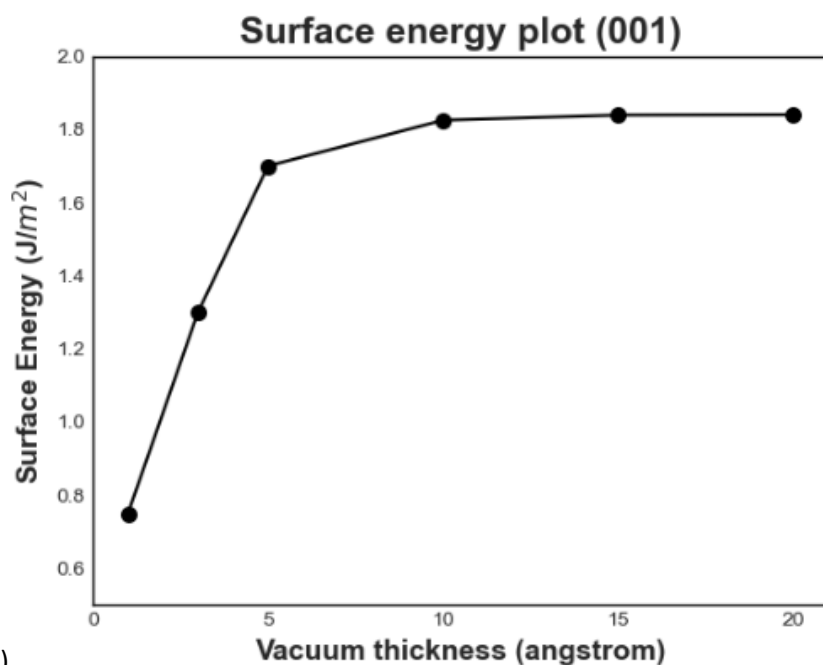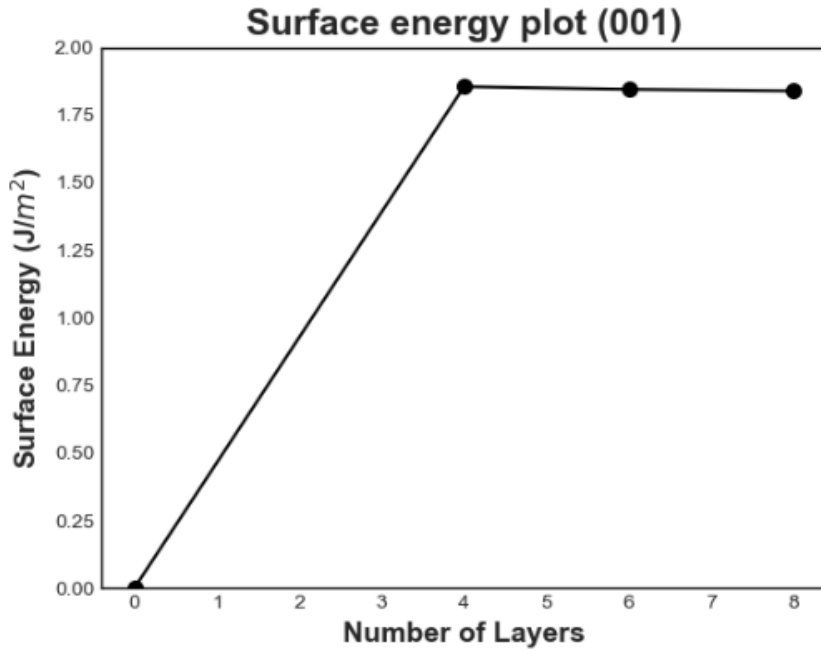
(b)

Figure A1: (a) Vacuum thickness and (b) Number of layers convergence tests.

REFERENCES

1.   Morrell, J. S. & Jackson, M. J. *Uranium processing and properties. Uranium Processing and Properties* vol. 9781461475 (2013).

2.   Lawson, A. C., Olsen, C. E., Richardson, J. W., Mueller, M. H. & Lander, G. H. Structure of β-uranium. *Acta Crystallogr. Sect. B* **44**, 89–96 (1988).

3.   Banos, A., Harker, N. J. & Scott, T. B. A review of uranium corrosion by hydrogen and the formation of uranium hydride. *Corros. Sci.* **136**, 129–147 (2018).

4.   Abraham, B. M. & Flotow, E. The Heats of Formation of Uranium Hydride, Uranium Deuteride and Uranium Tritide at 25°. *J. Am. Chem. Soc.* **77**, 1446–1448 (1955).

5.   Momma, K. & Izumi, F. VESTA 3 for three-dimensional visualization of crystal, volumetric and morphology data. *J. Appl. Crystallogr.* **44**, 1272–1276 (2011).

6.   Le Guyadec, F. *et al.* Pyrophoric behaviour of uranium hydride and uranium powders. *J. Nucl. Mater.* **396**, 294–302 (2010).

7.   Owen, L. W. & Scudamore, R. A. A microscope study of the initiation of the hydrogen-uranium reaction. *Corros. Sci.* **6**, (1966).

8.   Mallett, M. W. Trzeciak, M. J. Hydrogen-uranium relationships. *Trans. ASM* **50**, 981–989 (1958).

9.   Condon, J. B. & Larson, E. A. Kinetics of the uranium-hydrogen system. *J. Chem. Phys.* **855**, 855–865 (1973).

10.   Ji, H. *et al.* Mechanism of surface uranium hydride formation during corrosion of uranium. *npj Mater. Degrad.* **3**, 1–8 (2019).

11.   Smirnova, D. E., Starikov, S. V. & Stegailov, V. V. New interatomic potential for computation of mechanical and thermodynamic properties of uranium in a wide range of pressures and temperatures. *Phys. Met. Metallogr.* **113**, 107–116 (2012).

12.   Smirnova, D. E., Kuksin, A. Y. & Starikov, S. V. Investigation of point defects diffusion in bcc uranium and U-Mo alloys. *J. Nucl. Mater.* **458**, 304–311 (2015).

13.   Nicholson, K. M. & Sholl, D. S. First-principles screening of complex transition metal hydrides for high temperature applications. *Inorg. Chem.* **53**, 11833–11848 (2014).

14.   Taylor, C. D., Lookman, T. & Lillard, R. S. Ab initio calculations of the uranium-hydrogen system: Thermodynamics, hydrogen saturation of α-U and phase-transformation to UH3. *Acta Mater.* **58**, 1045–1055 (2010).

15.   Wolverton, C., Ozoliņš, V. & Asta, M. Hydrogen in aluminum: First-principles calculations of structure and thermodynamics. *Phys. Rev. B - Condens. Matter Mater. Phys.* **69**, 1–16 (2004).

16.   Jiang, D. E. & Carter, E. A. Diffusion of interstitial hydrogen into and through bcc Fe from first principles. *Phys. Rev. B - Condens. Matter Mater. Phys.* **70**, 1–9 (2004).

17.   Domain, C., Besson, R. & Legris, A. Atomic-scale Ab-initio study of the Zr-H system: I. Bulk properties. *Acta Mater.* **50**, 3513–3526 (2002).

18.   Sundell, P. G. & Wahnström, G. Quantum motion of hydrogen on Cu(001) using first-principles calculations. *Phys. Rev. B - Condens. Matter Mater. Phys.* **70**, 1–4 (2004).

19.   Xu, Q. & Van Der Ven, A. First-principles investigation of metal-hydride phase stability: The Ti-H system. *Phys. Rev. B - Condens. Matter Mater. Phys.* **76**, 1–12 (2007).

20. Das, S. S., Kopnov, G. & Gerber, A. Kinetics of the lattice response to hydrogen absorption in Thin Pd and CoPd films. *Molecules* **25**, 1–10 (2020).

21. Mamatkulov, M. & Zhdanov, V. P. Partial or complete suppression of hysteresis in hydride formation in binary alloys of Pd with other metals. *J. Alloys Compd.* **885**, 160956 (2021).

22. Goldman, N. *et al.* Semi-Automated Creation of Density Functional Tight Binding Models through Leveraging Chebyshev Polynomial-Based Force Fields. *J. Chem. Theory Comput.* **17**, 4435–4448 (2021).

23. Mullen, R. G. & Goldman, N. Quantum accurate prediction of plutonium−plutonium dihydride phase equilibrium using a lattice gas model. *J. Phys. Chem. C* **124**, 20881–20888 (2020).

24. Mullen, R. G. & Goldman, N. A first-principles study of hydrogen surface coverage on δ - Pu (100), (111), and (110) surfaces. *J. Chem. Phys.* **155**, 1–25 (2021).

25. Huang, S., Zeng, X. L., Zhao, F. Q. & Ju, X. H. Density functional study of H2 molecule and H atom adsorption on α-U(001) surface. *Surf. Interface Anal.* **48**, 328–333 (2016).

26. Huang, S. Q. & Ju, X. H. First-principles study of properties of alpha uranium crystal and seven alpha uranium surfaces. *J. Chem.* **2017**, (2017).

27. Nie, J. L., Xiao, H. Y., Zu, X. T. & Gao, F. Hydrogen adsorption, dissociation and diffusion on the α-U(001) surface. *J. Phys. Condens. Matter* **20**, (2008).

28. Taylor, C. D. Evaluation of first-principles techniques for obtaining materials parameters of α -uranium and the (001) α -uranium surface. *Phys. Rev. B - Condens. Matter Mater.*

Phys. **77**, 1–9 (2008).

29.   Taylor, C. D. & Scott Lillard, R. Ab-initio calculations of the hydrogen-uranium system: Surface phenomena, absorption, transport and trapping. *Acta Mater.* **57**, 4707–4715 (2009).

30.   Chapman, J. *et al.* Hydrogen in disordered titania: connecting local chemistry, structure, and stoichiometry through accelerated exploration. *J. Mater. Chem. A* (2023) doi:10.1039/d2ta07075h.

31.   Brooks, B. R. *et al.* CHARMM: A program for macromolecular energy, minimization, and dynamics calculations. *J. Comput. Chem.* **4**, 187–217 (1983).

32.   Rappe, A. K., Casewit, C. J., Colwell, K. S. & Goddard III, W. A. UFF, a Full Periodic Table Force Field for Molecular Mechanics and Molecular Dynamics Simulations. *J. Am. Chem. SOC* **114**, 10024–10035 (1992).

33.   Cornell, W., Cieplak, P., Bayly, C. & Gould, I. A Second Generation Force Field for the Simulation of Proteins, Nucleic Acids, and Organic Molecules. *J. Am. Chem. SOC* **117**, 5179–5197 (1995).

34.   Senftle, T. P., Janik, M. J. & Van Duin, A. C. T. A ReaxFF investigation of hydride formation in palladium nanoclusters via Monte Carlo and molecular dynamics simulations. *J. Phys. Chem. C* **118**, 4967–4981 (2014).

35.   Liang, T. *et al.* Reactive potentials for advanced atomistic simulations. *Annu. Rev. Mater. Res.* **43**, 109–129 (2013).

36.   Bartók, A. P., Kermode, J., Bernstein, N. & Csányi, G. Machine Learning a General-

Purpose Interatomic Potential for Silicon. *Phys. Rev. X* **8**, 41048 (2018).

37.   Wang, H., Zhang, L., Han, J. & E, W. DeePMD-kit: A deep learning package for many-body potential energy representation and molecular dynamics. *Comput. Phys. Commun.* **228**, 178–184 (2018).

38.   Lu, D. *et al.* DP Train, then DP Compress: Model Compression in Deep Potential Molecular Dynamics. 1–9 (2021).

39.   Tamura, R., Lin, J. & Miyazaki, T. Machine learning forces trained by Gaussian process in liquid states: Transferability to temperature and pressure. *J. Phys. Soc. Japan* **88**, 1–21 (2019).

40.   Panosetti, C., Engelmann, A., Nemec, L., Reuter, K. & Margraf, J. T. Learning to Use the Force: Fitting Repulsive Potentials in Density-Functional Tight-Binding with Gaussian Process Regression. *J. Chem. Theory Comput.* **16**, 2181–2191 (2020).

41.   Lindsey, R. K., Fried, L. E. & Goldman, N. ChIMES: A Force Matched Potential with Explicit Three-Body Interactions for Molten Carbon. *J. Chem. Theory Comput.* **13**, 6222–6229 (2017).

42.   Lindsey, R. K., Fried, L. E., Goldman, N. & Bastea, S. Active learning for robust, high-complexity reactive atomistic simulations. *J. Chem. Phys.* **153**, (2020).

43.   Pham, C. H., Lindsey, R. K., Fried, L. E. & Goldman, N. High-Accuracy Semiempirical Quantum Models Based on a Minimal Training Set. *J. Phys. Chem. Lett.* **13**, 2934–2942 (2022).

44.   Koziol, L., Fried, L. E. & Goldman, N. Using force matching to determine reactive force

fields for water under extreme thermodynamic conditions. *J. Chem. Theory Comput.* **13**, 135–146 (2017).

45.   Lindsey, R. K., Fried, L. E. & Goldman, N. Application of the ChIMES Force Field to Nonreactive Molecular Systems: Water at Ambient Conditions. *J. Chem. Theory Comput.* **15**, 436–447 (2019).

46.   Armstrong, M. R. *et al.* Ultrafast shock synthesis of nanocarbon from a liquid precursor. *Nat. Commun.* **11**, 1–7 (2020).

47.   Lindsey, R. K., Goldman, N., Fried, L. E. & Bastea, S. Many-body reactive force field development for carbon condensation in C/O systems under extreme conditions. *J. Chem. Phys.* **153**, (2020).

48.   Pham, C. H., Lindsey, R. K., Fried, L. E. & Goldman, N. Calculation of the detonation state of HN3with quantum accuracy. *J. Chem. Phys.* **153**, (2020).

49.   Goldman, N., Fried, L. E., Lindsey, R. K., Pham, C. H. & Dettori, R. Enhancing the Accuracy of Density Functional Tight Binding Models Through ChIMES Many-body Interaction Potentials. *J. Chem. Phys.* **144112**, 1–17 (2023).

50.   Kresse, G. & Furthmüller, J. Efficient iterative schemes for ab initio total-energy calculations using a plane-wave basis set. *Phys. Rev. B - Condens. Matter Mater. Phys.* **54**, 11169–11186 (1996).

51.   Blöchl, P. E. Projector augmented-wave method. *Phys. Rev. B* **50**, 17953–17979 (1994).

52.   Methfessel, M. & Paxton, A. T. High-precision sampling for Brillouin-zone integration in metals. *Phys. Rev. B* **40**, 3616–3621 (1989).

53. Monkhorst, H. J. & Pack, J. D. Special points for Brillouin-zone integrations. *Phys. Rev. B* **13**, 5188–5192 (1976).

54. Taylor, C. D. Periodic trends governing the interactions between impurity atoms [H-Ar] and α-U. *Philos. Mag.* **89**, 465–487 (2009).

55. Fiorentini, V. & Methfessel, M. Extracting convergent surface energies from slab calculations. *J. Phys. Condens. Matter* **8**, 6525–6529 (1996).

56. Su, Q. *et al.* First-principles study on the interaction of nitrogen atom with α-uranium: From surface adsorption to bulk diffusion. *J. Appl. Phys.* **115**, (2014).

57. Barrett, C. S., Mueller, M. H. & Hitterman, R. L. Crystal structure variations in alpha uranium at low temperatures. *Phys. Rev.* **129**, 625–629 (1963).

58. Söderlind, P. Ambient pressure phase diagram of plutonium: A unified theory for α-Pu and δ-Pu. *Europhys. Lett.* **55**, 525–531 (2001).

59. Beridze, G. & Kowalski, P. M. Benchmarking the DFT+ U method for thermochemical calculations of uranium molecular compounds and solids. *J. Phys. Chem. A* **118**, 11797–11810 (2014).

60. Su, Q. *et al.* First-principles study of nitrogen adsorption and dissociation on α-uranium (001) surface. *RSC Adv.* **4**, 57308–57321 (2014).

61. Goldman, N. & Morales, M. A. A First-Principles Study of Hydrogen Diffusivity and Dissociation on δ-Pu (100) and (111) Surfaces. *J. Phys. Chem. C* **121**, 17950–17957 (2017).

62. Dettori, R. & Goldman, N. First-principles surface characterization and water adsorption

of Fe 3 P schreibersite. *ChemRxiv* 1–26 (2021).

63. Patra, A., Bates, J. E., Sun, J. & Perdew, J. P. Properties of real metallic surfaces: Effects of density functional semilocality and van der Waals nonlocality. *Proc. Natl. Acad. Sci. U. S. A.* **114**, E9188–E9196 (2017).

64. Nie, J. L., Ao, L., Zu, X. T., Huang, H. & Liu, K. Z. The interaction of oxygen with the α-U(001) surface: An ab initio study. *Phys. Scr.* **89**, 1–5 (2014).

65. Stojić, N., Davenport, W., Komelj, M. & Glimm, J. Surface magnetic moment in α-uranium by density-functional theory. *Phys. Rev. B - Condens. Matter Mater. Phys.* **68**, 1–5 (2003).

66. Dholabhai, P. P. & Ray, A. K. A density functional study of carbon monoxide adsorption on (1 0 0) surface of γ-uranium. *J. Alloys Compd.* **444**–**445**, 356–362 (2007).

67. Morrison, D. R. & Ray, A. K. Atomic H interaction with the γ-U (100) surface. *Phys. Status Solidi Basic Res.* **250**, 2221–2231 (2013).

68. Lischka, M. Adsorption of simple molecules on structured surfaces. 3–21 (2003).

69. Ghosh, P., Pushpa, R., De Gironcoli, S. & Narasimhan, S. Effective coordination number: A simple indicator of activation energies for NO dissociation on Rh(100) surfaces. *Phys. Rev. B - Condens. Matter Mater. Phys.* **80**, 1–4 (2009).

70. Kumar, N. & Ghosh, P. Structure and stability of clean and adsorbate covered intermetallic PdGa surfaces: A first principles study. *Surf. Sci.* **644**, 69–79 (2016).

71. Larcht'e, F. C. & Cahn, J. l. The effect of self-stress on diffusion in solids. *Acta Metall.* **30**, 1835–1845 (1982).

72. Dietze, E. M. & Grönbeck, H. Structure-Dependent Strain Effects. *ChemPhysChem* **21**, 2407–2410 (2020).

73. Grönbeck, H. & Zhdanov, V. P. Effect of lattice strain on hydrogen diffusion in Pd: A density functional theory study. *Phys. Rev. B - Condens. Matter Mater. Phys.* **84**, 1–4 (2011).

74. Kesharwani, M. K., Brauer, B. & Martin, J. M. L. Frequency and zero-point vibrational energy scale factors for double-hybrid density functionals (and other selected methods): Can anharmonic force fields be avoided? *J. Phys. Chem. A* **119**, 1701–1714 (2015).

75. Chaudhary, N., Hensley, A., Collinge, G., Wang, Y. & McEwen, J. S. Coverage-Dependent Adsorption of Phenol on Pt(111) from First Principles. *J. Phys. Chem. C* (2019) doi:10.1021/acs.jpcc.9b07517.

76. Tang, H., Van Der Ven, A. & Trout, B. L. Lateral interactions between oxygen atoms adsorbed on platinum (111) by first principles. *Mol. Phys.* **102**, 273–279 (2004).

77. Caruana, R. & Freitag, D. Greedy Attribute Selection. *Mach. Learn. Proc. 1994* 28–36 (1994) doi:10.1016/b978-1-55860-335-6.50012-x.

78. Lym, J., Wittreich, G. R. & Vlachos, D. G. A Python Multiscale Thermochemistry Toolbox (pMuTT) for thermochemical and kinetic parameter estimation. *Comput. Phys. Commun.* **247**, 106864 (2020).

79. Kresse, G. & Hafner, J. Ab initio molecular dynamics for liquid metals. *Phys. Rev. B* **47**, 558–561 (1993).

80. Kresse, G. & Hafner, J. Ab initio molecular-dynamics simulation of the liquid-

metalamorphous- semiconductor transition in germanium. *Phys. Rev. B* **49**, 14251–14269 (1994).

81. Kresse, G. & Furthmüller, J. Efficiency of ab-initio total energy calculations for metals and semiconductors using a plane-wave basis set. *Comput. Mater. Sci.* **6**, 15–50 (1996).

82. Joubert, D. From ultrasoft pseudopotentials to the projector augmented-wave method. *Phys. Rev. B - Condens. Matter Mater. Phys.* **59**, 1758–1775 (1999).

83. Perdew, J. P., Burke, K. & Ernzerhof, M. Generalized gradient approximation made simple. *Phys. Rev. Lett.* **77**, 3865–3868 (1996).

84. Nosé, S. A unified formulation of the constant temperature molecular dynamics methods. *J. Chem. Phys.* **81**, 511–519 (1984).

85. Hoover, W. G. Canonical dynamics: Equilibrium phase-space distributions. *Phys. Rev. A* **31**, 1695–1697 (1985).

86. Martyna, G. J., Klein, M. L. & Tuckerman, M. Nosé-Hoover chains: The canonical ensemble via continuous dynamics. *J. Chem. Phys.* **97**, 2635–2643 (1992).

87. Lindsey, R. K., Huy Pham, C., Goldman, N., Bastea, S. & Fried, L. E. Machine-Learning a Solution for Reactive Atomistic Simulations of Energetic Materials. *Propellants, Explos. Pyrotech.* (2022) doi:10.1002/prep.202200001.

88. Drautz, R. Atomic cluster expansion for accurate and transferable interatomic potentials. *Phys. Rev. B* **99**, 1–15 (2019).

89. Bochkarev, A., Lysogorskiy, Y., Ortner, C., Csányi, G. & Drautz, R. Multilayer atomic cluster expansion for semilocal interactions. *Phys. Rev. Res.* **4**, (2022).

90. Thompson, A. P., Swiler, L. P., Trott, C. R., Foiles, S. M. & Tucker, G. J. Spectral neighbor analysis method for automated generation of quantum-accurate interatomic potentials. *J. Comput. Phys.* **285**, 316–330 (2015).

91. Khorshidi, A. & Peterson, A. A. Amp: A modular approach to machine learning in atomistic simulations. *Comput. Phys. Commun.* **207**, 310–324 (2016).

92. Ercolesi, F. & Adams, J. B. Interatomic potentials from first-principles calculations: The force-matching method. *Eur. Lett.* **26**, 583–588 (1994).

93. Fan, Z. *et al.* Neuroevolution machine learning potentials: Combining high accuracy and low cost in atomistic simulations and application to heat transport. *Phys. Rev. B* **104**, 1–18 (2021).

94. Efron, B., Hastie, T., Johnstone, I. & Tibshirani, R. LEAST ANGLE REGRESSION. *Ann. Stat.* **32**, 407–499 (2004).

95. Zhang, H. J., Li, S. N., Zheng, J. J., Li, W. D. & Wang, B. T. Effects of pressure on structural, electronic, and mechanical properties of α, β, and γ uranium. *Chinese Phys. B* **26**, (2017).

96. Grunzweig-Genossar, J., Kuznietz, M. & Meerovici, B. Nuclear Magnetic Resonance in Uranium Hydride and Deuteride. *Phys. Rev. B* **1**, (1970).

97. Akella, J., Weir, S., Wills, J. M. & Söderlind, P. Structural stability in uranium. *J. Phys. Condens. Matter* **9**, (1997).

98. Birch, F. Finite elastic strain of cubic crystals. *Phys. Rev.* **71**, 809–824 (1947).

99. Huang, G. Y. & Wirth, B. D. First-principles study of bubble nucleation and growth

behaviors in α U-Zr. *J. Phys. Condens. Matter* **24**, (2012).

100. Beeler, B. *et al.* First principles calculations for defects in U. *J. Phys. Condens. Matter* **22**, 3–10 (2010).

101. Matter, H., Winter, J. & Triftshauser, W. INVESTIGATION OF VACANCY FORMATION AND PHASE TRANSFORMATIONS IN URANIUM BY POSITRON ANNIHILATION. *J. Nucl. Mater.* **88**, 273–278 (1980).

102. Holby, E. F. Crystallographic orientation effects of hydrogen diffusion in α-uranium from DFT: Interpreting variations in experimental data. *J. Nucl. Mater.* **513**, 293–296 (2019).

103. Henkelman, G., Uberuaga, B. P. & Jónsson, H. Climbing image nudged elastic band method for finding saddle points and minimum energy paths. *J. Chem. Phys.* **113**, 9901–9904 (2000).

104. Kumar, N., Chattaraj, D., Ghosh, P. & Majumder, C. Microscopic Insights into Hydrogen Permeation Through a Model PdCu Membrane from First-Principles Investigations. *J. Phys. Chem. C* **122**, 12920–12933 (2018).

105. Sunwoo, A. & Goto, D. Effects of processing on microstructure and properties of α-uranium formed parts. *Scr. Mater.* **47**, 261–266 (2002).

106. Roa, F., Block, M. J. & Way, J. D. The influence of alloy composition on the H2 flux of composite Pd-Cu membranes. *Desalination* **147**, 411–416 (2002).

107. Brill, M., Bloch, J. & Mintz, M. H. Experimental verification of the formal nucleation and growth rate equations - Initial UH3 development on uranium surface. *J. Alloys Compd.* **266**, 180–185 (1998).

108. Allen, G. C. & Tucker, P. M. Surface oxidation of uranium metal as studied by X-ray photoelectron spectroscopy. *J. Chem. Soc. Dalt. Trans.* 470–474 (1973) doi:10.1039/DT9730000470.

109. Allen, G. C. *et al.* X-Ray photoelectron spectroscopy of some uranium oxide phases. *J. Chem. Soc. Dalt. Trans.* 1296–1301 (1974) doi:10.1039/DT9740001296.

110. Allen, G. C., Tucker, P. M. & Lewis, R. A. X-ray photoelectron spectroscopy study of the initial oxidation of uranium metal in oxygen + water-vapour mixtures. *J. Chem. Soc. Faraday Trans. 2 Mol. Chem. Phys.* **80**, 991–1000 (1984).
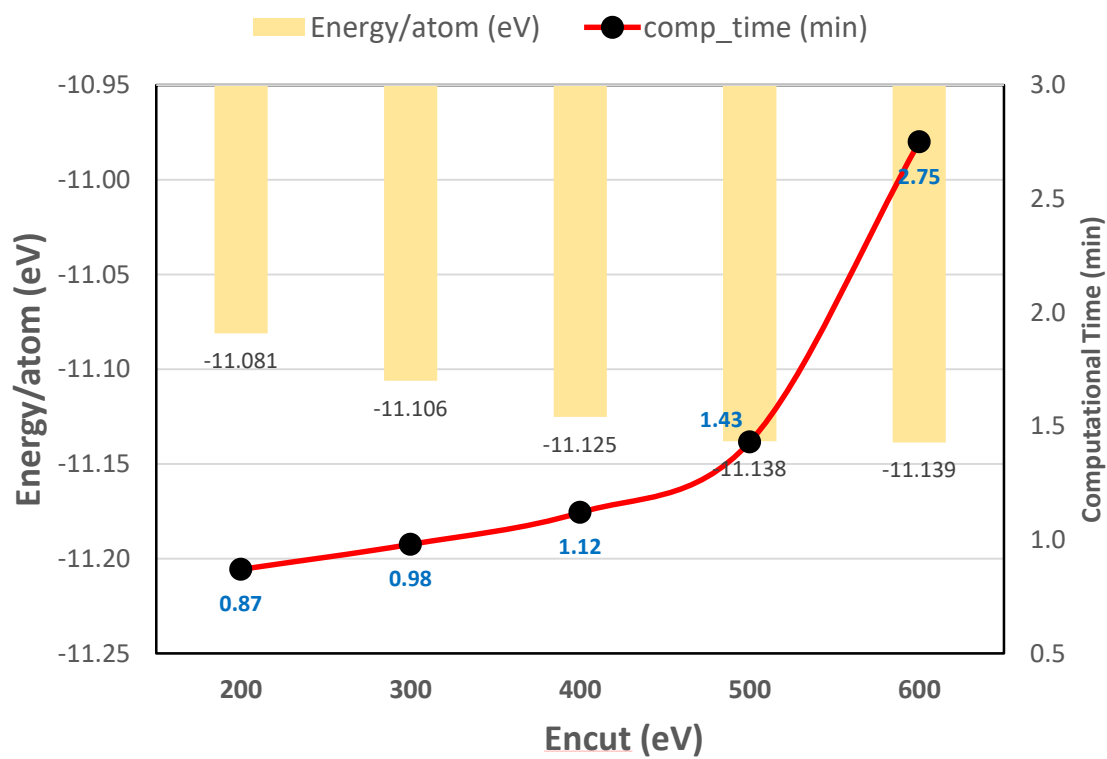
Figure S1: Encut convergence test.
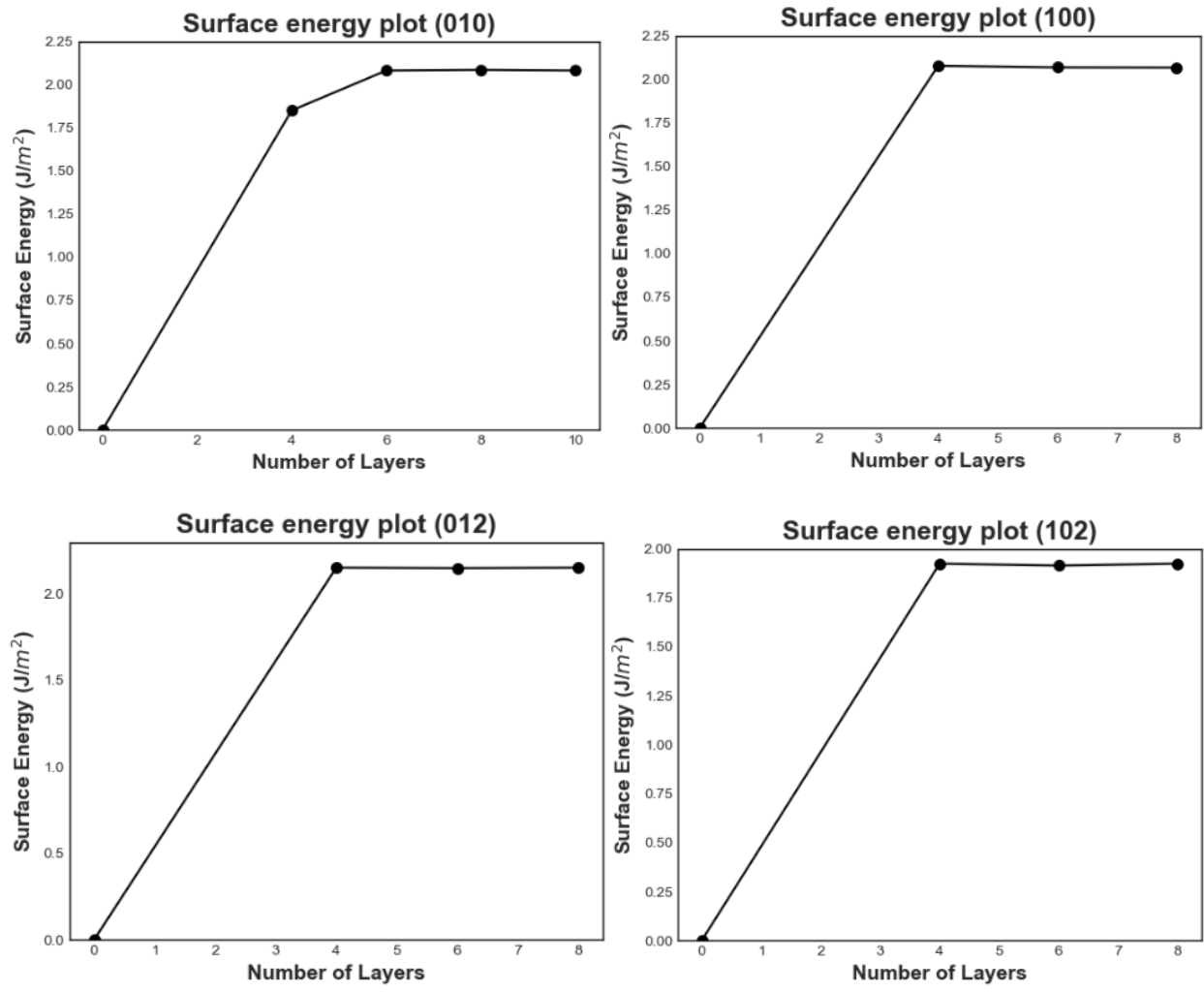
Figure S2: DFT estimated α-U surface energies.
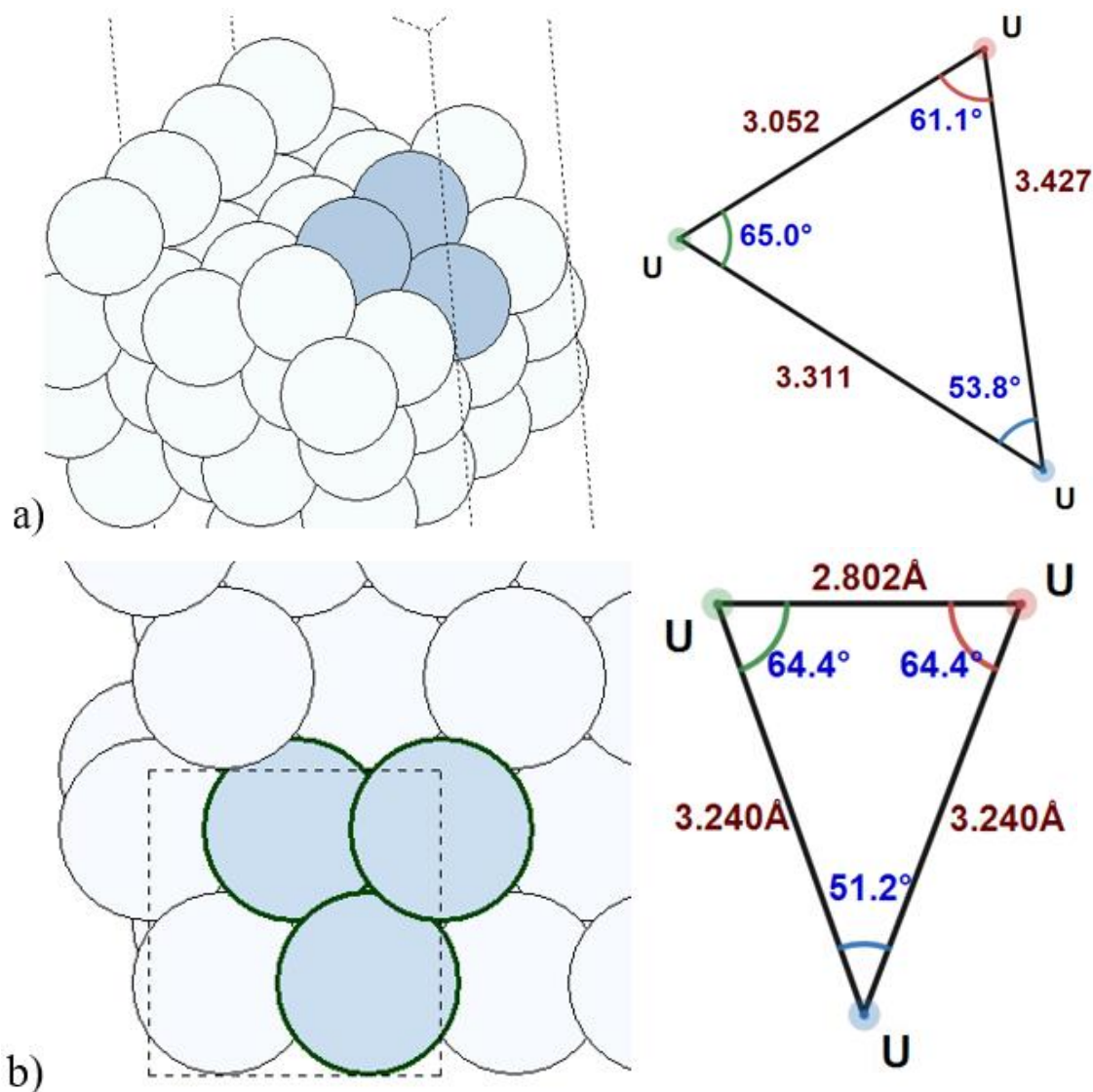
Figure S3: Geometric comparison of terrace and kinked sites. (a) stepped hollow site of (012) facet, (b) terrace hollow site of (001) surface. (012) facet has 3.052, 3.311, and 3.196 Å U-U bond distances and 53.8°, 61.1°, and 65.0° angles that encompass the most energetically favorable hollow site, compared to values of 2.802 Å and 3.240 Å for bonds and 51.2°, 64.4°, and 64.4° for angles from the (001) surface.
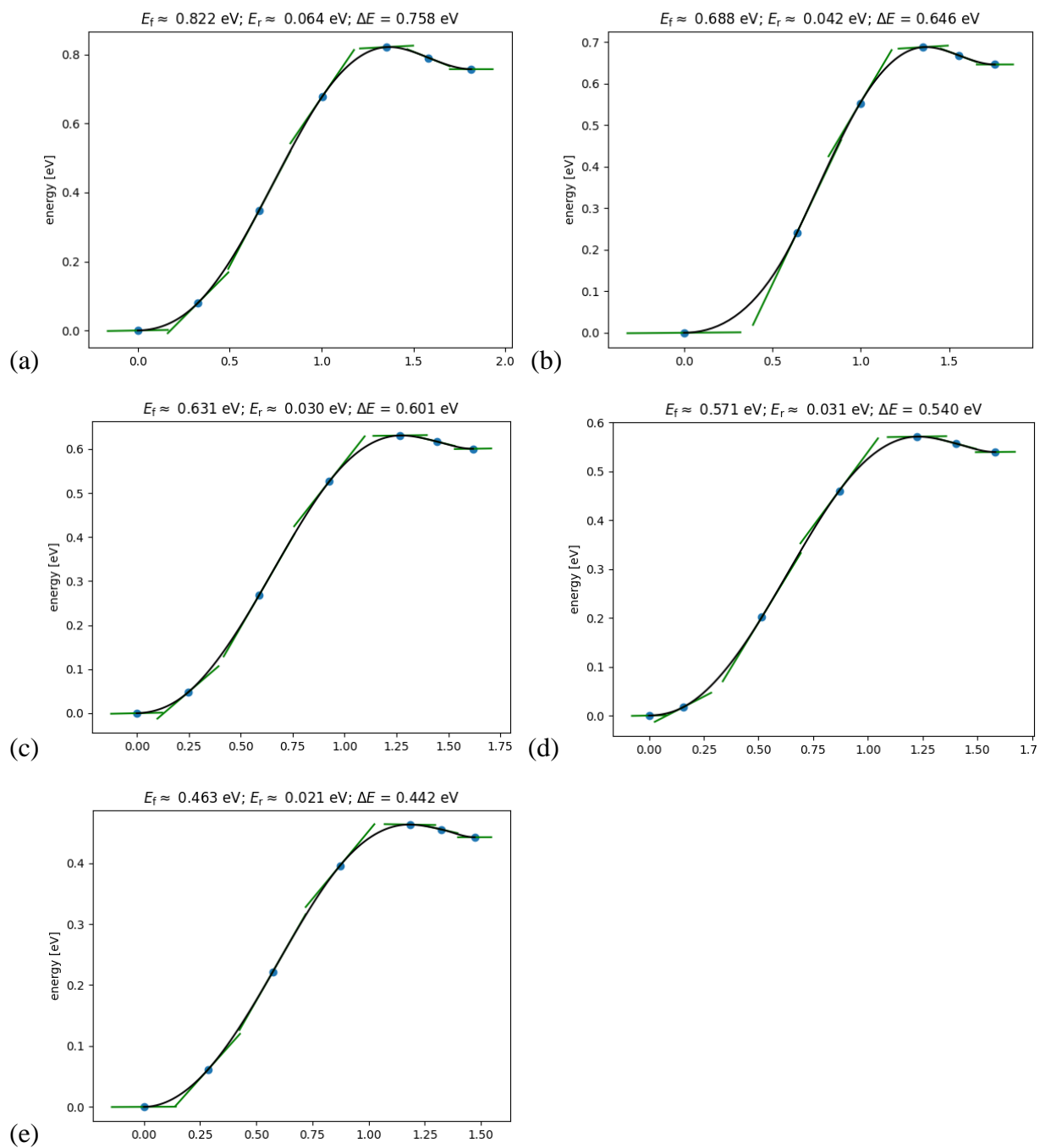
Figure S4: Sample NEB plots for (001) facet. (a) 0%, (b) 1%, (c) 2%, (d) 3%, and (e) 4% tensile load.

Table S1: Interlayer and U-U bond distances comparison as a function of tensile strain for common terrace surfaces.

Surface	Expansion	Interlayer distance (Å)	% change due to exp. (rel. to perf)	% change due relax. (rel. to perf.)	% total change (rel. to perf. lattice)	Bond distance (Å)	% change (rel. to perf. lattice)
001	0%	2.353	0.00%	0.00%	0.00%	2.802	0.00%
	1%	2.338	1.00%	-1.64%	-0.64%	2.83	1.00%
	2%	2.324	2.00%	-3.23%	-1.23%	2.858	2.00%
	3%	2.311	3.00%	-4.78%	-1.78%	2.886	3.00%
	4%	2.297	4.00%	-6.38%	-2.38%	2.914	4.00%
010	0%	2.903	0.00%	0.00%	0.00%	2.802	0.00%
	1%	2.887	1.00%	-1.55%	-0.55%	2.83	1.00%
	2%	2.869	2.00%	-3.17%	-1.17%	2.858	2.00%
	3%	2.851	3.00%	-4.79%	-1.79%	2.886	3.00%
	4%	2.833	4.00%	-6.41%	-2.41%	2.914	4.00%
100	0%	2.624	0.00%	0.00%	0.00%	2.732	0.00%
	1%	2.608	1.00%	-1.61%	-0.61%	2.751	0.70%
	2%	2.596	2.00%	-3.07%	-1.07%	2.767	1.28%
	3%	2.583	3.00%	-4.56%	-1.56%	2.786	1.98%
	4%	2.572	4.00%	-5.98%	-1.98%	2.807	2.75%

Table S2: Surface vs subsurface adsorption energy comparison as a function of tensile strain. E_{ads} represents the lowest adsorption energy for H atom on surface; E_{ss} denotes the lowest absorption energy to insert H atom inside the first subsurface layer for a given surface; ΔE indicates the energy difference between surface adsorption and subsurface absorption; E_{TS} represents the energy of the transition state.

Surface	Tensile strain	Surf site	E_{ads} (eV)	E_{ads} (eV) w/ZPE	Subsurf site	E_{ss} (eV)	E_{ss} (eV) w/ZPE	ΔE (eV)	E_{TS} (eV)	E_{TS} (eV) w/ZPE
001	0%	3-fold	-0.57	-0.41	Tet	0.16	0.40	-0.73	0.82	0.86
	1%	3-fold	-0.62	-0.46	Tet	0.03	0.26	-0.65	0.69	0.73
	2%	3-fold	-0.67	-0.52	Tet	-0.14	0.09	-0.53	0.63	0.66
	3%	3-fold	-0.67	-0.52	Tet	-0.32	-0.10	-0.35	0.57	0.60
	4%	3-fold	-0.69	-0.53	Tet	-0.51	-0.30	-0.18	0.46	0.48
010	0%	4-fold	-0.39	-0.25	Sqpy	0.22	0.43	-0.61	0.78	0.82
	1%	4-fold	-0.46	-0.32	Sqpy	0.11	0.32	-0.57	0.67	0.71
	2%	4-fold	-0.55	-0.41	Sqpy	-0.06	0.15	-0.49	0.55	0.59
	3%	4-fold	-0.65	-0.52	Sqpy	-0.19	0.01	-0.46	0.49	0.52
	4%	4-fold	-0.74	-0.61	Sqpy	-0.38	-0.20	-0.36	0.42	0.45
100	0%	3-fold	-0.58	-0.42	Sqpy	0.12	0.33	-0.70	0.82	0.83
	1%	3-fold	-0.61	-0.44	Sqpy	0.08	0.29	-0.69	0.78	0.78
	2%	3-fold	-0.65	-0.49	Sqpy	-0.01	0.19	-0.64	0.74	0.73
	3%	3-fold	-0.70	-0.54	Sqpy	-0.09	0.11	-0.61	0.64	0.66
	4%	3-fold	-0.76	-0.60	Sqpy	-0.26	-0.07	-0.50	0.55	0.53
012	0%	3-fold	-0.71	-0.54	Tet	0.16	0.39	-0.87	1.48	1.49
	1%	3-fold	-0.73	-0.56	Tet	0.10	0.33	-0.83	1.40	1.42
	2%	3-fold	-0.74	-0.57	Tet	-0.02	0.20	-0.72	1.33	1.33
	3%	3-fold	-0.77	-0.60	Tet	-0.10	0.12	-0.67	1.30	1.30
	4%	3-fold	-0.79	-0.62	Tet	-0.20	-0.01	-0.59	1.24	1.25
102	0%	3-fold	-0.66	-0.52	Tet	0.10	0.33	-0.76	0.91	0.95
	1%	3-fold	-0.67	-0.53	Tet	0.03	0.25	-0.70	0.81	0.85
	2%	3-fold	-0.67	-0.53	Tet	-0.05	0.14	-0.62	0.79	0.83
	3%	3-fold	-0.68	-0.54	Tet	-0.09	0.10	-0.59	0.73	0.74
	4%	3-fold	-0.69	-0.55	Tet	-0.13	0.05	-0.56	0.65	0.66

Table S3: The adsorption energy to add additional hydrogen atom on α-U surface or in the first subsurface layer as a function of coverage. $E_{add\_subsurf}$ denotes the energy required to add a hydrogen atom to the subsurface layer; E_{add_surf} (eV) represents the energy required to add a hydrogen on the top of the surface.

Surface	Coverage (ML)	E_{add_surf} (eV)	$E_{add\_subsurf}$ (eV)
(010)	0	-0.39	0.22
	1/8	-0.40	0.24
	2/8	-0.26	0.25
	3/8	-0.12	0.25
	4/8	-0.03	0.22
	5/8	0.06	0.32
(100)	0	-0.58	0.12
	1/8	-0.60	0.20
	2/8	-0.37	0.19
	3/8	-0.32	0.17
	4/8	-0.28	0.18
	5/8	-0.11	0.25
	6/8	0.26	0.28
(012)	0	-0.71	0.16
	1/18	-0.67	0.17
	2/18	-0.63	0.18
	3/18	-0.53	0.19
	4/18	-0.43	0.17
	5/18	-0.41	0.10
	6/18	-0.40	0.06
	7/18	-0.38	0.05
	8/18	-0.38	0.11
	9/18	-0.33	0.12
(102)	0	-0.66	0.10
	1/16	-0.66	-0.07
	2/16	-0.57	-0.09
	3/16	-0.54	-0.09
	4/16	-0.56	-0.14
	5/16	-0.41	-0.15
	6/16	-0.40	-0.10
	7/16	-0.35	-0.08
	8/16	-0.34	0.21
	9/16	-0.26	0.27

Table S4: Exploring the effect of applied spin polarization and the Hubbard U correction on the estimation of surface properties.

Surface	PBE (ispin=1)	PBE (ispin=2)		PBE+U (ispin=1)
	SE (J/m²)	SE (J/m²)	Mag mom/surf atom	SE (J/m²)
(001)	1.83	1.80	0.89	1.78
(010)	2.06	1.93	0.66	2.35
(100)	2.08	1.99	1.28	2.17
(012)	2.15	2.05	2.23	2.07
(102)	1.92	2.03	1.94	2.02

In addition to exploring different functional methods, we have also investigated the effect of applied spin polarization and the Hubbard U correction on the estimation of surface properties. We notice that spin polarization has very minor effect on the surface energies by lowering the estimated energies by 0.03-0.13 J/m², depending on the facet type. This could be attributed to very small surface magnetization for low index facets and somewhat significant, but still relatively small for the kinked surfaces. However, we do notice that the ordering of the surface energies changes with applied spin polarization. Also, applied spin polarization in calculation of adsorption only slightly lowers energies, +0.08eV for (012) and +0.07eV for (102) facets.

Surface energies undergo similar changes with applied PBE+U method. We also noticed the ordering changes.

Table S5: Validation Results for polynomial structure a) RMS, b) Validation tests, and c) Validation test (including 4B interactions)

Polynomial Type	rms H (ev/Å)	rms U (ev/Å)	rms E (ev/atom)	rms P (GPa)	Polynomial Type	rms H (ev/Å)	rms U (ev/Å)	rms E (ev/atom)	rms P (GPa)
2 2 0	2.024	20.521	3.660	26.16	10 8 0	0.31	0.871	0.251	1.481
2 4 0	0.843	10.984	3.412	50.497	10 10 0	0.239	0.539	0.263	0.867
2 6 0	0.634	2.778	1.633	17.645	10 12 0	0.253	0.506	0.346	1.273
2 8 0	0.569	2.096	1.670	17.427	12 2 0	0.713	16.029	1.246	4.287
2 10 0	0.625	1.797	1.579	16.331	12 4 0	0.994	8.093	2.019	14.789
2 12 0	0.488	1.577	1.446	14.988	12 6 0	0.488	1.834	0.371	2.662
2 14 0	0.441	1.462	1.443	14.328	12 8 0	0.268	0.623	0.261	1.137
4 2 0	1.646	19.722	9.886	114.472	12 10 0	0.223	0.426	0.302	0.927
4 4 0	0.909	9.77	6.729	53.609	12 12 0	0.202	0.359	0.385	0.729
4 6 0	0.609	2.681	0.961	10.381	14 2 0	0.709	16.026	1.223	4.095
4 8 0	0.538	1.974	1.216	12.211	14 4 0	0.991	8.092	2.018	14.774
4 10 0	0.589	1.654	1.022	10.186	14 6 0	0.497	1.818	0.403	2.921
4 12 0	0.45	1.404	0.797	7.843	14 8 0	0.266	0.573	0.247	0.769
4 14 0	0.399	1.194	0.771	6.641	14 10 0	0.22	0.403	0.301	0.727
6 2 0	1.157	18.839	6.783	75.467	14 12 0	0.202	0.368	0.381	0.705
6 4 0	0.983	9.339	5.912	44.722	16 2 0	0.701	16.025	1.148	3.808
6 6 0	0.546	2.169	0.224	2.531	16 4 0	0.987	8.062	2.039	14.543
6 8 0	0.431	1.544	0.667	6.48	16 6 0	0.497	1.815	0.406	2.97
6 10 0	0.454	1.153	0.487	4.56	16 8 0	0.266	0.58	0.243	0.771
6 12 0	0.335	0.923	0.355	2.924	16 8 1	0.266	0.58	0.243	0.771
6 14 0	0.287	0.713	0.495	2.094	16 8 2	0.263	0.56	0.238	0.738
8 2 0	0.748	16.581	2.403	22.207	16 8 3	0.254	0.532	0.216	0.789
8 4 0	0.999	8.441	3.365	23.168	16 8 4	0.239	0.512	0.191	0.877
8 6 0	0.489	1.971	0.283	1.962	16 10 0	0.223	0.412	0.296	0.754
8 8 0	0.338	1.037	0.314	3.165	16 12 0	0.201	0.356	0.400	0.711
8 10 0	0.265	0.635	0.243	1.691	18 2 0	0.697	16.024	1.127	3.638
8 12 0	0.233	0.474	0.276	1.182	18 4 0	0.997	8.048	2.034	14.614
8 14 0	0.203	0.369	0.481	1	18 6 0	0.501	1.806	0.411	3.007
10 2 0	0.715	16.129	1.186	5.655	18 8 0	0.266	0.571	0.248	0.73
10 4 0	0.985	8.153	2.222	15.027	18 10 0	0.219	0.401	0.304	0.709
10 6 0	0.475	1.938	0.323	2.371	18 12 0	0.197	0.342	0.421	0.696

(a)

98

(b)

Poly Type	aU_lata	aU_latb	aU_latc	aU_V	aUH3_lata	aUH3_V	DEF Vac_U	DEF Int1H
2 2 0	2.542 (-9.68%)	5.3 (-9.67%)	4.448 (-9.68%)	14.98 (-26.29%)	3.749 (-9.01%)	26.34 (-24.67%)	-178.505 (10128.	-157.872 (59007.46%)
2 4 0	2.542 (-9.68%)	5.3 (-9.67%)	4.448 (-9.68%)	14.98 (-26.29%)	3.455 (-16.15%)	20.62 (-41.03%)	127.921 (7086.57	-34.113 (12828.73%)
2 6 0	2.417 (-14.11%)	5.04 (-14.1%)	4.229 (-14.11%)	12.88 (-36.63%)	3.58 (-13.1%)	22.95 (-34.37%)	10.101 (467.47%	-31.461 (11839.18%)
2 8 0	2.388 (-15.15%)	4.979 (-15.14%)	4.178 (-15.15%)	12.42 (-38.89%)	3.575 (-13.24%)	22.84 (-34.68%)	-18.176 (1121.12	-18.679 (7069.78%)
2 10 0	2.475 (-12.04%)	5.161 (-12.03%)	4.331 (-12.04%)	13.83 (-31.95%)	3.658 (-11.21%)	24.48 (-29.99%)	5.612 (215.28%)	1.774 (561.94%)
2 12 0	2.463 (-12.47%)	5.136 (-12.46%)	4.31 (-12.47%)	13.63 (-32.93%)	3.611 (-12.36%)	23.53 (-32.71%)	3.435 (92.98%)	3.721 (1288.43%)
2 14 0	2.505 (-10.97%)	5.224 (-10.95%)	4.384 (-10.97%)	14.35 (-29.39%)	3.59 (-12.87%)	23.13 (-33.85%)	-17.21 (1066.85%	-20.405 (7713.81%)
4 2 0	2.307 (-18.01%)	4.811 (-18.0%)	4.037 (-18.01%)	11.2 (-44.89%)	3.442 (-16.45%)	20.39 (-41.69%)	60.935 (3323.31%	76.408 (28410.45%)
4 4 0	6.092 (116.5%)	12.704 (116.52%	10.66 (116.5%)	206.26 (914.88%)	6.435 (56.19%)	133.25 (281.07%)	-0.0 (100.0%)	-17.683 (6698.13%)
4 6 0	2.37 (-15.79%)	4.941 (-15.78%)	4.146 (-15.79%)	12.14 (-40.27%)	3.752 (-8.92%)	26.42 (-24.44%)	10.299 (478.6%)	-20.119 (7607.09%)
4 8 0	2.592 (-7.88%)	5.405 (-7.87%)	4.536 (-7.88%)	15.89 (-21.81%)	3.589 (-12.88%)	23.12 (-33.88%)	-80.362 (4614.72	-93.514 (34993.28%)
4 10 0	2.579 (-8.35%)	5.378 (-8.34%)	4.513 (-8.35%)	15.65 (-23.0%)	3.757 (-8.82%)	26.5 (-24.21%)	-22.233 (1349.04	-43.832 (16455.22%)
4 12 0	2.645 (-6.01%)	5.515 (-5.99%)	4.628 (-6.01%)	16.88 (-16.94%)	3.697 (-10.28%)	25.26 (-27.76%)	1.425 (19.94%)	-0.883 (429.48%)
4 14 0	2.657 (-5.57%)	5.541 (-5.55%)	4.65 (-5.57%)	17.12 (-15.76%)	3.825 (-7.15%)	27.99 (-19.95%)	0.714 (59.89%)	-0.433 (261.57%)
6 2 0	2.241 (-20.37%)	4.672 (-20.36%)	3.921 (-20.37%)	10.26 (-49.52%)	3.383 (-17.89%)	19.36 (-44.63%)	59.738 (3256.07%	-105.326 (39400.75%)
6 4 0	6.092 (116.5%)	12.704 (116.52%	10.66 (116.5%)	206.26 (914.88%)	6.423 (55.89%)	132.46 (278.81%)	-6.884 (486.74%	-14.201 (5398.88%)
6 6 0	2.673 (-5.0%)	5.575 (-4.98%)	4.678 (-5.0%)	17.43 (-14.24%)	3.99 (-3.17%)	31.75 (-9.2%)	1.304 (26.74%)	-1.353 (604.85%)
6 8 0	2.654 (-5.7%)	5.533 (-5.69%)	4.643 (-5.7%)	17.04 (-16.16%)	3.911 (-5.06%)	29.92 (-14.43%)	4.388 (146.52%)	1.479 (451.87%)
6 10 0	2.682 (-4.69%)	5.593 (-4.68%)	4.693 (-4.69%)	17.6 (-13.4%)	3.887 (-5.65%)	29.37 (-16.01%)	4.097 (130.17%)	0.087 (67.54%)
6 12 0	2.711 (-3.67%)	5.652 (-3.66%)	4.743 (-3.67%)	18.17 (-10.6%)	3.931 (-4.58%)	30.38 (-13.12%)	3.516 (97.53%)	0.571 (113.06%)
6 14 0	2.741 (-2.61%)	5.715 (-2.6%)	4.795 (-2.61%)	18.78 (-7.59%)	3.982 (-3.36%)	31.56 (-9.74%)	2.317 (30.17%)	0.175 (34.7%)
8 2 0	2.36 (-16.13%)	4.921 (-16.12%)	4.13 (-16.13%)	11.99 (-41.0%)	3.435 (-16.62%)	20.27 (-42.03%)	11.412 (541.12%)	-4.462 (1764.93%)
8 4 0	6.092 (116.5%)	12.704 (116.52%	10.66 (116.5%)	206.26 (914.88%)	6.38 (54.85%)	129.82 (271.26%)	-16.489 (1026.35	7.126 (2558.96%)
8 6 0	2.68 (-4.76%)	5.588 (-4.75%)	4.689 (-4.76%)	17.56 (-13.6%)	4.089 (-0.76%)	34.17 (-2.28%)	3.316 (86.29%)	0.515 (92.16%)
8 8 0	2.697 (-4.16%)	5.624 (-4.15%)	4.719 (-4.16%)	17.89 (-11.97%)	3.973 (-3.57%)	31.35 (-10.34%)	3.005 (68.82%)	-0.087 (132.46%)
8 10 0	2.745 (-2.44%)	5.725 (-2.43%)	4.804 (-2.44%)	18.87 (-7.15%)	3.983 (-3.31%)	31.61 (-9.6%)	1.986 (11.57%)	0.392 (46.27%)
8 12 0	2.76 (-1.9%)	5.756 (-1.89%)	4.83 (-1.9%)	19.19 (-5.58%)	3.997 (-2.98%)	31.93 (-8.69%)	1.72 (3.37%)	-0.071 (126.49%)
8 14 0	2.758 (-1.99%)	5.751 (-1.98%)	4.826 (-1.99%)	19.14 (-5.82%)	4.013 (-2.59%)	32.32 (-7.57%)	1.632 (8.31%)	-0.432 (261.19%)
10 2 0	2.931 (4.17%)	6.112 (4.18%)	5.129 (4.17%)	22.97 (13.02%)	3.551 (-13.81%)	22.39 (-35.97%)	5.988 (236.4%)	-4.497 (1777.99%)
10 4 0	3.551 (26.17%)	7.404 (26.19%)	6.213 (26.17%)	40.83 (100.9%)	6.317 (53.33%)	126.05 (260.48%)	-5.207 (392.53%	-1.808 (774.63%)
10 6 0	6.092 (116.5%)	12.704 (116.52%	10.66 (116.5%)	206.26 (914.88%)	4.134 (0.34%)	35.32 (1.01%)	-272.121 (15387.	-267.005 (99728.73%)
10 8 0	2.749 (-2.33%)	5.731 (-2.31%)	4.809 (-2.33%)	18.94 (-6.81%)	4.005 (-2.78%)	32.13 (-8.11%)	2.026 (13.82%)	-0.01 (103.73%)
10 10 0	2.774 (-1.41%)	5.785 (-1.4%)	4.854 (-1.41%)	19.48 (-4.15%)	4.032 (-2.14%)	32.77 (-6.28%)	1.496 (15.96%)	0.216 (19.4%)
10 12 0	2.752 (-2.21%)	5.738 (-2.19%)	4.815 (-2.21%)	19.01 (-6.46%)	3.982 (-3.34%)	31.58 (-9.69%)	1.694 (4.83%)	-0.358 (233.58%)
12 2 0	2.931 (4.17%)	6.112 (4.18%)	5.129 (4.17%)	22.97 (13.02%)	3.438 (-16.55%)	20.32 (-41.89%)	8.92 (401.12%)	-2.907 (1184.7%)
12 4 0	3.626 (28.86%)	7.561 (28.88%)	6.345 (28.86%)	43.49 (113.99%)	6.304 (53.01%)	125.27 (258.25%)	-3.087 (273.43%	-1.241 (563.06%)
12 6 0	6.092 (116.5%)	12.704 (116.52%	10.66 (116.5%)	206.26 (914.88%)	4.158 (0.92%)	35.94 (2.78%)	-296.043 (16731.	-277.507 (103647.39%)
12 8 0	2.749 (-2.32%)	5.732 (-2.31%)	4.81 (-2.32%)	18.94 (-6.81%)	4.032 (-2.13%)	32.78 (-6.26%)	1.796 (0.9%)	0.223 (16.79%)
12 10 0	2.767 (-1.67%)	5.77 (-1.66%)	4.842 (-1.67%)	19.33 (-4.89%)	4.039 (-1.98%)	32.93 (-5.83%)	1.401 (21.29%)	0.187 (30.22%)
12 12 0	2.779 (-1.23%)	5.796 (-1.21%)	4.864 (-1.23%)	19.59 (-3.61%)	4.037 (-2.01%)	32.9 (-5.91%)	1.303 (26.8%)	-0.07 (126.12%)
14 2 0	2.931 (4.17%)	6.112 (4.18%)	5.129 (4.17%)	22.97 (13.02%)	3.33 (-19.19%)	18.46 (-47.21%)	9.002 (405.73%)	-2.823 (1153.36%)
14 4 0	3.622 (28.72%)	7.553 (28.74%)	6.338 (28.72%)	43.35 (113.3%)	6.309 (53.13%)	125.57 (259.11%)	-3.142 (276.52%	-1.075 (501.12%)
14 6 0	6.092 (116.5%)	12.704 (116.52%	10.66 (116.5%)	206.26 (914.88%)	4.173 (1.28%)	36.33 (3.9%)	0.34 (80.9%)	0.11 (58.96%)
14 8 0	2.773 (-1.47%)	5.782 (-1.45%)	4.852 (-1.47%)	19.44 (-4.35%)	4.043 (-1.88%)	33.04 (-5.51%)	1.568 (11.91%)	0.245 (8.58%)
14 10 0	2.78 (-1.22%)	5.796 (-1.21%)	4.864 (-1.22%)	19.59 (-3.61%)	4.045 (-1.82%)	33.1 (-5.34%)	1.315 (26.12%)	0.173 (35.45%)
14 12 0	2.782 (-1.13%)	5.802 (-1.11%)	4.869 (-1.13%)	19.65 (-3.31%)	4.035 (-2.06%)	32.85 (-6.05%)	1.306 (26.63%)	-0.005 (101.87%)
16 2 0	2.931 (4.17%)	6.112 (4.18%)	5.129 (4.17%)	22.97 (13.02%)	3.544 (-13.98%)	22.26 (-36.34%)	9.072 (409.66%)	-2.488 (1028.36%)
16 4 0	3.548 (26.07%)	7.398 (26.09%)	6.208 (26.07%)	40.73 (100.41%)	6.311 (53.18%)	125.69 (259.45%)	-3.589 (301.63%	-1.324 (594.03%)
16 6 0	6.092 (116.5%)	12.704 (116.52%	10.66 (116.5%)	206.26 (914.88%)	4.184 (1.55%)	36.62 (4.73%)	-3.48 (295.51%)	0.927 (245.9%)
16 8 0	2.777 (-1.32%)	5.79 (-1.3%)	4.859 (-1.32%)	19.53 (-3.9%)	4.042 (-1.9%)	33.02 (-5.57%)	1.557 (12.53%)	0.275 (2.61%)
16 10 0	2.776 (-1.35%)	5.788 (-1.34%)	4.857 (-1.35%)	19.51 (-4.0%)	4.043 (-1.86%)	33.05 (-5.48%)	1.249 (29.83%)	0.082 (69.4%)
16 12 0	2.779 (-1.23%)	5.796 (-1.22%)	4.864 (-1.23%)	19.59 (-3.61%)	4.036 (-2.04%)	32.87 (-6.0%)	1.37 (23.03%)	-0.032 (111.94%)
18 2 0	2.931 (4.17%)	6.112 (4.18%)	5.129 (4.17%)	22.97 (13.02%)	3.59 (-12.86%)	23.14 (-33.82%)	8.96 (403.37%)	-2.276 (949.25%)
18 4 0	3.554 (26.3%)	7.411 (26.32%)	6.219 (26.3%)	40.95 (101.49%)	6.31 (53.17%)	125.64 (259.31%)	-3.259 (283.09%	-1.383 (616.04%)
18 6 0	6.092 (116.5%)	12.704 (116.52%	10.66 (116.5%)	206.26 (914.88%)	4.166 (1.12%)	36.15 (3.38%)	-3.746 (310.45%	0.903 (236.94%)
18 8 0	2.775 (-1.4%)	5.785 (-1.39%)	4.855 (-1.4%)	19.48 (-4.15%)	4.045 (-1.83%)	33.08 (-5.4%)	1.514 (14.94%)	0.264 (1.49%)
18 10 0	2.779 (-1.24%)	5.795 (-1.23%)	4.863 (-1.24%)	19.58 (-3.66%)	4.047 (-1.77%)	33.14 (-5.23%)	1.3 (26.97%)	0.15 (44.03%)
18 12 0	2.781 (-1.16%)	5.8 (-1.14%)	4.867 (-1.15%)	19.63 (-3.41%)	4.04 (-1.94%)	32.97 (-5.71%)	1.393 (21.74%)	0.041 (84.7%)

(c)

Poly Type	aU_lata	aU_latb	aU_latc	aU_V	aUH3_lata	aUH3_V	DEF Vac_U	DEF Int1H
16 8 0	2.777 (-1.32%)	5.79 (-1.3%)	4.859 (-1.32%)	19.53 (-3.9%)	4.042 (-1.9%)	33.02 (-5.57%)	1.557 (12.53%)	0.275 (2.61%)
16 8 1	2.777 (-1.32%)	5.79 (-1.3%)	4.859 (-1.32%)	19.53 (-3.9%)	4.042 (-1.9%)	33.02 (-5.57%)	1.557 (12.53%)	0.275 (2.61%)
16 8 2	2.776 (-1.34%)	5.789 (-1.32%)	4.858 (-1.34%)	19.52 (-3.95%)	4.074 (-1.12%)	33.8 (-3.34%)	1.599 (10.17%)	0.244 (8.96%)
16 8 3	2.765 (-1.75%)	5.765 (-1.74%)	4.838 (-1.75%)	19.28 (-5.13%)	4.079 (-1.01%)	33.92 (-2.99%)	1.528 (12.54%)	0.374 (39.55%)
16 8 4	2.77 (-1.56%)	5.776 (-1.55%)	4.847 (-1.56%)	19.39 (-4.59%)	4.082 (-0.92%)	34.01 (-2.74%)	1.514 (14.94%)	0.384 (43.28%)

Table S6: Summary of validation tests using different values of LASSO/LARS parameter α: a) RMS, b) Validation tests.

α value	rms H (eV/Å)	rms U (eV/Å)	rms Energy (eV)	rms P (GPa)
1.00E-05	0.238	0.518	0.249	0.674
1.00E-04	0.243	0.532	0.250	0.684
1.00E-03	0.266	0.58	0.243	0.771
1.00E-02	0.326	0.702	0.253	1.234

a)

α value	α-U						α-UH$_3$	
	lat_a (Å)	lat_b (Å)	lat_c (Å)	Vol. (Å^3)	Vac 1U (eV)	Int 1H (eV)	lat (Å)	Vol. (Å^3)
1.00E-05	2.78 (-1.19%)	5.798 (-1.18%)	4.865 (-1.19%)	19.61 (-3.51%)	1.421 (20.17%)	0.263 (1.87%)	4.053 (-1.63%)	33.28 (-4.83%)
1.00E-04	2.781 (-1.19%)	5.798 (-1.17%)	4.866 (-1.18%)	19.61 (-3.51%)	1.409 (20.84%)	0.223 (16.79%)	4.051 (-1.67%)	33.24 (-4.94%)
1.00E-03	2.777 (-1.32%)	5.79 (-1.3%)	4.859 (-1.32%)	19.53 (-3.9%)	1.557 (12.53%)	0.275 (2.61%)	4.042 (-1.9%)	33.02 (-5.57%)
1.00E-02	2.759 (-1.97%)	5.752 (-1.95%)	4.827 (-1.97%)	19.15 (-5.77%)	1.93 (8.43%)	-0.001 (100.37%)	4.011 (-2.65%)	32.26 (-7.74%)

b)